

國 立 成 功 大 學  
航 空 太 空 工 程 學 系  
碩 士 論 文

以多自由度仿生撲翼機構分析雀類腕關節  
折曲運動於懸停飛行之氣動力效應

Aerodynamic Effect of Wrist Folding on  
Passerines in Hovering Flight with a Multi-  
articulated Flapping-wing Robot

研 究 生：陳威瀚

指 導 教 授：葉思沂

中華民國 一百零九年二月

國立成功大學  
碩士論文

以多自由度仿生撲翼機構分析雀類腕關節折曲運動於  
懸停飛行之氣動力效應

Aerodynamic Effect of Wrist Folding on Passerines in  
Hovering Flight with a Multi-articulated  
Flapping-wing Robot

研究生：陳威瀚

本論文業經審查及口試合格特此證明

論文考試委員：

尤芳志，葉思沂  
龔光民  
高君易

指導教授：葉思沂

系(所)主管：呂章祥

中華民國 109 年 2 月 20 日

## 摘要

論文題目(中文)：以多自由度仿生撲翼機構分析雀類腕關節折曲運動於懸停飛行之氣動力效應

論文題目(英文)：Aerodynamic Effect of Wrist Folding on Passerines in Hovering Flight with a Multi-articulated Flapping-wing Robot

研究 生：陳威瀚

指 導 教 授：葉思沂

本研究根據小型雀類尺寸、外型及飛行模式設計並製作一拍撲實驗機構，其單翅擁有五個可控自由度並能仿照雀類之懸停飛行之運動以進行升力量測與流場可視化實驗。近年，開始有研究學者投入大量心力以昆蟲或簡化的鳥類模型分析探討拍撲飛行之空氣動力學機制及效應。然而，由於鳥類在飛行時的翅膀運動學較為複雜，因此這類多自由度之空氣動力學機制仍然有待深入研究。本研究根據雀類懸停飛行之運動學軌跡衍生出兩種運動模式進行觀察與實驗，其中一種之運動軌跡與真實雀類相似，另一種則將翅膀上拍時的折曲幅度縮小為二分之一，探討雀類腕關節折曲運動於懸停飛行之氣動力效應。實驗中首先利用直接線性轉換(DLT)進行運動學分析，驗證本研究之拍撲機構能確實重現此兩種運動模式後，接續進行升力量測及流場可視化實驗。本研究根據力平衡儀量測之結果，將一個拍撲週期分為四階段並可由運動學觀察以及流場可視化之結果詳加說明。實驗結果指出，折曲幅度較小之運動模式雖然會於上拍時產生極大之負升力，但同時也會誘發下拍初期的「尾流捕捉」效應，使其在下拍初期便產生極大升力。也因此，其整體升力反而較另一模式略大一些。然

而，單純擁有較大之升力並不代表該運動模式會是對飛行之表現及效率有益的。未來若能再針對像是水平力或者是功耗進行量測實驗，將有可能更利於深入了解這些運動模式在鳥類飛行上之效益。

**關鍵字：**拍撲翼、懸停飛行、翅膀折曲、力量測、粒子影像測速法、翼前緣渦流、尾流捕捉



# **Aerodynamic Effect of Wrist Folding on Passerines in Hovering Flight with a Multi-articulated Flapping-wing Robot**

Student: Wei-Han Chen

Advisor: Szu-I Yeh

## **ABSTRACT**

In this study, a novel multiarticulate flapping-wing robot with five degrees of freedom on each wing was designed and fabricated to replicate hovering motion of passerines for force measurement and PIV experiments. Recent years, several researchers have focused on exploring the aerodynamic characteristics of insects and also some simplified model of birds. However, birds, like passerines, perform much more complicated wing kinematics which are rarely tested. The detailed aerodynamic effect of wings with higher degrees of freedom still remains to be further investigated. Two modified wing trajectories from previous observed wing kinematics of passerines were experimented in this research to investigate the aerodynamic differences, one with a larger folding amplitude, similar to that of real passerines, and one with only half the amplitude. Kinematics of the robot was verified utilizing direct linear transformation (DLT) which confirmed that the wing trajectories had high correlation with the desired motion. According to the lift force measurements, 4 phases of the wingbeat cycle were characterized and elaborated through camera images and flow visualization results. We found that although less folding caused higher negative lift during upstrokes, it also induced greater lift at the initial downstroke through ‘wake capture’ which ended up producing higher cycle-averaged lift. However, this does not imply that less folding benefits flight performance. Further investigation such as the horizontal force or power

requirement could be a helping hand to more thoroughly understand the pros and cons of folding on passerines during hovering flight.

**KEYWORDS:** flapping wing, hovering flight, wing folding, force measurement, PIV, leading-edge vortex, wake capture



## 誌謝

在完成這篇論文的同時，我首先要感謝指導教授葉思沂老師在這段時間的指導與幫助，並提供了實驗室的資源與設備，使這篇論文研究得以順利完成。此外也要感謝口試委員尤芳恣老師、苗君易老師以及鍾光民主任對於相關實驗方法以及論文撰寫等方面之提醒與建議，使我獲益良多。我也要感謝實驗室的學弟夥伴們，包括威仲、登元、羿賢以及柏翔，在我進行實驗以及資料後處理的時候，不辭辛勞地給予必要的支援與幫助。最後我也要感謝一直以來陪伴、支持以及包容我的父母，沒有你們過去辛苦的栽培就沒有現在的我。

這篇論文謹獻給這一路上曾經支持、協助過我的每一個人。



## CONTENTS

<b>摘要 .....</b>	i
<b>ABSTRACT .....</b>	iii
<b>誌謝 .....</b>	v
<b>CONTENTS .....</b>	vi
<b>LIST OF TABLES.....</b>	ix
<b>LIST OF FIGURES.....</b>	x
<b>NOMENCLATURE .....</b>	xiv
<b>CHAPTER I INTRODUCTION.....</b>	1
1.1 Background and Motivation .....	1
1.2 Flapping Wing Micro Aerial Vehicles.....	3
1.2.1 MicroBat .....	3
1.2.2 Nano Hummingbird .....	4
1.2.3 DelFly .....	5
1.3 Flapping Wing Aerodynamics .....	6
1.3.1 Delayed Stall .....	6
1.3.2 Added Mass.....	7
1.3.3 Rotational Circulation .....	8
1.3.4 Clap and Fling .....	9
1.3.5 Wake Capture .....	10
1.4 Related Research on Wing Kinematics .....	11
1.5 Objective .....	13
<b>CHAPTER II Design of Flapping-wing Robot .....</b>	14
2.1 Flow Similarity and Dimensional Analysis .....	14
2.1.1 Flow Similarity.....	14
2.1.2 Buckingham Pi Theorem & Dimensionless Parameters .....	15
2.2 Mechanical Design of Robot .....	19
2.2.1 Initial Sizing .....	19

2.2.2 Mechanism Linkage .....	21
2.3 Electronic and Control System .....	25
2.3.1 Motor & Driver .....	25
2.3.2 Controller Board.....	27
2.4 Completed Flapping-wing Robot.....	29
2.4.1 Robot Assembly .....	29
2.4.2 Flapping Mechanism.....	30
2.4.3 Control Algorithm.....	31
2.5 Mathematical Representation of Kinematics .....	32
2.5.1 Denavit-Hartenberg Convention .....	32
2.5.2 Kinematics of the Bevel-gear Train .....	35
<b>CHAPTER III Wing Trajectory and Kinematic Analysis .....</b>	<b>37</b>
3.1 Reference Kinematics .....	37
3.1.1 Previously Observed Wing Kinematics .....	37
3.1.2 Solving for the Mechanical Kinematic Angles .....	40
3.2 Kinematic Analysis.....	47
3.2.1 Objective .....	47
3.2.2 Experimental Method.....	47
3.2.3 Camera Positioning .....	50
3.2.4 Feature Point Tracking .....	54
3.2.5 Kinematic Verification Results .....	56
<b>CHAPTER IV Force Measurement and Flow Visualization.....</b>	<b>67</b>
4.1 Force Measurement System.....	67
4.1.1 Construction of the Force Measurement System .....	67
4.1.2 Uncertainty and Calibration of the Force Measurement System .....	70
4.2 Flow Visualization System .....	73
4.2.1 High-speed Camera .....	73
4.2.2 Laser and Optics.....	73
4.2.3 Experimental Setup .....	74
4.2.4 Image Processing Tool.....	75
4.3 Results and Discussion .....	76
4.3.1 Force Measurement and Wingbeat Phase Characterization.....	76

4.3.2 Phase 1 – Pre-downstroke .....	79
4.3.3 Phase 2 – Downstroke.....	85
4.3.4 Phase 3 – Folding Upstroke .....	87
4.3.5 Phase 4 – None-lifting Upstroke .....	90
4.3.6 Comparisons.....	92
<b>CHAPTER V Conclusion.....</b>	<b>96</b>
5.1 Concluding Remarks.....	96
5.2 Perspectives .....	99
<b>REFERENCES .....</b>	<b>100</b>



## LIST OF TABLES

	<b>Page</b>
Table 2-1 Dimensional parameters involved in present research .....	16
Table 2-2 Characteristics of the NEMA17 stepper motor .....	26
Table 2-3 Characteristics of the DRV8825 stepper motor driver .....	27
Table 2-4 Specifications of the Raspberry Pi 3 model B microcontroller board.....	28
Table 2-5 DH parameters of the designed flapping mechanism.....	34
Table 3-1 Statistical comparison of experimental case 1 .....	60
Table 3-2 Statistical comparison of experimental case 2 .....	65
Table 4-1 Equivalent averaged lift of case 1 .....	94
Table 4-2 Equivalent averaged lift of case 2 .....	94



## LIST OF FIGURES

	<b>Page</b>
Figure 1-1 Design sketches of Leonardo da Vinci[1].....	1
Figure 1-2 Types of MAVs (a) Fixed-wing[3] (b) Rotary-wing[4] (c) Flapping-wing[5] ....	3
Figure 1-3 Photo of MicroBat[7].....	4
Figure 1-4 Nano Hummingbird[8] .....	4
Figure 1-5 (a) DelFly I (b) DelFly II (c) DelFly Micro (d) DelFly Explorer[10] .....	5
Figure 1-6 Comparison between the formation of LEV for non-rational and rotational flapping motion[14].....	7
Figure 1-7 Illustration of (a) advanced rotation (b) symmetric rotation (c) delayed rotation[19] .....	8
Figure 1-8 Illustration of wing sections during the process of clap and fling[14] .....	9
Figure 1-9 Clap and fling during transition from upstroke to downstroke of a turtledove .	10
Figure 2-1 Mass versus reduced frequency for birds and insects[28] .....	18
Figure 2-2 Experimental water tank and its dimensions .....	19
Figure 2-3 Structure of a general bird's wing [33].....	21
Figure 2-4 Conceptual sketch of the flapping mechanism .....	21
Figure 2-5 Illustration of the coaxial bevel-gear train for the shoulder joint .....	22
Figure 2-6 CAD design of the shoulder joint in CATIA (left) and the actual shoulder joint assembly (right) .....	22
Figure 2-7 Illustration of the wrist joint mechanism .....	23
Figure 2-8 CAD design of wrist joint (left) and the actual wrist assembly (right) .....	23
Figure 2-9 Illustration of the actuation mechanism for power transfer .....	24
Figure 2-10 NEMA17 bipolar stepper motor .....	25
Figure 2-11 DRV8825 stepper motor driver board.....	26
Figure 2-12 Raspberry Pi 3 model B microcontroller board.....	27
Figure 2-13 Robot Assembly .....	29

Figure 2-14 Joints and DOFs of the flapping mechanism.....	30
Figure 2-15 Sketch of attached frames according to the D-H convention .....	32
Figure 2-16 Sketch of attached frames of the designed flapping mechanism.....	34
Figure 2-17 Functional schematic of a bevel-gear train[37] (left) and the corresponding members labeled in the CAD design (right).....	35
Figure 3-1 Illustration of reference kinematic angles[20] .....	38
Figure 3-2 Observed reference kinematic angles within a wingbeat cycle (redrawn with datapoints adopted from [38]) .....	39
Figure 3-3 Eighth-order Fourier series regression curve of reference kinematic angles ....	39
Figure 3-4 Flow chart of the binary genetic algorithm optimization process .....	40
Figure 3-5 Results of mechanical kinematic angles ( $\Phi$ ) using GA optimization process... <td>43</td>	43
Figure 3-6 Results of reference kinematic angles ( $\Theta$ ) using GA optimization process compared with the original reference .....	44
Figure 3-7 Proposed folding motion and reference kinematics.....	46
Figure 3-8 Feature points marked for kinematic analysis .....	47
Figure 3-9 Experimental setup for kinematic analysis .....	48
Figure 3-10 Calibration Cube .....	48
Figure 3-11 Top view illustration of the refraction experiment .....	51
Figure 3-12 Image captured in the refraction experiment .....	51
Figure 3-13 (a) Mean error (b) Maximum error of DLT method in refraction experiment ( $n = 64$ with 4 samples).....	52
Figure 3-14 Top view illustration of the second refraction experiment .....	53
Figure 3-15 Image captured in second refraction experiment (a) camera 1 (b) camera 2... <td>53</td>	53
Figure 3-16 (a) Mean error (b) Maximum error of DLT method in second refraction experiment ( $n = 64$ with 4 samples).....	54
Figure 3-17 Flow chart of the feature point tracking algorithm.....	55
Figure 3-18 Camera images from flapping sequence of experimental case 1.....	57

Figure 3-19 Flapping angle of experimental case 1 .....	58
Figure 3-20 Arm-sweeping angle of experimental case 1 .....	58
Figure 3-21 Twisting angle of experimental case 1.....	59
Figure 3-22 Folding angle experimental case 1 .....	59
Figure 3-23 Hand-sweeping angle of experimental case 1 .....	60
Figure 3-24 Camera images from flapping sequence of experimental case 2.....	62
Figure 3-25 Flapping angle of experimental case 2 .....	63
Figure 3-26 Arm-sweeping angle of experimental case 2 .....	63
Figure 3-27 Twisting angle of experimental case 2.....	64
Figure 3-28 Folding angle of experimental case 2 .....	64
Figure 3-29 Hand-sweeping angle of experimental case 2 .....	65
Figure 4-1 Configurations of force balance.....	68
Figure 4-2 System layout of the force measurement system.....	69
Figure 4-3 Drift assessment of the force measurement system .....	70
Figure 4-4 Frequency spectrum of measured force data .....	71
Figure 4-5 Distribution of linearly compensated force data.....	72
Figure 4-6 Linearity calibration results of the force measurement system .....	72
Figure 4-7 Photron Fastcam SA-X highspeed camera .....	73
Figure 4-8 Elforlight HPG-5000 laser with power supply .....	74
Figure 4-9 Experimental setup for PIV flow visualization experiment.....	74
Figure 4-10 Graphical user interface of PIVlab .....	75
Figure 4-11 Experimental phases of force measurement .....	76
Figure 4-12 Comparison of unfiltered and filtered lift data .....	77
Figure 4-13 Lift production history of case 1.....	78
Figure 4-14 Lift production history of case 2.....	78

Figure 4-15 Lift production history comparison of both cases.....	79
Figure 4-16 Kinematic comparison of Phase 1 .....	80
Figure 4-17 Velocity field comparison of phase 1 at $y = 60$ mm .....	83
Figure 4-18 Velocity field comparison of phase 1 at $y = 150$ mm.....	84
Figure 4-19 Kinematic comparison of phase 2.....	85
Figure 4-20 Velocity field during and after maximum lift at $y = 150$ mm (case 2) .....	86
Figure 4-21 Velocity field of clap effect before stroke reversal ( $y = 0$ mm) .....	86
Figure 4-22 Kinematic comparison of phase 3.....	88
Figure 4-23 Velocity field comparison of phase 3 at $y = 0$ mm .....	89
Figure 4-24 Kinematic comparison of phase 4.....	91
Figure 4-25 Lift-to-weight ratio comparison of case 1 and real passerines (data source:[38]) .....	93
Figure 4-26 Lift-to-weight ratio comparison of both cases.....	93

# NOMENCLATURE

## Alphabetic Symbols

$AR$	Aspect ratio
$b$	Wingspan (mm)
$c$	Chord length (mm)
$C_L$	Lift coefficient
$C_D$	Drag coefficient
$f$	Frequency (Hz)
$f_w$	Wing flapping frequency (Hz)
$J$	Advance ratio
$k$	Reduced frequency
$P$	Power (W)
$q$	Dynamic pressure
$Re$	Reynolds number
$Ro$	Rossby number
$S$	Wing area ( $\text{m}^2$ )
$St$	Strouhal number
$T$	Normalized time
$V_w$	Average wing-tip velocity (m/s)

## Greek Symbols

$\alpha$	Angle of attack (deg)
$\rho$	Density ( $\text{kg}/\text{m}^3$ )
$\Theta$	Reference kinematic angles (deg)
$\Phi$	Mechanical kinematic angles (deg)
$\Psi$	Motor angles (deg)
$\mu$	Dynamic viscosity ( $\text{kg}/(\text{m} \cdot \text{s})$ )
$\nu$	Kinematic viscosity ( $\text{m}^2/\text{s}$ )

## Abbreviations

ADC	Analog to Digital Convertor
AOA	Angle of Attack
CAD	Computer Aided Design
CMOS	Complementary metal–oxide–semiconductor
DLT	Direct Linear Transformation
DOF	Degree of Freedom
DSLR	Digital Single-Lens Reflex Camera
FDM	Fused Deposition Modeling
GA	Genetic Algorithm
GPIO	General Purpose Input / Output
I/O	Input / Output
LEV	Leading-edge Vortex
MAV	Micro Aerial Vehicle
PIV	Particle Image Velocimetry
PLA	Polylactic Acid
TTL	Transistor-Transistor Logic
UAV	Unmanned Aerial Vehicle

# CHAPTER I

## INTRODUCTION

This chapter introduces the background of the present research and briefly covers the basic aerodynamic mechanisms of flapping-wing flight. Previous researches that drives the concept of this research are also mentioned along with the main objectives of this research.

### **1.1 Background and Motivation**

For more than several hundreds of years, humans have long wished to fly like birds in the sky. In order to realize the dream of flight, many efforts have been made trying to mimic the geometric shapes, internal structure of wings and even the flapping motion of flying vertebrates or insects. In the 15th century, Leonardo da Vinci designed and sketched the very first man-powered ornithopter (Figure 1-1). However, flapping flights are not only complicated in the field of mechanical engineering but also equally, if not more, complicated in aerodynamics and control. It was not until 1903, when the Wright brothers accomplished the first powered and controllable flight with human onboard, that the aviation industry settled down to the commonly seen fixed-wing designs and expanded rapidly.

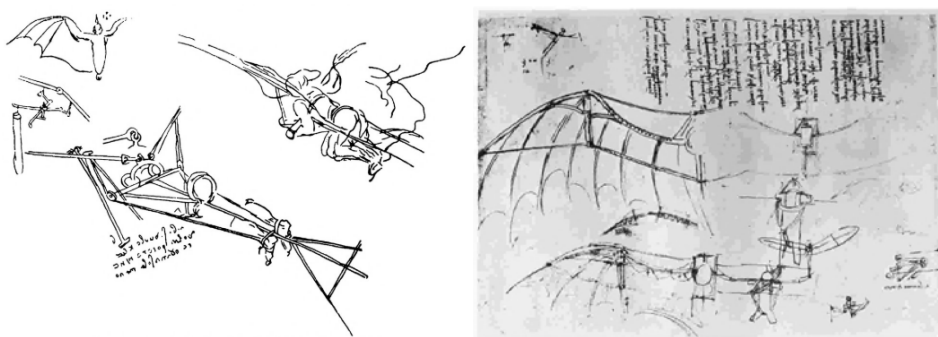


Figure 1-1 Design sketches of Leonardo da Vinci[1]

In modern days, the fixed-wing designs are capable of efficiently perform missions from scales as large as super jumbo passenger jets to small unmanned aerial vehicles (UAVs). However, the demand for research concerning even smaller micro scale vehicles for rescue or scouting purposes has risen recent years. Consequently, biomimetic flapping-wing designs have again raised great interests since natural flyers are well-known to be efficient and highly maneuverable in such small scale. In addition, the advancement in material science and electrical technology provide ultra-light weight but at the same time strong and powerful enough components which make the realization of small size flapping-wing micro aerial vehicles (MAVs) possible.

In the field of biomimetic flapping-wing flight, recent research mainly focuses on two major aspects. One is the design, fabrication and control of flapping-wing robots or MAVs and the other targets at the investigation into the underlying aerodynamic mechanisms that enables flapping-wing flight. Although many research and experiments have been done, the current understanding of flapping-wing aerodynamics still only provide limited knowledge or guidance when it comes to the design of flapping-wing MAVs. Thus, extended investigation is required to gain further insight to flapping-wings.

The following sections briefly introduces some of the present progress in the field of flapping-wing flights which includes the development of novel flapping-wing MAVs, basic aerodynamic mechanisms of flapping-wing force generation and investigations into the effect of wing kinematics on the aerodynamics of flapping-wings.

## 1.2 Flapping Wing Micro Aerial Vehicles

Micro aerial vehicles are commonly defined as small UAVs which are less than 15 centimeters in any dimension. There are three main categories of MAVs shown in Figure 1-2 which are fundamentally different in the methods of lift and thrust production. Flapping-wing MAVs usually generate greater force per unit wing area thus has the potential to be much smaller than the others[2]. Also, their flight agility allows them to be deployed in confined areas for missions such as military reconnaissance.

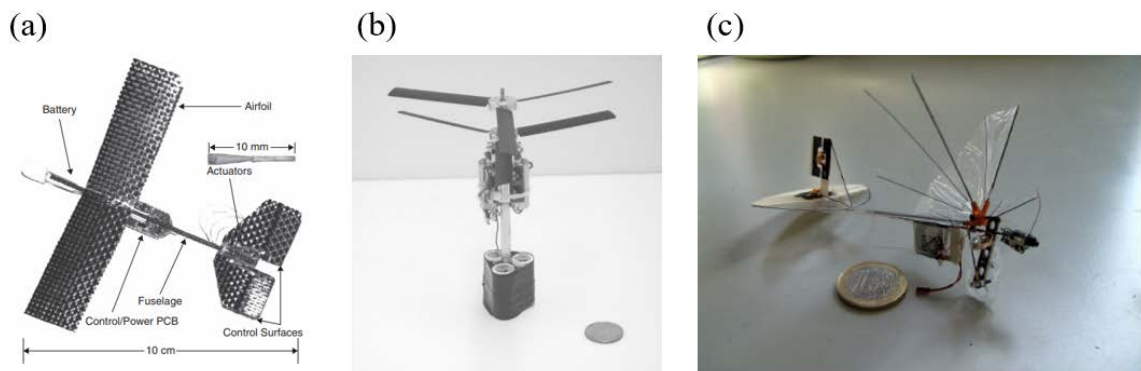


Figure 1-2 Types of MAVs (a) Fixed-wing[3] (b) Rotary-wing[4] (c) Flapping-wing[5]

Many research institutes, technological cooperation and defense agencies around the globe have invested in the development of flapping-wing MAVs with some iconic achievements showing the potential applications of the concept. Following are some brief introductions to some of the most well-known flapping-wing MAVs produced.

### 1.2.1 MicroBat

Since 1998, Caltech MEMS Lab have started the project of developing the world's first electric-powered flapping-wing MAV – MicroBat. The first prototype was powered by two super capacitors with a total weight of only 7.5 grams. Although the flight endurance was only 9 seconds, this still marks the very first milestone on electric-powered flapping-wing flight[6]. Further improvement in flight time was achieved by replacing the super capacitors

with nickel cadmium batteries and plastic lithium ion batteries. The latest prototype was built in 2001 which was radio-controlled and flew for 6 minutes and 17 seconds[7].

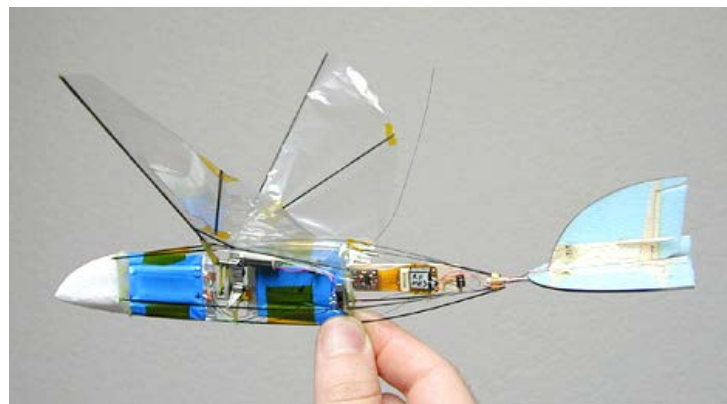


Figure 1-3 Photo of MicroBat[7]

### **1.2.2 Nano Hummingbird**

AeroVironment, an U.S. technology company, created a hummingbird-like flapping-wing MAV prototype – Nano Hummingbird (Figure 1-4), under the project funding of the Defense Advanced Research Projects Agency (DARPA) in 2011. The final prototype had a wingspan of 16.5 centimeters and weighed 19 grams with the appearance resembling a real hummingbird and having the capability to hover, maneuver in all directions and withstand mild wind gust while flying outdoors. Furthermore, live video was streamed to the operator wirelessly allowing heads-down operations[8]. According to DARPA, this concept has the potential of providing troops with enhanced situational awareness during urban operations.



Figure 1-4 Nano Hummingbird[8]

### **1.2.3 DelFly**

A group of students from Delft University of Technology (TUDelft) designed a flapping-wing MAV with a camera onboard – DelFly I (Figure 1-5a), which won the prize of the ‘most exotic MAV’ in the European Micro Air Vehicle conference and competitions in 2005. This led to the creation of the Micro Air Vehicle Laboratory (MAVLab) which focuses on the design and study of all types of autonomous MAVs.

Increased flight performance and smaller size was achieved as the team revealed the second generation – DelFly II (Figure 1-5b), which was capable of hovering, forward flight and even backward flight. Based on the experiences acquired, a miniaturized version – DelFly Micro (Figure 1-5c), which has a wingspan of only 10 centimeters and a total weight of only 3.07 grams was presented in 2008. This version of DelFly is currently the smallest and lightest flapping-wing MAV with an onboard camera and video transmitter which also holds the Guinness World Record as the ‘Smallest Camera Plane’.

The DelFly MAVs used the X-shaped wing configuration which is quite different from natural flyers. However, it enhances force production through the ‘clap and peel’ mechanism as the wings contact during each period. Furthermore, investigation on the aerodynamic effects of factors such as wing flexibility were also conducted through PIV[9].

The latest version of DelFly – DelFly Explorer, is a fully autonomous MAV equipped with an inertial measurement unit (IMU) and stereo-vision camera capable of taking-off, maintaining altitude and avoiding obstacles with all processing performed onboard[10].

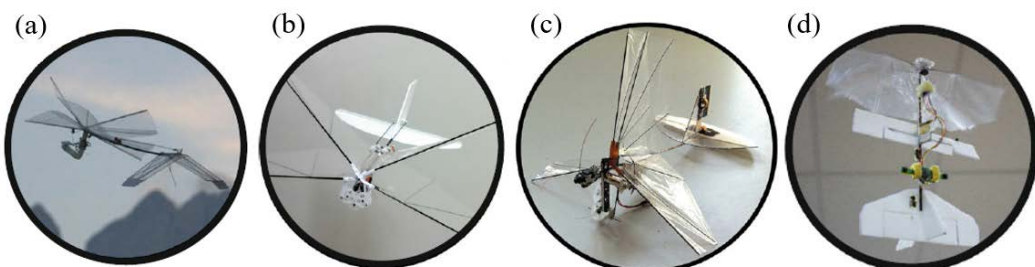


Figure 1-5 (a) DelFly I (b) DelFly II (c) DelFly Micro (d) DelFly Explorer[10]

## **1.3 Flapping Wing Aerodynamics**

According to classical physics theories of steady-state aerodynamics, animals such as birds, bats, and insects shouldn't be able to perform sustained flight due to their aerodynamic efficiency being greatly reduced with such a small scale or, in other words, under low Reynolds number ( $Re$ ) conditions. However, the key to allowing these species of animal to be able to produce sufficient lift to stay airborne lies under several unsteady aerodynamic mechanisms which enhances lift production.

For a simplified insect model of flapping motion, it is usually composed of two translational phases, the downstroke and upstroke, which are separated by two rotational phases, pronation and supination[11]. Within these phases, five key aerodynamic mechanisms, delayed stall, added mass, clap and fling, rotational circulation, and wake capture, which are unique to flapping-wings play an important role in the force production.

### **1.3.1 Delayed Stall**

Delayed stall, also often referred to as ‘absence of stall’, is the phenomenon of flapping-wings being able to still generate lift during the translational phases even the local angle of attack (AOA) of its wings had exceeded the critical angle of attack where stall happens for traditional fixed-wings. As the wing flaps at a high AOA during downstroke and upstroke, airflow over the lee-side of the wing separates around the leading edge and rolls into a strong vortex, as known as the leading-edge vortex (LEV), which remains stably attached to the wing surface[12]. Due to the strong LEV, airflow then reattaches to the wing surface behind the LEV which transfers additional downward momentum to the fluid and prevents the wing from stalling. Researchers have found that the key to allowing a stable LEV to form on the wing are the centripetal and Coriolis accelerations which are induced by the flapping motion

about the wing-base[13]. A comparison of a non-flapping motion and flapping motion where LEV stably attaches are shown in Figure 1-6.

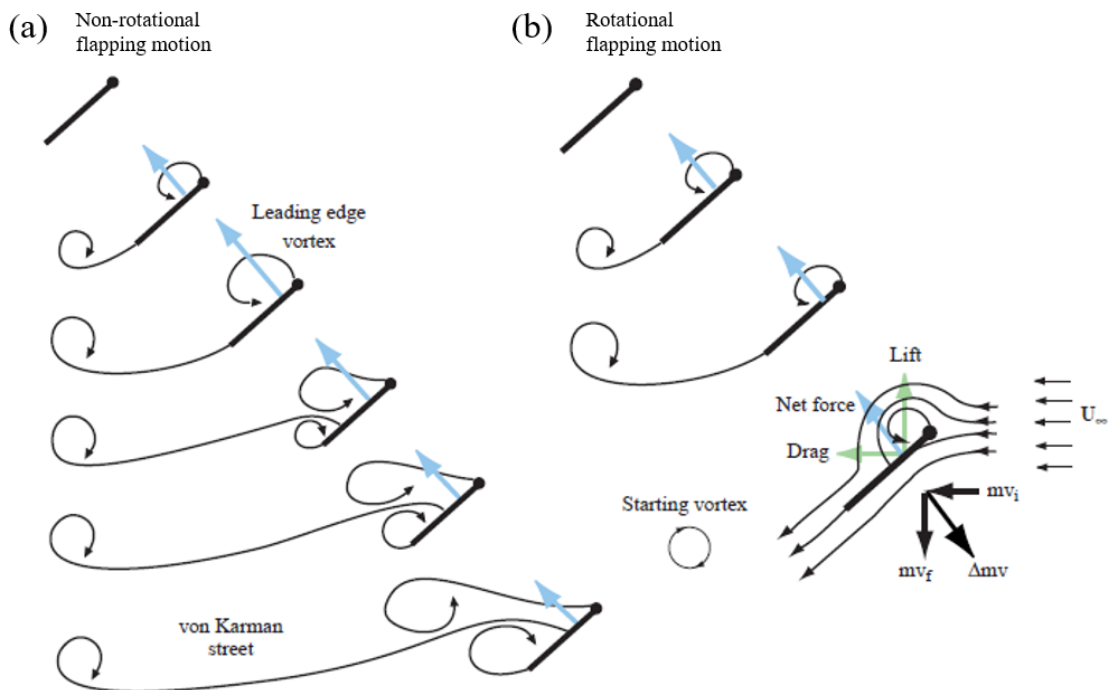


Figure 1-6 Comparison between the formation of LEV for non-rotational and rotational flapping motion[14]

### 1.3.2 Added Mass

During the acceleration phase of wings at startup or stroke reversal, fluid surrounding the wing also has to be accelerated or decelerated. The reaction force due to the accelerated fluid, which is different from the common circulation-base forces, acts on the wing surfaces as if there are additional mass on the wing, hence often called ‘added mass’, ‘added mass inertia’, ‘acceleration reaction’ or ‘virtual mass’ effect[14]. However, this effect is often difficult to be identified through experiments since it usually occurs along with other circulatory effects. Mathematically, researchers often model the added mass effect as a time-variant increase in the inertia of the wing[15].

### **1.3.3 Rotational Circulation**

When stroke reversal happens, the wings of flapping-wing animals often undergoes supination and pronation where the wings rotate along a spanwise axis. This allows the wings to maintain at a suitable AOA that produce sufficient forces during both downstrokes and upstrokes. As long as the rotational axis is not at the trailing edge, which is usually the case, the airflow around the wing deviates from the established Kutta condition and leads to sharp velocity gradients at the trailing edge which causes increased local shear. As a result, this forces the wing to generate additional circulation trying to re-establish the Kutta condition. This phenomenon is often known as the ‘Kramer effect’ under the context of aircraft wing fluttering analysis where extensive theoretical and experimental investigations were done by several researchers[16-18]. Based on the duration and timing where wing rotation happens, the rotational motion can either enhance or suppress the force generation. Figure 1-7 shows the three typical rotational modes where the wing chord is drawn in blue and the force vector shown in red. Generally, advanced rotation increases force production, delayed rotation decreases force production and symmetrical rotation lies somewhere in between. However, change in the force produced also leads to the change in power requirement, thus different modes could be used during various flight maneuvers.

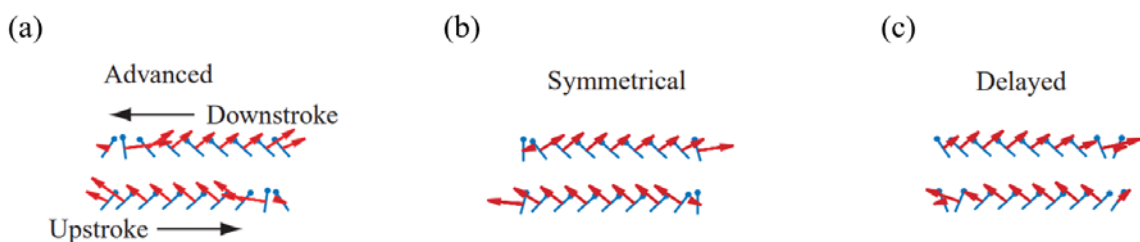


Figure 1-7 Illustration of (a) advanced rotation (b) symmetric rotation (c) delayed rotation[19]

### 1.3.4 Clap and Fling

Further force production enhancement can be achieved by interactions between the two wings during stroke reversal. The process of clap and fling, or in some cases called clap and peel, usually starts with the leading edge of both wings approaching first as shown in Figure 1-8a. After contact of the leading edge, the wing ‘claps’ and the air between two wings is pushed outwards as a jet flow (Figure 1-8c) providing extra force. The ‘fling’ motion then begins with the leading edge separating first creating a low-pressure region between the two wings which sucks surrounding air inwards (Figure 1-8d). This also assists the formation of leading-edge vortices which helps the wings to generate lift more rapidly in the following stroke.

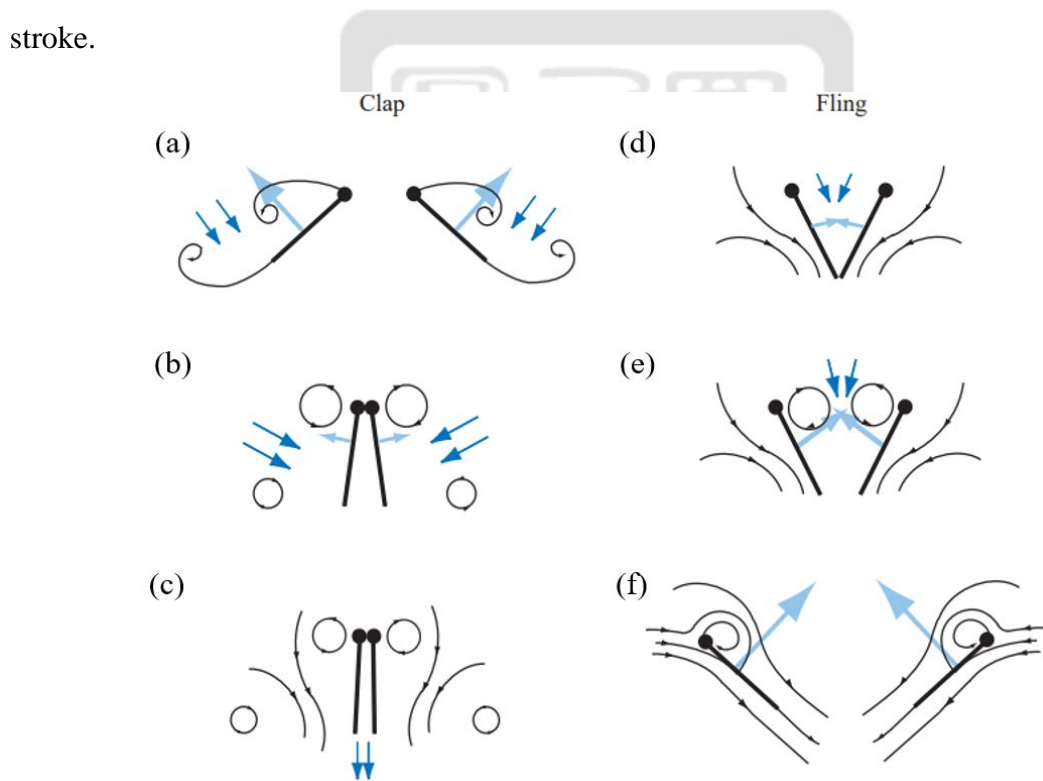


Figure 1-8 Illustration of wing sections during the process of clap and fling[14]

The clap and fling motions are not restricted to happen only from downstroke to upstroke or the opposite. As shown in Figure 1-9, turtledove exhibits clap and fling motion dorsally during transition from upstroke to downstroke at takeoff, where there is high

demand of lift and thrust. On the other hand, researchers have found that some species of passerines perform ‘ventral clap’ while hovering[20].

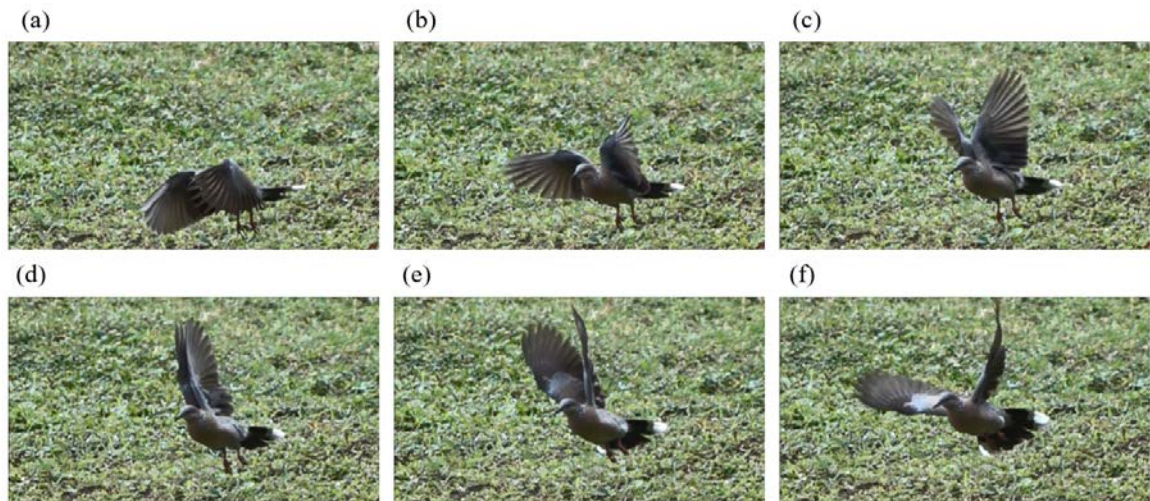


Figure 1-9 Clap and fling during transition from upstroke to downstroke of a turtledove

### 1.3.5 Wake Capture

The reciprocating property of flapping allows the wing to flap through vortices shed in the wake during the previous stroke, known as the ‘wake capture’ or ‘wing-wake interaction’. Through wake capture, some of the lost energy in the previous stroke should be recovered and supposedly increase the overall efficiency of flight. Although this effect has been qualitatively observed for butterflies[21], it is still difficult to quantify the effect since it usually requires methods of flow visualization and thus are unable to isolate from other aerodynamic effects.

## **1.4 Related Research on Wing Kinematics**

As described in the previous section, differences in flapping kinematics can substantially alter the surrounding flow field and consequently affect force production. Some researchers have put great effort into the investigation of wing kinematics not only *in vivo* and also with simplified flapping mechanisms. The following sections will briefly introduce some previous works on the topic of wing kinematics which are also the inspiration of this present research.

In natural flight, animals perform significantly different wing kinematics at different flight stages such as taking-off, cruising, hovering, turning and etc. Oorschot et al.[22] observed that birds extend and retract their wings within a single wingbeat and experimented the differences in aerodynamic performance between an extended wing and a retracted wing during take-off and gliding conditions with multiple wing samples of raptor species. They concluded that, contradictory to what hypothesized, extended wings had higher ratios between vertical and horizontal force coefficients during flapping flight compared with retracted wings but did not see much difference during gliding conditions. However, results of flapping flight were obtained with simplified propeller model to emulate quasi-steady flapping flight at low speeds which ignores the effect of other unsteady aerodynamic mechanisms, possibly resulting in misleading conclusions.

Ros et al.[23] statistically concluded that during 90-degree turning flights, pigeons create aerodynamic torques instead of relying on inertial angular momentum transfer between the wings and the torso. Furthermore, the study pointed out that the aerodynamic torques were generated with asymmetric wing trajectories instead of altering the wing speed, wing area or wingbeat amplitude. In order to make the turn, the outer wing swept further forward into the turn compared with the relatively straight inner wing. This research was

done purely with kinematic observations and the implementation of the angular momentum principle, thus further aerodynamic experiments could be done to verify the results.

Feshalami et al.[24] experimented with the aerodynamic effect of different wrist bending angles of a gull-sized flapping robot during forward flight in a wind tunnel with a two-component force balance. They concluded that the larger the bending deflection angle during upstrokes, the greater the lift and thrust forces were produced. Furthermore, the power consumption was also less with larger bending deflection angles meaning that the bending motion contributes to higher power loadings and more efficient flight.

Chang et al.[25] observed an unique ‘ventral-clap’ wing motion on hovering passerines (*Zosterops japonicus*) and conducted quantitative aerodynamic investigation on its effect. PIV was used to capture the flow structure around the bird during hovering in an experimental chamber and lift was calculated based on the transient vortex ring model. According to their observation, jet flows due to the ventral-clap was seen not only convecting downwards creating lift, but also temporarily moving upwards attenuating lift. However, the net contribution of the ventral-clap was positive and the calculated cycle-averaged lift was close to the weight of the bird. The purpose of the ventral-clap was thought to be the compensation of the non-lifting upstroke of an asymmetric hovering motion.

## **1.5 Objective**

The most significant differences in the flapping characteristics between insects and flying vertebrates are the muscle and bone structure which allow high-complexity flapping motion. Although researchers have done extensive investigation on simple flapping insects, aerodynamic mechanisms of flapping vertebrates are still not thoroughly understood.

Since passerines present unique types of flapping motion during hovering flight, this research aims to dig deeper into the underlying aerodynamic effects of the increased degree of freedom in flapping-wing kinematics.

In order to provide a controlled environment for experiments, a high DOF multiarticulate flapping-wing robot which mimics the hovering motion of passerines will be designed and constructed. The robot will be capable of executing custom kinematic trajectories and being submerged in a water tank for further aerodynamic analysis using PIV system.

The present research is expected to explore the aerodynamic benefits of a two-segmented wing and the aerodynamic effect of different wing folding angles during hovering flight in order to gain further insight into the design and development of flapping wing micro aerial vehicles.

## **CHAPTER II**

### **Design of Flapping-wing Robot**

This chapter describes the detail process of designing the flapping-wing robot used in this research, including the dimensional analysis to ensure proper scaling, design of each mechanical joints, selection of electronic components and the complete assembly of the robot.

#### **2.1 Flow Similarity and Dimensional Analysis**

##### **2.1.1 Flow Similarity**

To ensure that the characteristics of aerodynamic forces measured with the flapping-wing robot are scaled properly and can be comparable with the actual flying animal, the study of flow similarities should be conducted before proceeding into the designing process of the mechanism. Three major aspects of flow similarity which are geometric similarity, kinematic similarity, and dynamic similarity are considered.

First of all, geometric similarity is achieved by making the wing of the proposed flapping-wing robot geometrically similar to that of a passerine. In other words, the linear dimensions, such as the wingspan ( $b$ ), chord length ( $c$ ), etc. of the robot should be related to those of passerines by a constant scaling factor.

Secondly, the aspect of kinematic similarity requires that the flow fields around the robot and real passerines should be in the same direction with a constant scaling factor, i.e. the experimental robot should perform similar kinematic trajectories with that of an actual passerine in flight, which is the main purpose of designing a passerine-mimicking flapping wing robot in this chapter.

Finally, the most important aspect is to establish dynamic similarity, which allows all forces measured from the experimental model to be related quantitatively to the real-world scenario of passersines. Dynamic similarity is ensured by making all dimensionless groups, which are derived using the well-known Buckingham Pi theorem, identical between the experimental environment and the actual flight condition.

### **2.1.2 Buckingham Pi Theorem & Dimensionless Parameters**

According to the problem statement of the present research, the dimensional parameters involved are listed along with dimensions according to three selected primary dimensions, which are mass ( $M$ ), length ( $L$ ) and time ( $t$ ), as shown in Table 2-1. Since the force ( $F$ ) generated is the main interest, one can formulate the relation between  $F$  and other parameters as a function  $f$ .

$$F = f(\rho, V_w, b, c, \mu, f_w) \quad (2-1)$$

Or one can more formally write as

$$g(F, \rho, V_w, b, c, \mu, f_w) = 0 \quad (2-2)$$

where  $g$  is a function different from  $f$ .

Table 2-1 Dimensional parameters involved in present research

Parameter	Symbol	Unit	Dimension
Density	$\rho$	kg/m <sup>3</sup>	ML <sup>-3</sup>
Average Wing-tip Velocity	$V_w$	m/s	LT <sup>-1</sup>
Wingspan	$b$	m	L
Mean Chord Length	$\bar{c}$	m	L
Dynamic Viscosity	$\mu$	Pa · s	ML <sup>-1</sup> T <sup>-1</sup>
Flapping Frequency	$f_w$	Hz	T <sup>-1</sup>
Force	$F$	N	MLT <sup>-2</sup>

Since there are three primary dimensions, a set of 3 dimensional parameters that includes all primary dimensions should be selected as the repeating parameters. Along with the 7 dimensional parameters, a total of four dimensionless  $\Pi$  groups should be obtained according to the following equation

$$K = n - m = 7 - 3 = 4 \quad (2-3)$$

where  $K$ ,  $n$  and  $m$  represent respectively the total number of dimensionless  $\Pi$  groups, dimensional parameters and primary dimensions. The derived dimensionless  $\Pi$  groups are listed below.

$$\Pi_1 = \frac{b}{\bar{c}} \quad (2-4)$$

$$\Pi_2 = \frac{\mu}{\rho V_w \bar{c}} \quad (2-5)$$

$$\Pi_3 = \frac{f_w \bar{c}}{V_w} \quad (2-6)$$

$$\Pi_4 = \frac{F}{\rho V_w^2 \bar{c}^2} \quad (2-7)$$

$\Pi_1$  represents the aspect ratio ( $AR$ ) of the wing, which is related to its slenderness along the spanwise direction and is defined as

$$AR = \frac{b^2}{S} = \frac{b}{\bar{c}} \quad (2-8)$$

where  $S$  is the wing area. High  $AR$  wings usually tend to have greater aerodynamic performance, i.e. higher lift and lower induced drag, which is suitable for gliding. Fortunately, the identity of aspect ratio is automatically satisfied if the model is geometrically similar in the first place.

$\Pi_2$  is the inverse form of Reynolds number ( $Re$ ). Reynolds number represents the relation between the inertial force and the viscous force in the flow field, which is defined as

$$Re = \frac{\text{Inertial Force}}{\text{Viscous Force}} = \frac{VL}{\nu} = \frac{\rho VL}{\mu} \quad (2-9)$$

where  $V$ ,  $L$  and  $\nu$  represent the flow velocity, characteristic length and the kinematic viscosity. In contrast to large civilian or military aircrafts, natural flyers such as birds and insects usually fly in the low Reynolds number regime of  $10^5$  or lower[26].

When it comes to oscillating flow conditions with unsteady aerodynamic effects such as flapping-wings,  $\Pi_3$  resembles a critical dimensionless parameter which is the reduced frequency ( $k$ ). Reduced frequency describes the unsteadiness of the flow field which is defined as follows.

$$k = \frac{f\bar{c}}{2V} \quad (2-10)$$

For  $k = 0$ , the flow is steady. For  $0 \leq k \leq 0.05$ , the flow can be considered as quasi-steady, where unsteady effects are generally small and can sometimes be neglected. When it comes to  $k \geq 0.05$ , the flow is considered unsteady. Furthermore, flow fields with  $k$  greater than 0.2 are considered highly unsteady[27]. For flying birds and insects, the reduced frequency ranges roughly from 0.1 to 0.5 as shown in Figure 2-1, which, according to the above definitions, is obviously a highly unsteady phenomenon[28].

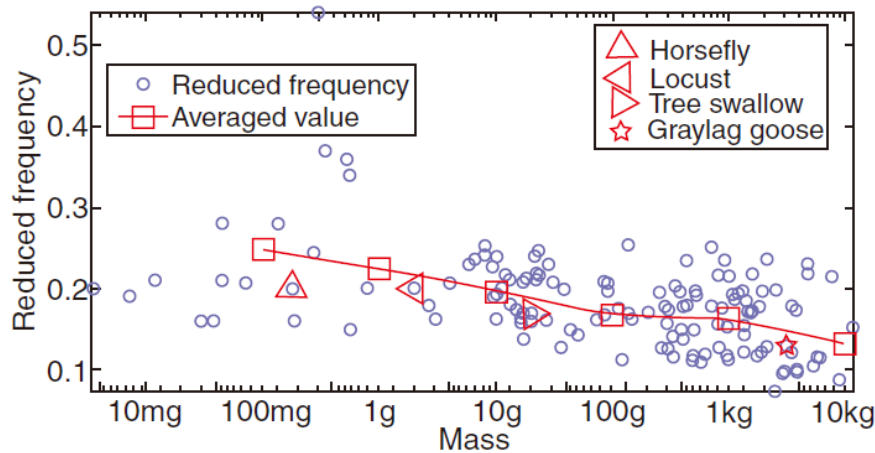


Figure 2-1 Mass versus reduced frequency for birds and insects[28]

Last but not least,  $\Pi_4$  resembles the force coefficients which are usually defined as

$$C_F = \frac{F}{qS} = \frac{F}{\frac{1}{2}\rho V^2 S} \quad (2-11)$$

where  $q$  represents the dynamic pressure and  $S$  is the reference wing area. Force coefficients that are usually discussed in the field of flapping-wing aerodynamics are the time-averaged coefficients and the transient coefficients, where the former describes the long-term performance and the latter provides the time history of force production.

## **2.2 Mechanical Design of Robot**

### **2.2.1 Initial Sizing**

The size of the robot mechanism could be determined and sometimes also limited by several factors such as the physical dimension of the water tank, structural limitation of the constructing materials that compose the mechanism, size of internal mechanical components, etc. According to previous researches, the size of robots used for aerodynamic experiments usually ranges between 15% to 30% of the chamber width in order to prevent interaction between the flow structure and the wall surface[29-32]. Since the water tank that is going to be used in this research has dimensions of 1800 mm × 800 mm × 900 mm (Figure 2-2) and also considering the orientation of the robot in the tank, the half span is conservatively set to be 150 mm which is around 18% of the tank width (800 mm).

The average half span of Japanese White-eye is about 66 mm[20], thus the scaling factor of the mechanism is

$$\text{Scaling Factor} = \frac{150 \text{ mm}}{66 \text{ mm}} = 2.27 \quad (2-12)$$

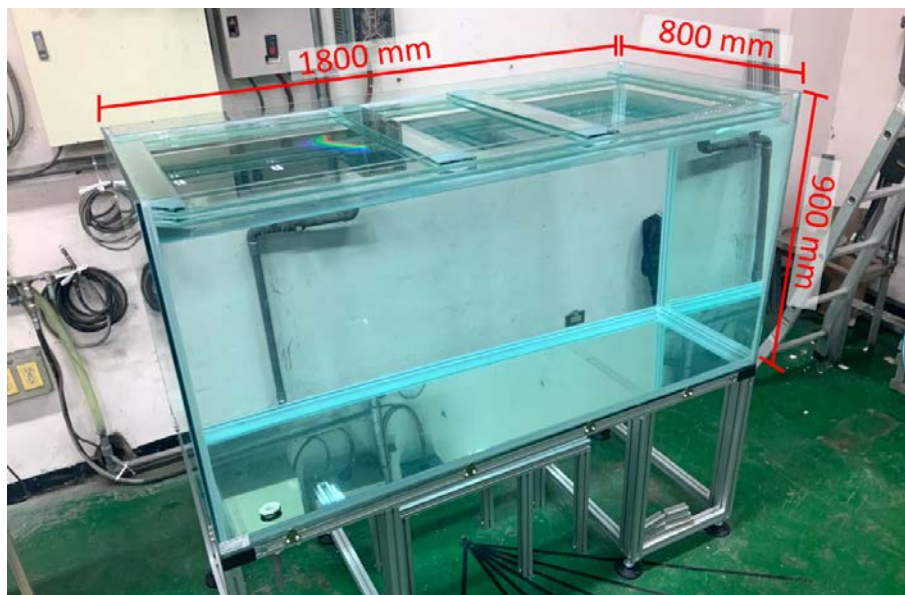


Figure 2-2 Experimental water tank and its dimensions

Furthermore, in order to maintain identical  $Re$  and  $k$  between real passerines and the robot, the average wing velocity of the flapping frequency should be changed accordingly. The average wing-tip velocity and flapping frequency of passerines are 9.4 m/s and 24.4 Hz[20], and the kinematic viscosity of air and water at room temperature (25°C) are  $1.552 \times 10^{-5}$  m<sup>2</sup>/s and  $8.917 \times 10^{-7}$  m<sup>2</sup>/s. Thus, we can derive the required wing velocity with  $Re$  as follows

$$\frac{V_{w_{robot}} \bar{c}_{robot}}{\nu_{water}} = \frac{V_{w_{bird}} \bar{c}_{bird}}{\nu_{air}} \quad (2-13)$$

By rearranging, one can get

$$\begin{aligned} V_{w_{robot}} &= V_{w_{bird}} \frac{\nu_{water}}{\nu_{air}} \frac{\bar{c}_{bird}}{\bar{c}_{robot}} \\ &= 9.4 \times \frac{8.917 \times 10^{-7}}{1.552 \times 10^{-5}} \times \frac{1}{2.27} \\ &= 0.2379 \text{ m/s} \end{aligned} \quad (2-14)$$

With a similar manner, the flapping frequency can also be obtained by

$$\frac{f_{w_{robot}} \bar{c}_{robot}}{V_{w_{robot}}} = \frac{f_{w_{bird}} \bar{c}_{bird}}{V_{w_{bird}}} \quad (2-15)$$

$$\begin{aligned} f_{w_{robot}} &= f_{w_{bird}} \frac{V_{w_{robot}}}{V_{w_{bird}}} \frac{\bar{c}_{bird}}{\bar{c}_{robot}} \\ &= 24.4 \times \frac{0.2379}{9.4} \times \frac{1}{2.27} \\ &= 0.2720 \text{ Hz} \end{aligned} \quad (2-16)$$

## 2.2.2 Mechanism Linkage

To design the mechanism, we have to first understand the general structure of a bird's wing. As shown in Figure 2-3, the wing of a bird can be generally divided into an arm section and a hand section. The arm section is connected to the body with a shoulder joint and the hand section is then connected to the arm section through a wrist joint.

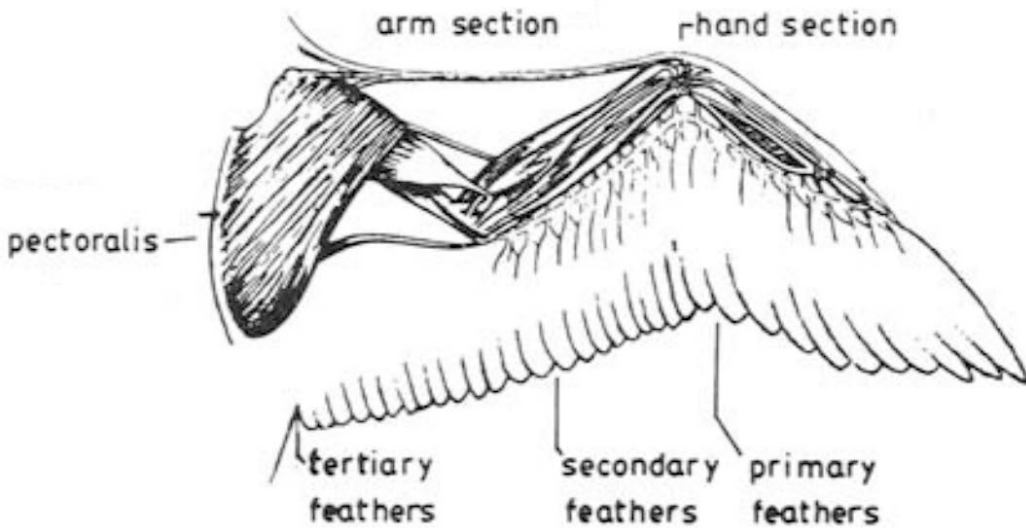


Figure 2-3 Structure of a general bird's wing [33]

The flapping mechanism of this research follows the structure described above with a 3-DOF shoulder joint connecting the fixed body and arm section and a 2-DOF wrist joint connecting the arm section with the hand section as shown in Figure 2-4.

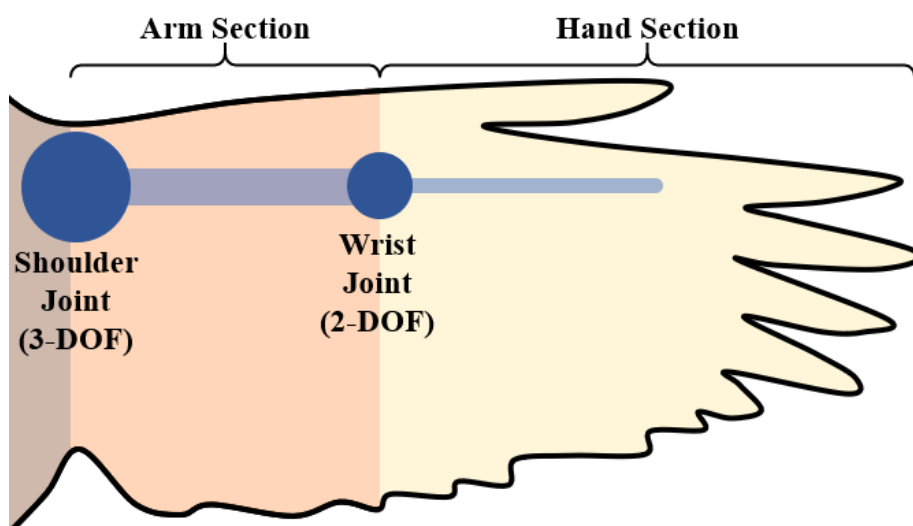


Figure 2-4 Conceptual sketch of the flapping mechanism

A compact 3-DOF coaxial bevel-gear train is used in the shoulder joint[34]. As shown in Figure 2-5, it comprises a C-shaped bracket (green), a set of two bevel gears with one attached to another C-shaped bracket (blue) and a set of three bevel gears (orange). In combination, it provides 3 axes of rotational motion, which are flapping, arm-sweeping, and twisting. Bearings were inserted and lubricated to ensure smooth rotation of the gears and shafts. The mechanical design and finished assembly are shown in Figure 2-6.

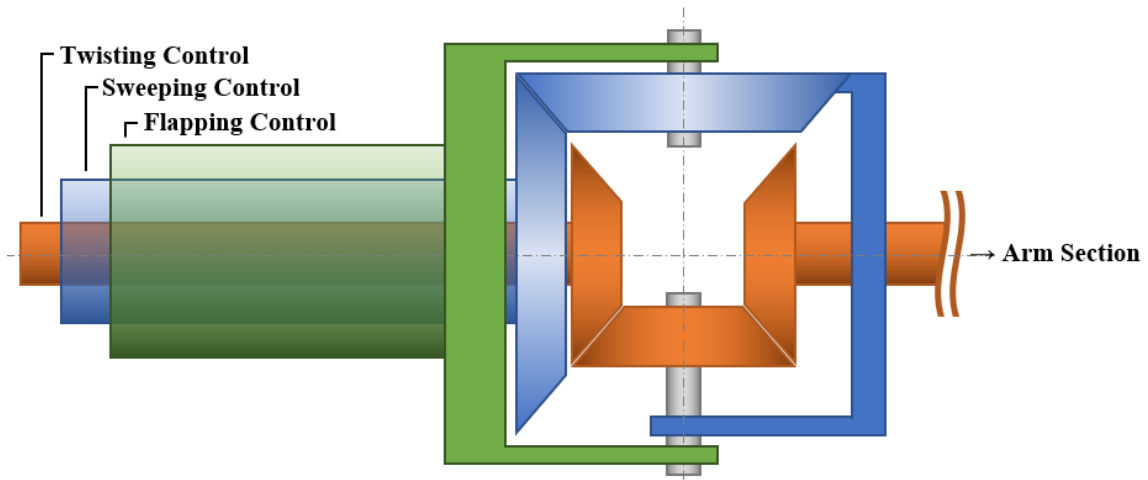


Figure 2-5 Illustration of the coaxial bevel-gear train for the shoulder joint

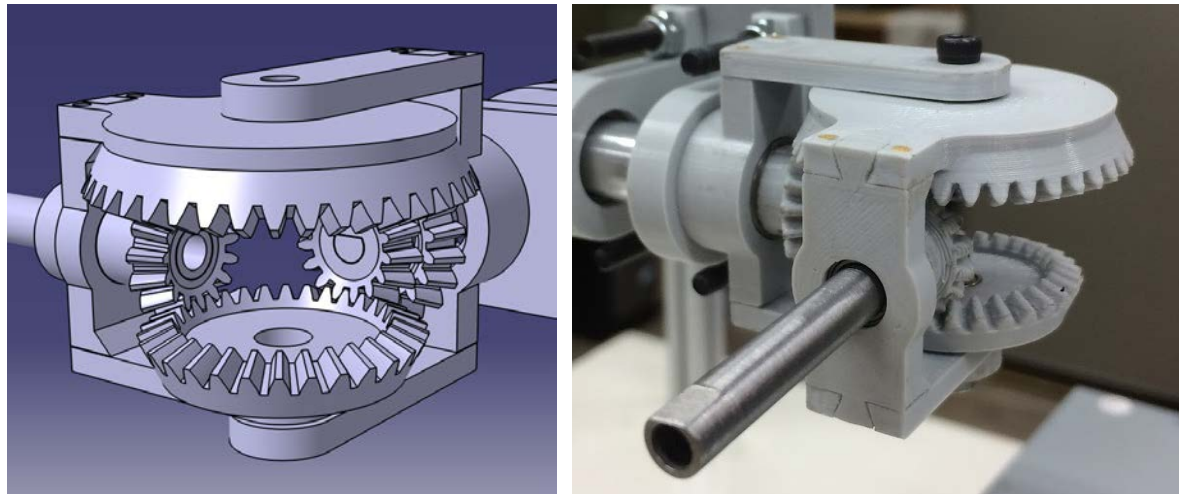


Figure 2-6 CAD design of the shoulder joint in CATIA (left) and the actual shoulder joint assembly (right)

To construct the 2-DOF wrist joint, which controls the folding and hand sweeping motion, simple pulleys with two actuating axes are used due to the restricted available space further out from the root of the wing as illustrated in Figure 2-7. Furthermore, in order to provide a more precise motion control, the reduction ratio from the motor to the actuating joint of the folding control and hand sweeping control are  $\frac{3}{2}:1$  and 3:1. The CAD design and actual wrist joint assembly are shown in Figure 2-8.

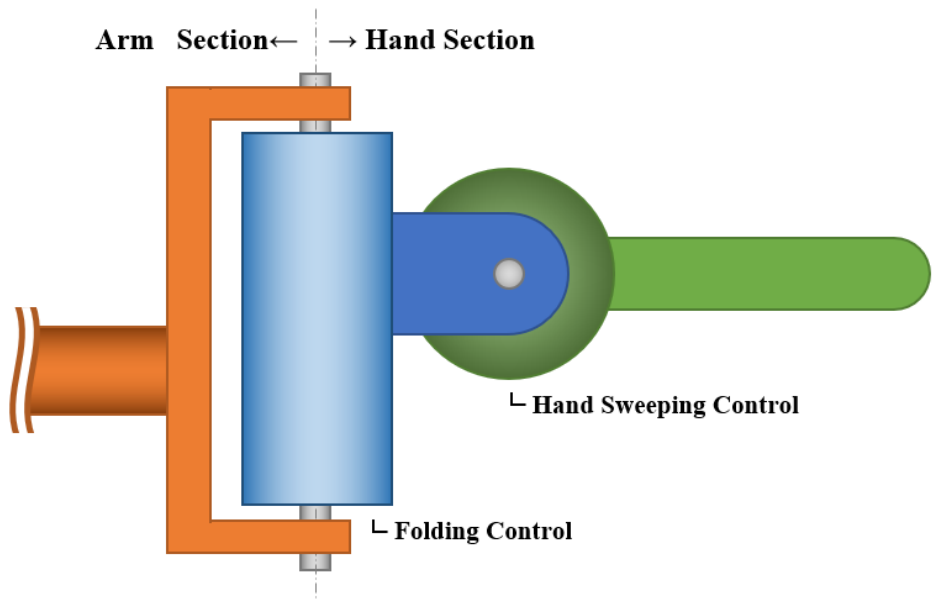


Figure 2-7 Illustration of the wrist joint mechanism

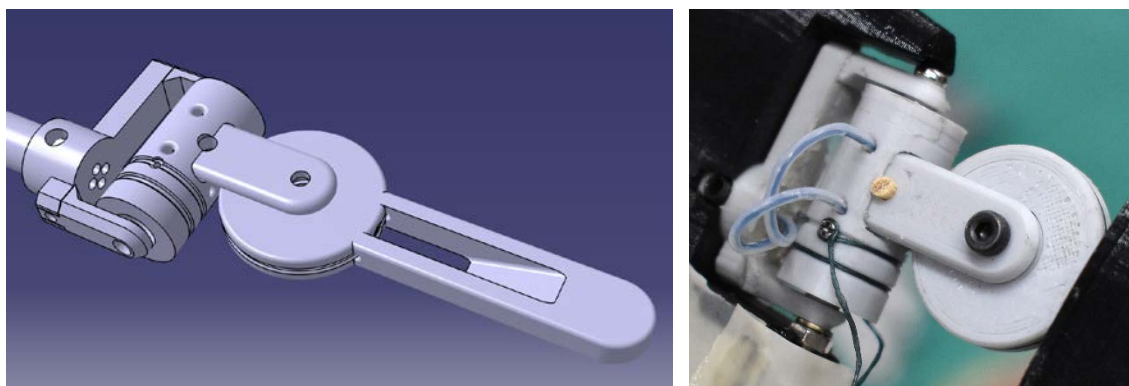


Figure 2-8 CAD design of wrist joint (left) and the actual wrist assembly (right)

Since the flapping mechanism will be operated underwater, control electronics and motors are designed to be placed separately above the water tank. In order to transfer power down to the flapping mechanism, a method inspired by the function of muscles was used. It uses a pair of flexible Teflon tubes which are fixed at both ends with pre-tensioned stainless steel wires running through connecting the motor and the pivoting joint as shown in Figure 2-9. As the motor rotates, the spool fixed on the motor shaft pulls on one side and releases the other, similar to that of muscles on the opposite side of a joint contracts and stretches, causing the end effector to rotate as required. A similar method was also used in previous research to measure the input power and output forces of a robotic bat[35].

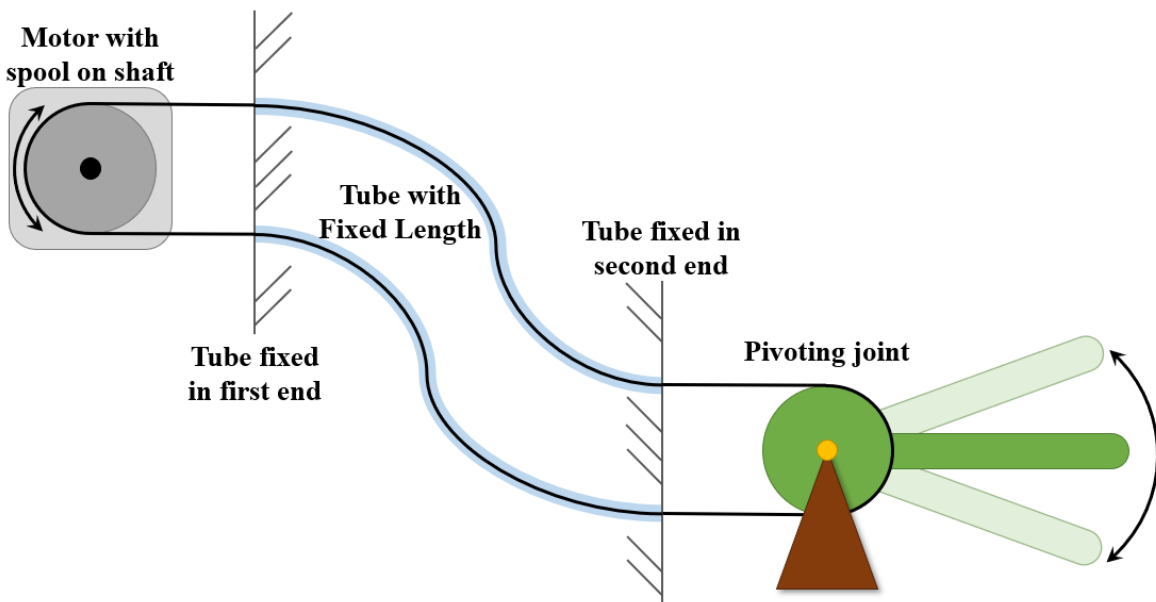


Figure 2-9 Illustration of the actuation mechanism for power transfer

Mechanical components of the flapping robot were mostly 3D-printed with an FDM printer using PLA where components that require precision and smoothness such as driving shafts are machined out for steel and aluminum alloy.

## **2.3 Electronic and Control System**

### **2.3.1 Motor & Driver**

Considering to reduce the complexity of the flapping-wing robot, stepper motors are chosen to control the mechanism. In contrast to standard servo motors, stepper motors provide high accuracy in angular position and angular rates without the need of encoders to provide feedback signals. This allows the control algorithm to be simplified to an open-loop control system instead of a closed-loop control system where suitable feedback gains and controllers should be designed to obtain an optimal motor response.

The stepper motors used in this research are NEMA17 bipolar stepper motors (Figure 2-10), which are commonly used in wide varieties of commercial 3D-printers nowadays. They are inexpensive, easily available and only requires simple driver circuits which are suitable for the current application. The electrical and mechanical characteristics of the NEMA17 stepper motor are listed in Table 2-2.

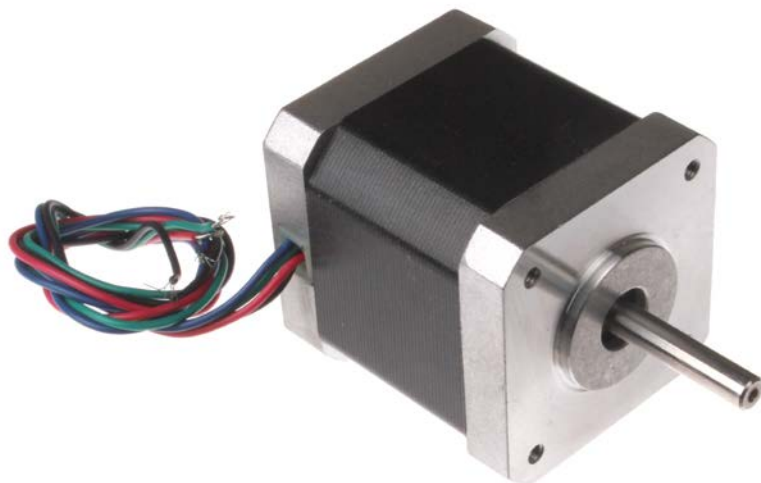


Figure 2-10 NEMA17 bipolar stepper motor

Table 2-2 Characteristics of the NEMA17 stepper motor

Characteristics	Value
Voltage	4.24~24 V
Current	0.8 A
Degree per Step	1.8 °
Static Torque	4.0 kg · cm

DRV8825 driver boards are used to power and control to stepper motors (Figure 2-11). They have great current delivering capabilities and can be configured to perform up to 1/32 microstepping which give an angular positional resolution of 0.056 degrees per step (Table 2-3). Furthermore, they are also inexpensive, commonly used and highly compatible for different applications.



Figure 2-11 DRV8825 stepper motor driver board

Table 2-3 Characteristics of the DRV8825 stepper motor driver

Characteristics	Value
Motor Voltage	8.2 ~ 45 V
Reference Voltage	1 ~ 3.5 V
Maximum Current	2.5 A
Microstepping	$1$ , $\frac{1}{2}$ , $\frac{1}{4}$ , $\frac{1}{8}$ , $\frac{1}{16}$ , $\frac{1}{32}$

### 2.3.2 Controller Board

In order to simultaneously control ten stepper motors, a powerful controller board with a large amount of I/O ports available is required. A Raspberry Pi 3 model B microcontroller board (Figure 2-12) is selected since there are a total of 40 GPIO pins available and also easily programmable with its graphical user interface using python, C++ or other languages. In this research, the control algorithm, which will be further discussed in the following chapter, is written in python code. The specifications of the microcontroller board are listed in Table 2-4.



Figure 2-12 Raspberry Pi 3 model B microcontroller board

Table 2-4 Specifications of the Raspberry Pi 3 model B microcontroller board

Items	Specs
CPU	BCM2837 (Quad Core; 1.2 GHz; 64 bit)
RAM	1 GB
GPIO Pins	40
USB Port	4 USB 2.0
Display Port	Composite RCA; HDMI



## **2.4 Completed Flapping-wing Robot**

### **2.4.1 Robot Assembly**

The completed robot assembly consists of 3 main components: the flapping mechanism, the control box and the force measurement system as shown in Figure 2-13.

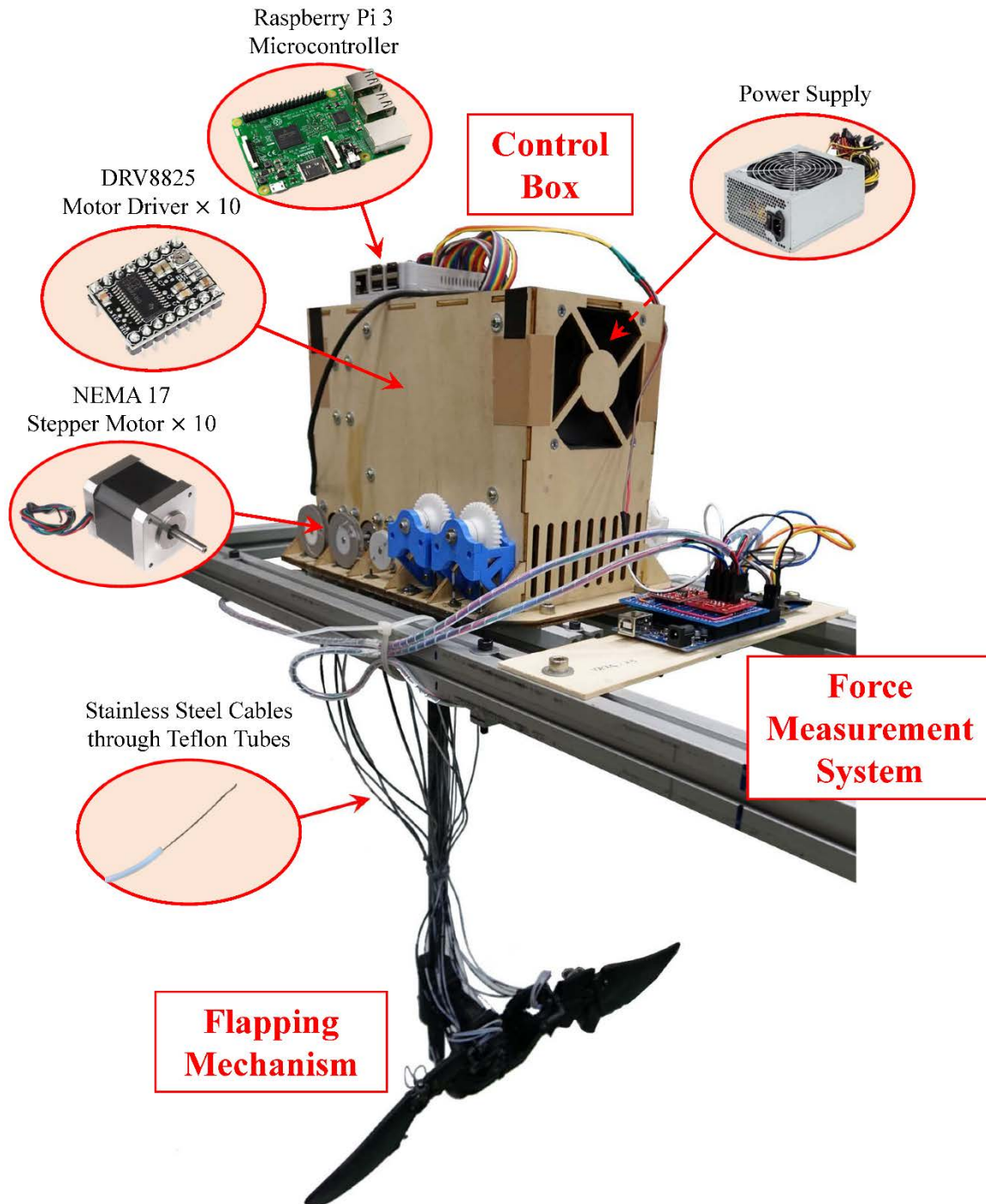


Figure 2-13 Robot Assembly

## 2.4.2 Flapping Mechanism

The assembled flapping mechanism, which is spray-painted black to reduce reflection during experiments, is shown in Figure 2-14. The shoulder joints control flapping, arm-sweeping and twisting angles; the wrist joints control folding and hand-sweeping angles.

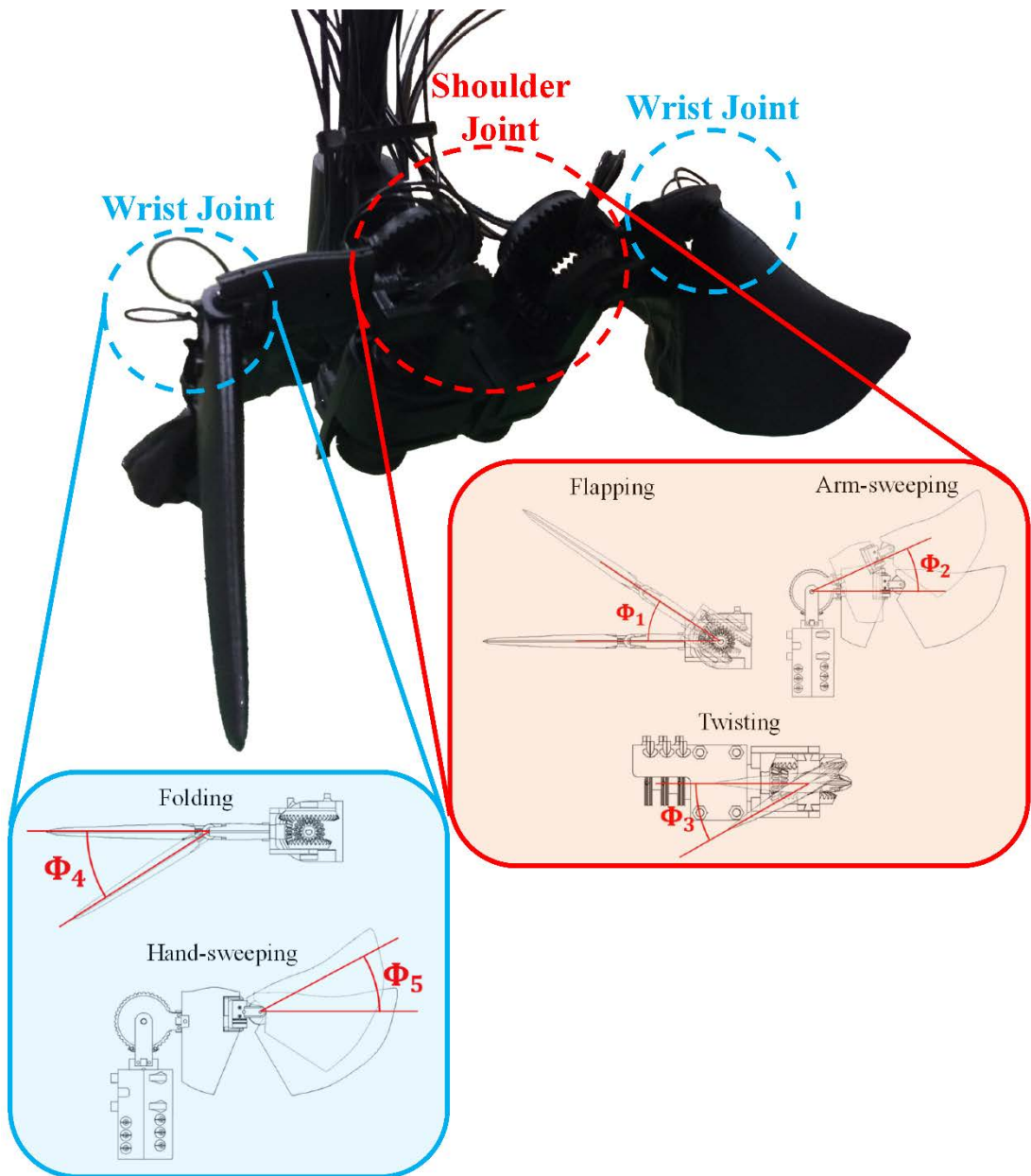


Figure 2-14 Joints and DOFs of the flapping mechanism

### **2.4.3 Control Algorithm**

The motor control code was written in python. Since stepper motors do not require feedback signals, the complexity of the control algorithm can be greatly reduced. Furthermore, the drivers for each stepper motor only required mainly 2 control signals from the control board, one controls the rotational direction and the other controls the steps to move. The control algorithm runs according to the following process:

1. Read the desired mechanical kinematic angles from a text file.
2. Transfer mechanical kinematic angles into motor angles.
3. Calculate the required step signals for each time intervals.
4. Move the robot from the resting position into the initial position.
5. Start the flapping motion until the preset maximum cycle count is met.
6. Move the robot back to the resting position.

During the flapping process, in addition to simply controlling the motors, a triggering signal will be sent through a designated GPIO port in order to trigger the data collection of the force balance and the high-speed camera at the current moment.

## **2.5 Mathematical Representation of Kinematics**

### **2.5.1 Denavit-Hartenberg Convention**

In order to understand how the angular position of each DOF on the joints affect the entire kinematics of the mechanism, a mathematical model should be formulated. Since the designed mechanism contains only a spherical joint in the form of a bevel-gear train at the shoulder and two revolute joints at the wrist, these lower-pair kinematic joints can be represented by a method called the Denavit-Hartenberg Convention, which is a matrix-based kinematic representation of mechanisms that was first introduced by Jacques Denavit and Richard S. Hartenberg in 1955[36].

Denavit-Hartenberg Convention, or often briefly written as D-H convention, uses four parameters, known as DH parameters, with a particular notation convention that describes the coordinate transformation between attached reference frames of a kinematic linkage. For example, reference frames are attached to each member of a 3-bar linkage as shown in Figure 2-15 in accordance with the D-H convention.

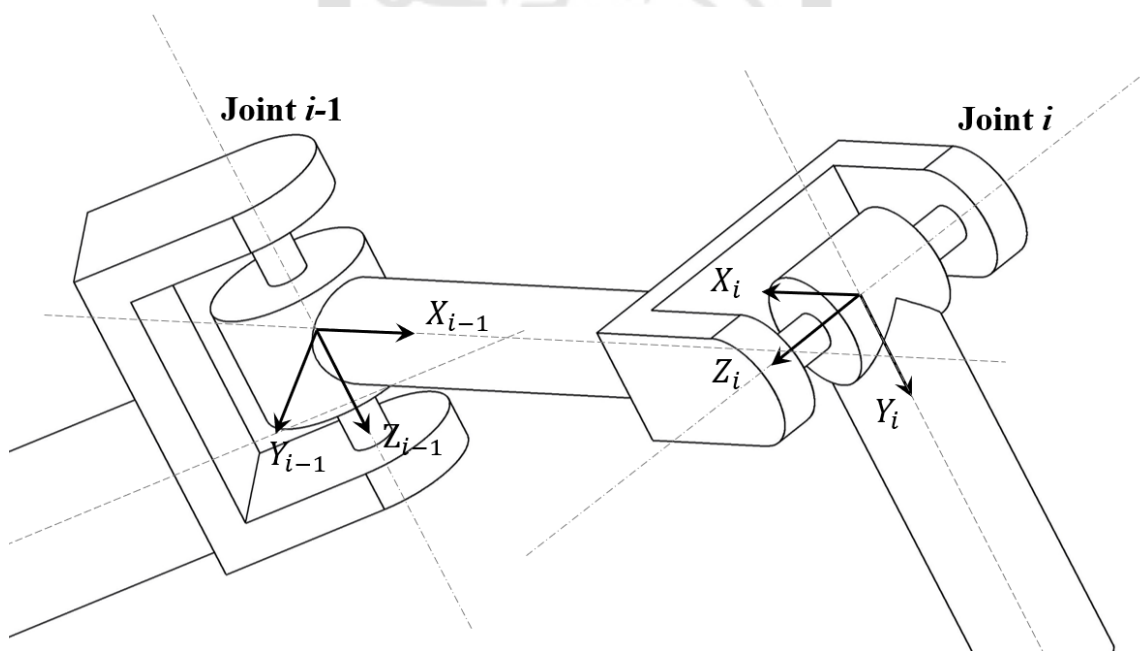


Figure 2-15 Sketch of attached frames according to the D-H convention

The four DH parameters between each frame can be found by observing the relative position of each frame as follows:

### 7. Joint offset ( $d_i$ )

The offset distance of the two successive joints which is defined as the distance measured between  $X_{i-1}$  and  $X_i$  along the previous joint axis  $Z_{i-1}$ . This distance is a variable if joint  $i$  is a prismatic joint.

### 8. Joint Angle ( $\theta_i$ )

The rotational angle of joint  $i$  which is defined as the angle measured between  $X_{i-1}$  and  $X_i$  about the joint axis  $Z_i$ . This angle is a variable if joint  $i$  is a revolute joint.

### 9. Link Length ( $a_i$ )

The length between joint  $i$  and  $i - 1$  which is defined as the distance measured between  $Z_i$  and  $Z_{i+1}$  along  $X_i$ . For a revolute joint, this parameter is sometimes referred to as  $r_i$  in some articles, since it represents the radius about the previous joint  $Z_{i-1}$ .

### 10. Twist Angle ( $\alpha_i$ )

The twist angle between the joint axes which is defined as the angle measured about  $X_i$  from  $Z_{i-1}$  and  $Z_i$ .

The transformation, including translation and rotation, from frame  $i$  to frame  $i - 1$  can be formulated as the following matrix. By successively transforming through the entire mechanism, local coordinates on the linkages can be represented in global coordinates for further kinematic analysis.

$${}^{i-1}T_i = \begin{bmatrix} \cos(\theta_i) & -\sin(\theta_i) \cos(\alpha_i) & \sin(\theta_i) \sin(\alpha_i) & a_i \cos(\theta_i) \\ \sin(\theta_i) & \cos(\theta_i) \cos(\alpha_i) & -\cos(\theta_i) \sin(\alpha_i) & a_i \sin(\theta_i) \\ 0 & \sin(\alpha_i) & \cos(\alpha_i) & d_i \\ 0 & 0 & 0 & 1 \end{bmatrix} \quad (2-17)$$

In order to analyze the kinematics of the designed flapping mechanism used in this research, local frames of reference are attached to each linkage following the Denavit-Hartenberg convention as shown in Figure 2-16 thus the DH parameters can also be found according to the definitions described previously and are listed in Table 2-5.

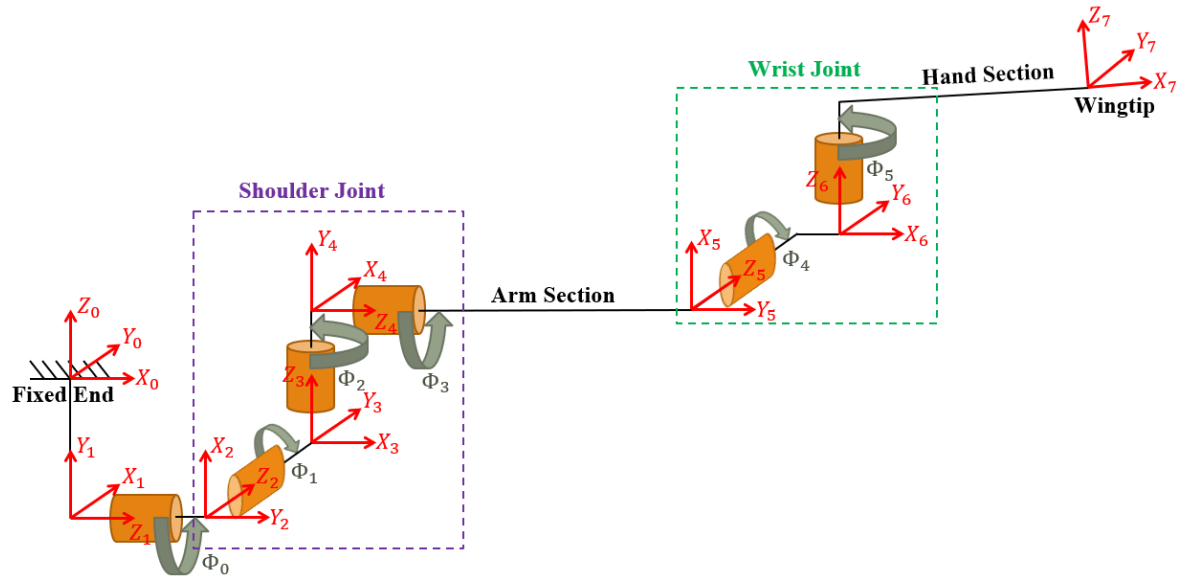


Figure 2-16 Sketch of attached frames of the designed flapping mechanism

Table 2-5 DH parameters of the designed flapping mechanism

Joint	DOF	$\theta_i$	$\alpha_i$	$d_i$	$a_i$
Body		90°	90°	0 mm	0 mm
	Body Angle	$90^\circ + \Phi_0$	90°	0 mm	0 mm
Shoulder	Flapping	$90^\circ + \Phi_1$	90°	0 mm	0 mm
	Sweeping	$90^\circ + \Phi_2$	90°	0 mm	0 mm
Wrist	Twisting	$90^\circ + \Phi_3$	90°	67.25 mm	0 mm
	Folding	$90^\circ + \Phi_4$	90°	6.5 mm	14.5 mm
	Hand Sweeping	$10.42^\circ + \Phi_5$	0°	0 mm	95.698 mm

## 2.5.2 Kinematics of the Bevel-gear Train

The implementation of a bevel-gear train at the shoulder joint provides a compact solution for simultaneous control of an equivalent spherical joint with three degrees of freedom. However, the three inputs are coupled together to provide individual outputs of flapping, sweeping and twisting motion of the shoulder joint. Thus, a graphical method was used to analyze the kinematics of the bevel-gear train[37].

The functional representation of the bevel-gear train at the shoulder joint is shown in the left of Figure 2-17. The mechanism can be separated into 7 members where the label 1 is a fixed base and links 2, 6 and 7 are connected to the three control inputs ( $\Psi_1$ ,  $\Psi_2$  and  $\Psi_3$ ). The rotational motions are then transferred through 3 gear pairs, which are gear 7 to 3, 6 to 5 and 5 to 4, to the end effector attached to gear 4, which in this case is the beam of the arm section.

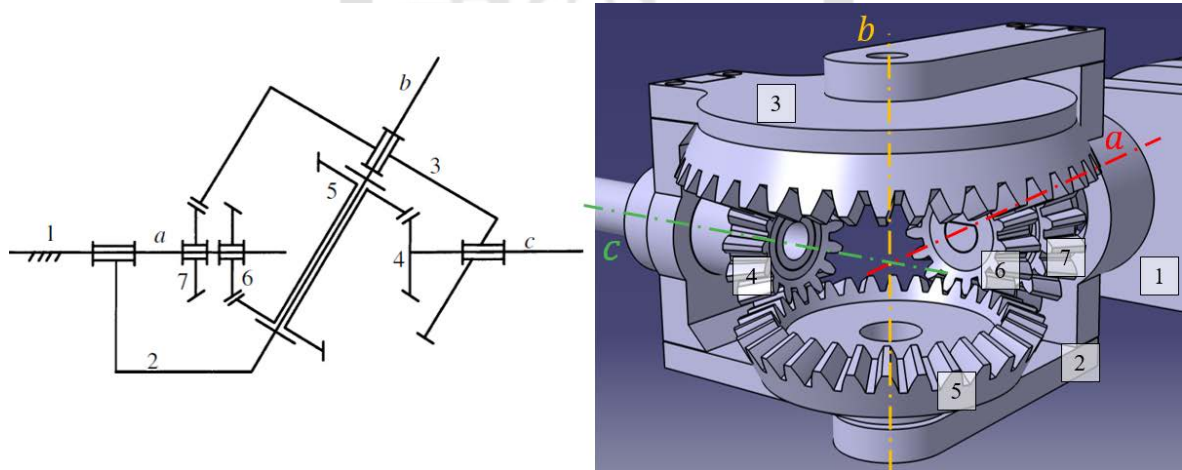


Figure 2-17 Functional schematic of a bevel-gear train[37] (left) and the corresponding members labeled in the CAD design (right)

In order to control the flapping angle ( $\Phi_1$ ) about the  $a$ -axis, all three inputs (link 2, 6, and 7) should rotate simultaneously. Moreover, sweeping angle ( $\Phi_2$ ) is controlled only by rotating link 6 and 7. Finally, the twisting angle ( $\Phi_3$ ) is directly controlled by link 7. This coupled relation can be easily represented by the following matrix:

$$\begin{bmatrix} \Phi_1 \\ \Phi_2 \\ \Phi_3 \end{bmatrix} = \begin{bmatrix} 1 & 0 & 0 \\ -n_{73} & n_{73} & 0 \\ n_{54}(n_{73} - n_{65}) & -n_{54}n_{73} & n_{54}n_{65} \end{bmatrix} \begin{bmatrix} \Psi_1 \\ \Psi_2 \\ \Psi_3 \end{bmatrix} \quad (2-18)$$

where  $n_{ij}$  represents the gear ratio from link  $i$  to link  $j$ . After substituting the gear ratios with those of the designed flapping mechanism and rearranging the equation, the control inputs required to obtain desired shoulder joint kinematics can be derived. Combined with the direct drive pulleys with reduction ratio of the wrist joint, the kinematic transformation matrix from mechanical kinematic angles ( $\Phi$ ) to motor angles ( $\Psi$ ) is shown below.

$$\begin{bmatrix} \Psi_1 \\ \Psi_2 \\ \Psi_3 \\ \Psi_4 \\ \Psi_5 \end{bmatrix} = \begin{bmatrix} 1 & 0 & 0 & 0 & 0 \\ 1 & 2 & 0 & 0 & 0 \\ 1 & -2 & 1 & 0 & 0 \\ 0 & 0 & 0 & \frac{3}{2} & 0 \\ 0 & 0 & 0 & 0 & 3 \end{bmatrix} \begin{bmatrix} \Phi_1 \\ \Phi_2 \\ \Phi_3 \\ \Phi_4 \\ \Phi_5 \end{bmatrix} \quad (2-19)$$

# **CHAPTER III**

## **Wing Trajectory and Kinematic Analysis**

This chapter elaborates on the derivation of kinematics angles and motor angles for the flapping-wing robot according to previous research and the verification of the kinematic trajectories performed by the robot to ensure proper tracking for each angle.

### **3.1 Reference Kinematics**

#### **3.1.1 Previously Observed Wing Kinematics**

Hovering passersines present complicated wing kinematic which was observed by researchers in National Taiwan University (NTU) using highspeed cameras. Five reference kinematic angles ( $\Theta$ ) were defined to characterize the hovering flight motion of the passerine which are flapping ( $\Theta_1$ ), twisting ( $\Theta_2$ ), folding ( $\Theta_3$ ), arm-sweeping ( $\Theta_4$ ) and hand-sweeping angles ( $\Theta_5$ ). Definition of the above angles will only be briefly covered here in Figure 3-1 since detailed description can be found in previous works[20, 38]. Note that these angles should not be confused with the mechanical kinematic angles ( $\Phi$ ) described in the previous chapter despite the similarity in names.

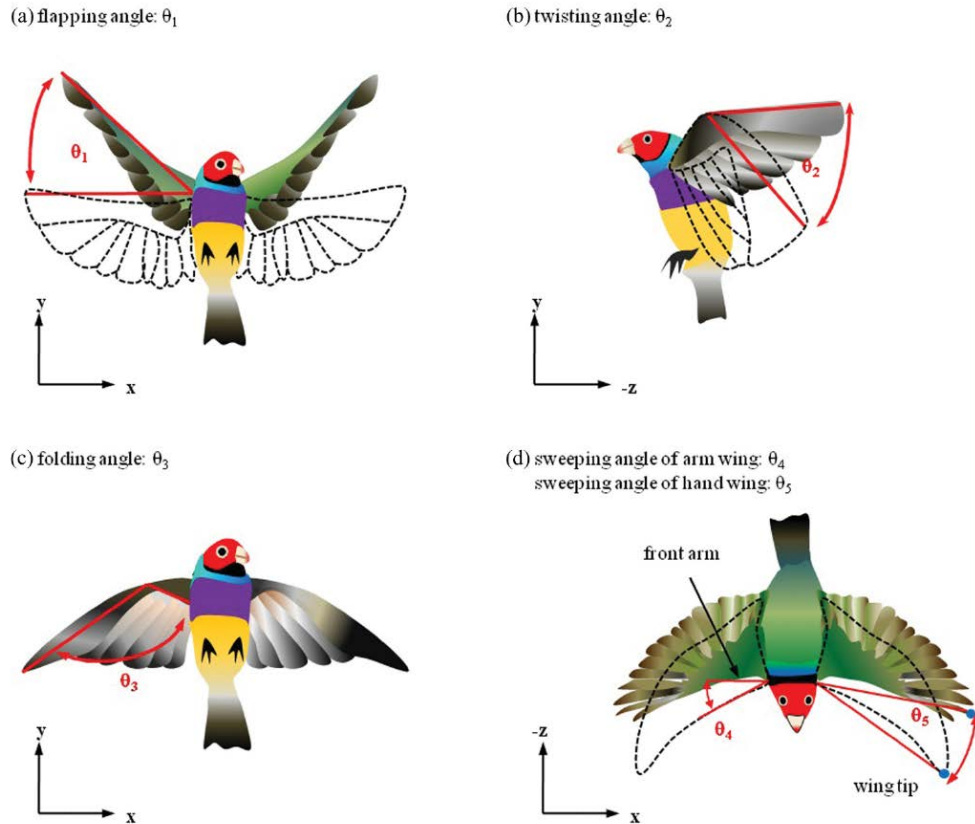


Figure 3-1 Illustration of reference kinematic angles[20]

Figure 3-2 shows how the five reference kinematic angles change throughout a wingbeat cycle during hovering flight. Although the data was observed with the aid of highspeed cameras, it is quite surprising that the all reference angles do not start and end at the same exact angle and some even exists differences of over 20 degrees. This is possibly due to errors while identifying feature points or the bird simply did not flap identically each and every wingbeat. Furthermore, the fact that the data were averaged through several wingbeat cycles could also lead to some deviation. Consequently, the raw data could not be directly used in this study since it would result in discontinuous motor inputs between wingbeat cycles. In order to obtain continuous kinematic angles, an eighth-order Fourier series were used for regression of each reference kinematic angles. By setting the period of the series to 1, this results in curves that start and end at the exact same angles within a cycle as shown in Figure 3-3.

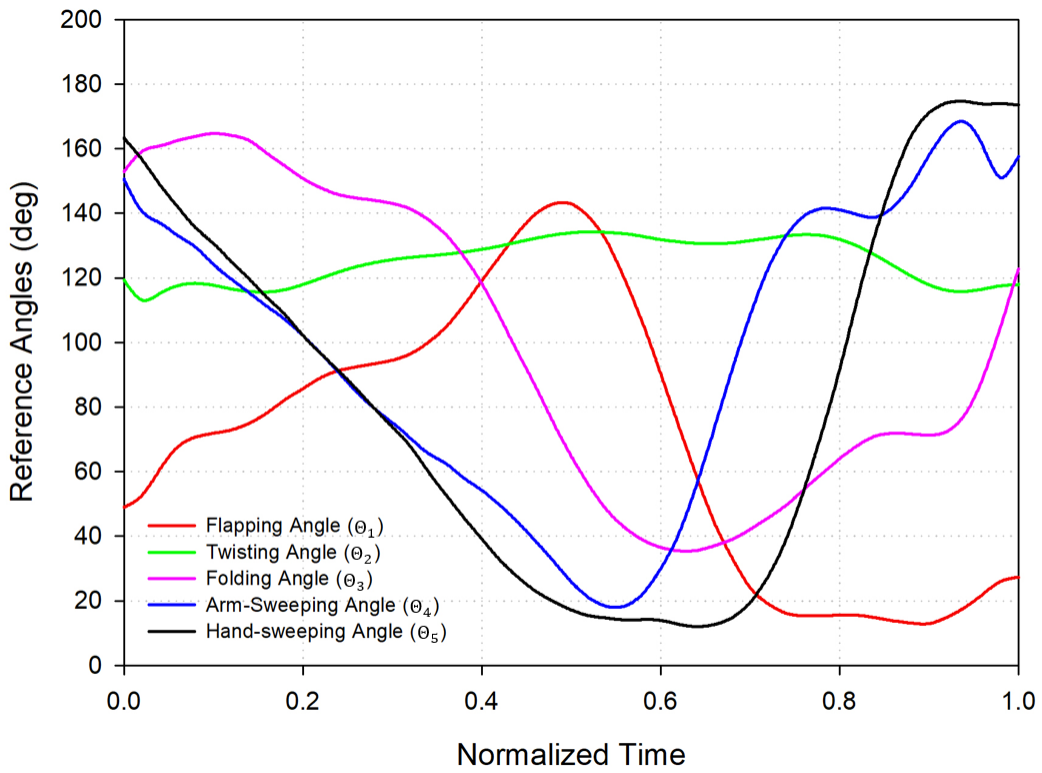


Figure 3-2 Observed reference kinematic angles within a wingbeat cycle (redrawn with datapoints adopted from [38])

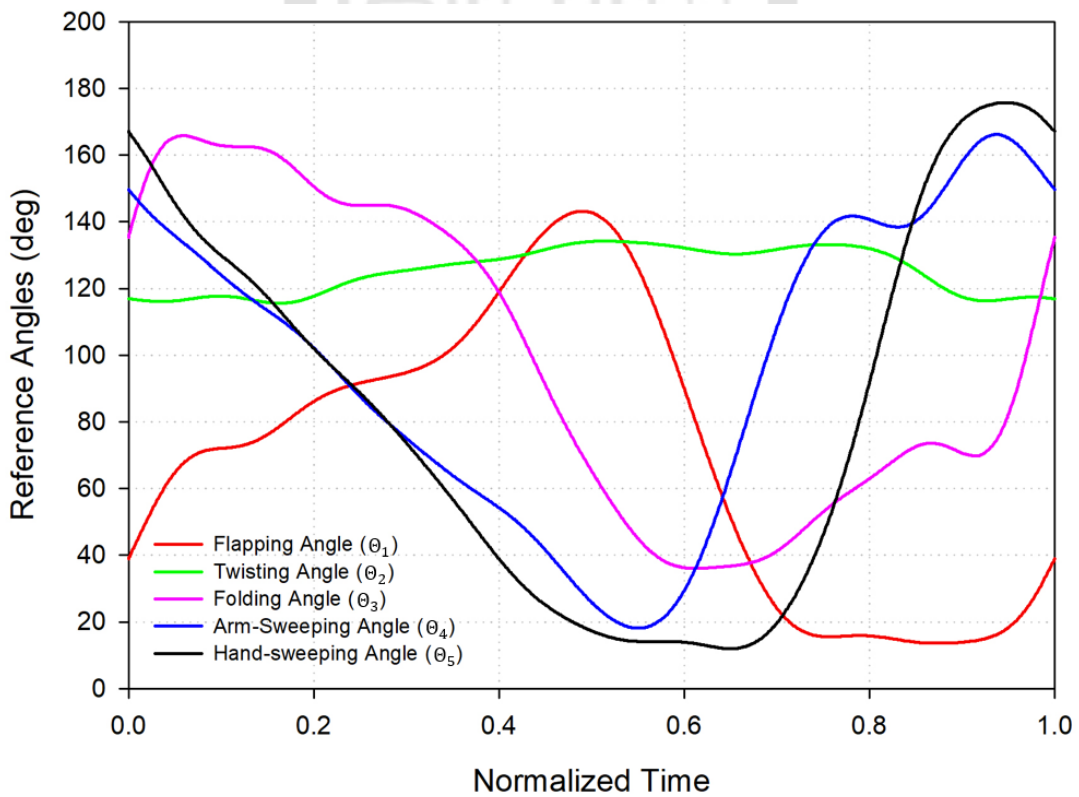


Figure 3-3 Eighth-order Fourier series regression curve of reference kinematic angles

### **3.1.2 Solving for the Mechanical Kinematic Angles**

The reference angles are then split into timesteps and the transformation to mechanical kinematic angles are solved for each timestep separately. However, the transformation from reference kinematic angles to mechanical kinematic angles consists of five unknowns and highly coupled nonlinear trigonometric functions thus can only be solved through nonlinear numerical solvers. However, using solvers such as that built-in in MATLAB could possibly lead to unsolvable situations where the flapping mechanism is unable to perfectly replicate the reference kinematics. Under these circumstances, a sub-optimal solution should be found in order to complete the wingbeat cycle. Thus, a custom binary genetic algorithm (GA) code was written in MATLAB to solve the problem. The GA optimization solver architecture is shown in Figure 3-4.

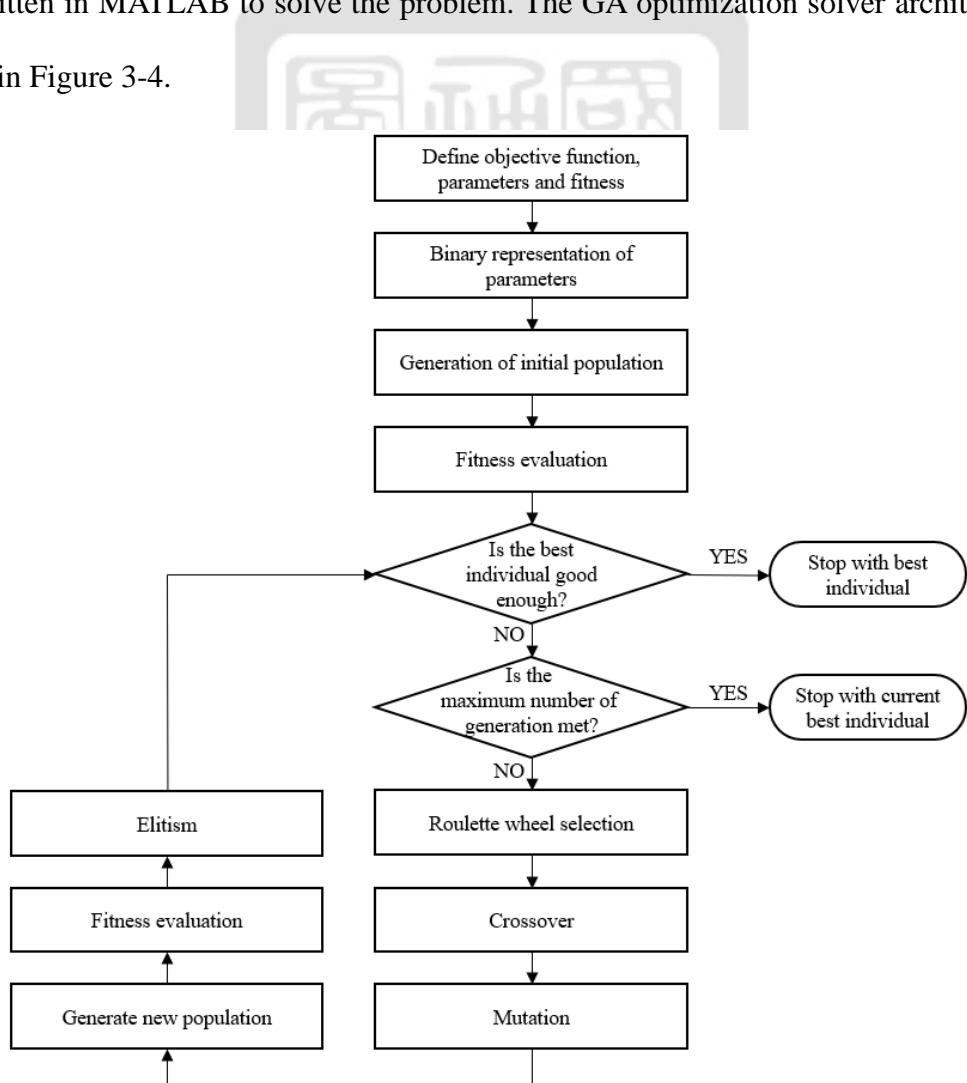


Figure 3-4 Flow chart of the binary genetic algorithm optimization process

The transformation for each timestep ( $t$ ) was formulated into an optimization problem with the design variables being the five mechanical kinematic angles at the timestep which are represented as

$$\Phi(t) = \begin{bmatrix} \Phi_1(t) \\ \Phi_2(t) \\ \Phi_3(t) \\ \Phi_4(t) \\ \Phi_5(t) \end{bmatrix}, \text{ subjected to } \begin{cases} -\frac{\pi}{2} \leq \Phi_1 \leq \frac{\pi}{2} \\ -\frac{\pi}{2} \leq \Phi_2 \leq \frac{\pi}{2} \\ -\frac{\pi}{2} \leq \Phi_3 \leq \frac{\pi}{2} \\ 0 \leq \Phi_4 \leq \pi \\ -\frac{\pi}{2} \leq \Phi_5 \leq \frac{\pi}{2} \end{cases} \quad (3-1)$$

Through the Denavit-Hartenberg representation derived in the previous chapter, a set of  $\Theta_i(t)$  that corresponds to the  $\Phi(t)$  of the individual can be obtained. The objective function to be minimized is then defined as the square of the summation of differences between each  $\Theta_i(\Phi(t))$  and the reference kinematic angles ( $\Theta_i^{ref}(t)$ ) from the Fourier regression curve which is expressed as follows

$$f(\Phi(t)) = \sum_{i=1}^5 [\Theta_i(\Phi(t)) - \Theta_i^{ref}(t)]^2 \quad (3-2)$$

Since GA optimizes the design variables through maximizing the fitness value, thus the fitness is defined as the inverse of the function value  $f(\overline{\Phi(t)})$  as shown below

$$fitness(\Phi(t)) = \frac{1}{f(\Phi(t)) + 1} \quad (3-3)$$

where the 1 in the denominator is purposely added to prevent occasions where the function value equals to zero leading to an undefined fitness value.

The optimization results of mechanical kinematic angles are shown in Figure 3-5 which shows that the algorithm successfully came up with continuous results for  $\Phi_1$  through  $\Phi_4$

but failed to solve the last angle  $\Phi_5$ . The optimized data points of  $\Phi_5$  results in discontinuous curve after 40% of the wingbeat cycle and even maxed out at the limits twice. Furthermore, Figure 3-6 shows the reference kinematic angles corresponding to the optimized mechanical kinematic angles compared with the original reference curve. Unsurprisingly, the result tracked  $\Theta_1$  to  $\Theta_4$  perfectly but  $\Theta_5$ , which is controlled by the wrist joint, exists unacceptable deviation from the reference curve.



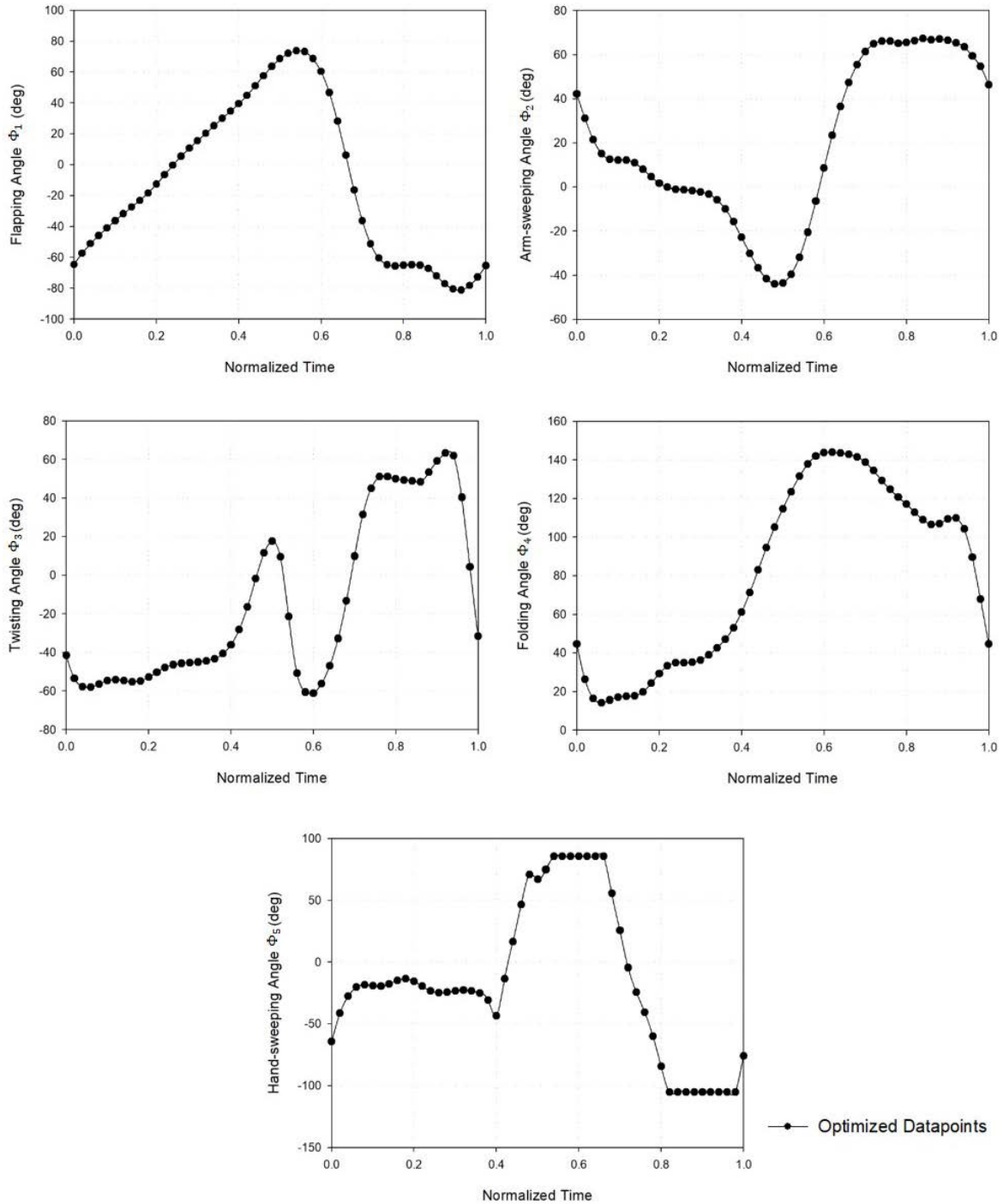


Figure 3-5 Results of mechanical kinematic angles ( $\Phi$ ) using GA optimization process

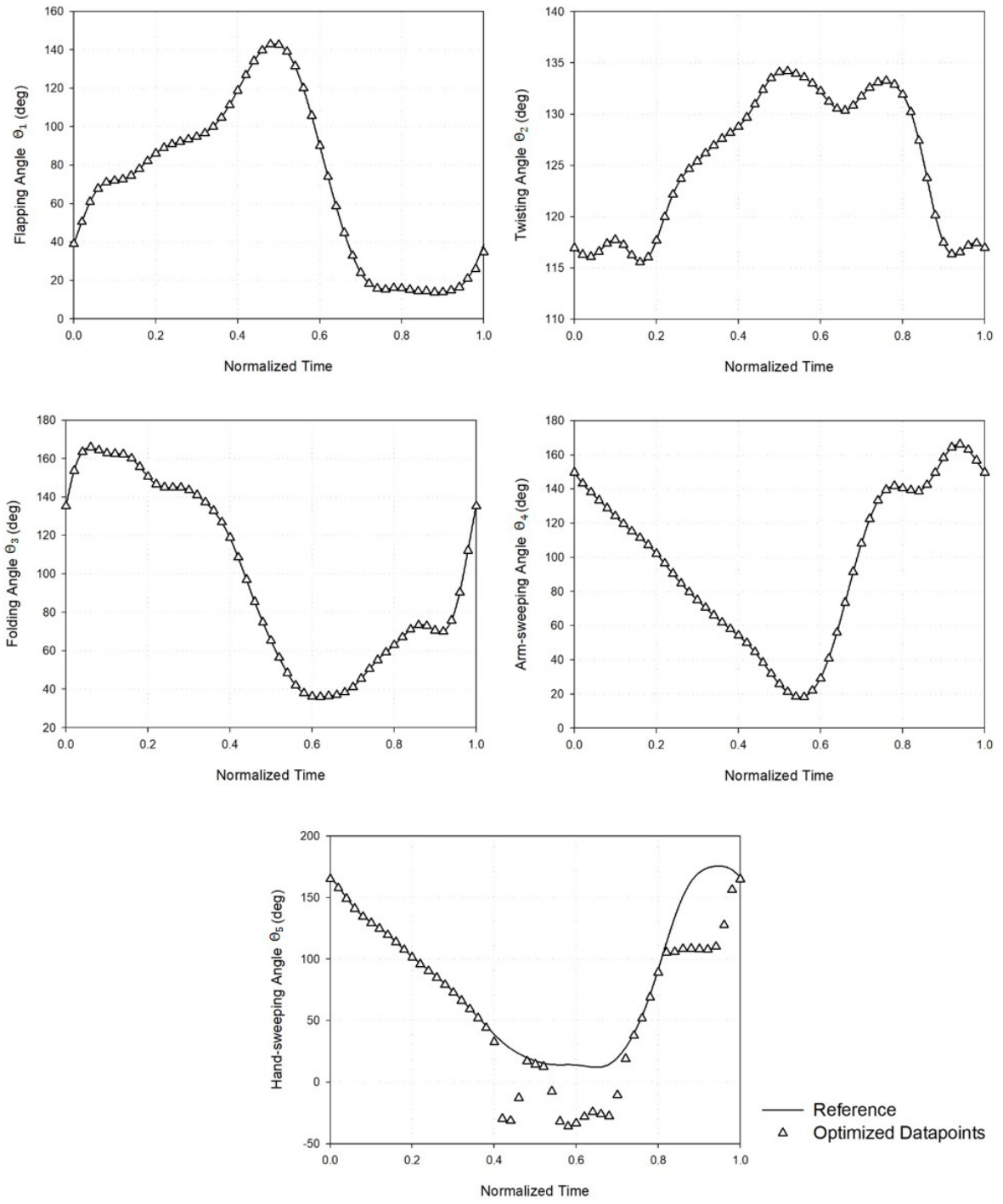


Figure 3-6 Results of reference kinematic angles ( $\Theta$ ) using GA optimization process compared with the original reference

After analyzing the results from Figure 3-5 and Figure 3-6, there are several possible reason that caused the GA solver to fail:

### **1. Inaccurate observation of reference kinematics**

The original reference kinematic angles were captured by high-speed cameras and feature points were manually identified and selected without the aid of markers on the bird. Thus, it is highly possible that the reference angles are not accurate at certain intervals where the image might be unclear or that some feature points being obstructed by the wing itself.

### **2. Flexibility of bird's wings**

The wings of a bird are fully covered with feathers which are flexible and also capable of deforming, folding and overlapping. This could lead to possible additional movement of the feature points. However, the designed flapping-wing mechanism was constructed with rigid components since it will take great effort to properly mimic the morphing characteristics.

### **3. Kinematic restriction of designed flapping-wing mechanism**

The structure of a bird's wing consists of bones like human arms, this provides complicated high DOF movements which the simplified 5-DOF mechanism could possibly be unable to fully replicate.

Although the mechanism is unable to perfectly mimic the movement at the wrist joint, the kinematics at the shoulder joint appears to be reasonably achievable. Furthermore, the original reference folding motion causes two wings to collide. Thus, in this research, the wrist kinematics are simplified to simple folding motion with two proposed folding amplitudes, which are shown in Figure 3-7, while the shoulder kinematics being programmed to follow the reference kinematics.

Experimental case 1 has the exact same folding amplitude as the reference kinematics. However, to prevent the wings from colliding at  $T=0.5$ , time stamp of each data point was modified using the following equation:

$$t_{modified} = t_{ref}^{0.7} \quad (3-4)$$

This shifts the curve towards the right-hand side which delays the time where folding happens. Experimental case 2 has the same maximum value of folding angle but the folding amplitude was halved compared with case 1.

Different folding kinematics are expected to lead to variation in the aerodynamic effect after the point of stroke-reversal from downstroke to upstroke. According to Feshalami et al.[24], as the wing folding amplitude increases, the averaged lift production also increases along with a reduction in power input during forward flight. Thus, in this present research, it is expected that a less-folding amplitude will also create a much greater negative force during upstrokes in hovering conditions which will decrease the overall lift produced.

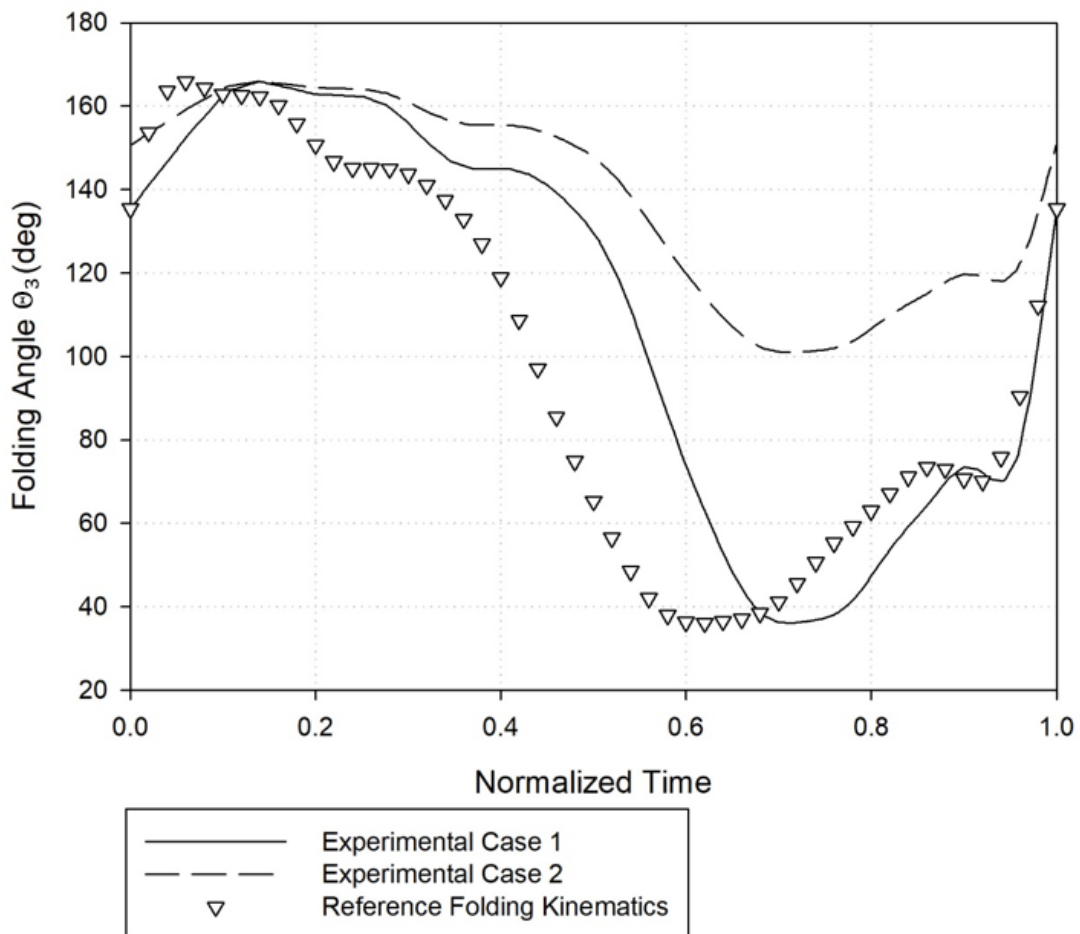


Figure 3-7 Proposed folding motion and reference kinematics

## 3.2 Kinematic Analysis

### 3.2.1 Objective

After determining how each DOF of flapping-wing mechanism will move through a wingbeat cycle, it is necessary to verify that the actual output of the mechanism is what initially desired. This process is essential in order to confirm that the previous transformations are correct and also make sure that the mechanical linkages are performing as expected.

### 3.2.2 Experimental Method

In order to reconstruct the three-dimensional motion of the mechanism, a direct linear transformation (DLT) method was implemented, which is used to convert feature points in a set of stereoscopic images into three-dimensional coordinates. The detailed description and principle of the DLT will only be briefly covered in this section since it could be found in several sources[39-41]. Four feature points on each wing were clearly marked with colored pins attached to the mechanical wings as shown in Figure 3-8.

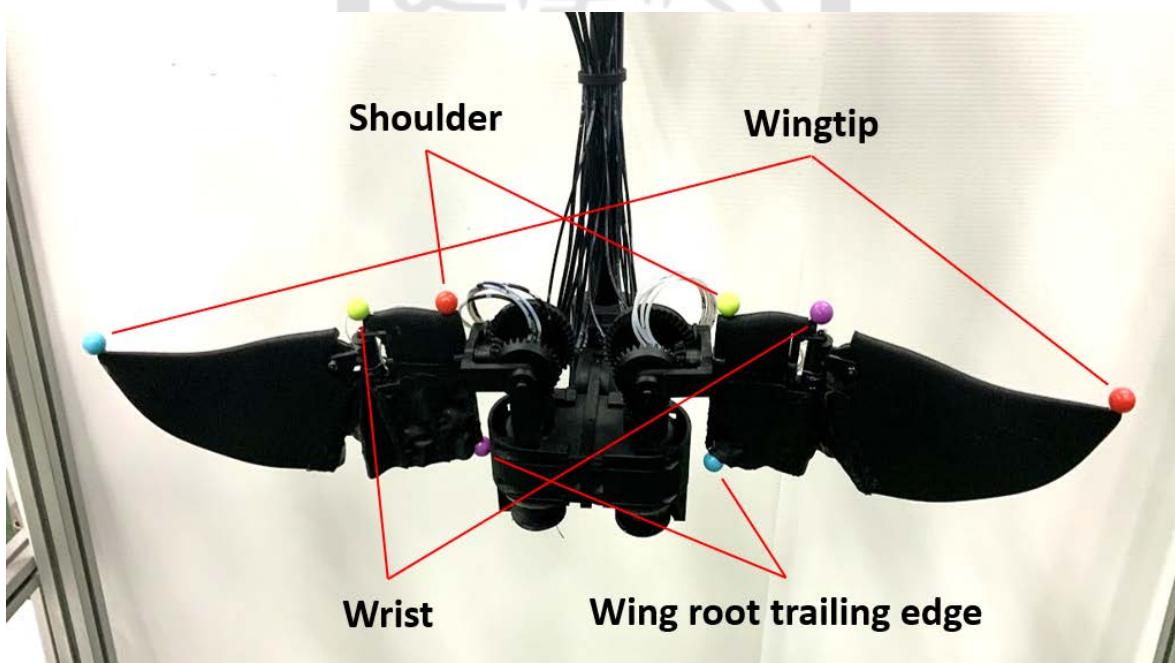


Figure 3-8 Feature points marked for kinematic analysis

The image acquisition process was conducted with 3 DSLR cameras setup as in Figure 3-9 to provide redundancy in case of feature points being block at certain angles. Since the mechanism moves at a fairly slow rate, the cameras were set to capture at 30 frames per second with shutter speed set to  $1/200$  of a second at a resolution of  $1920 \times 1080$  pixels.

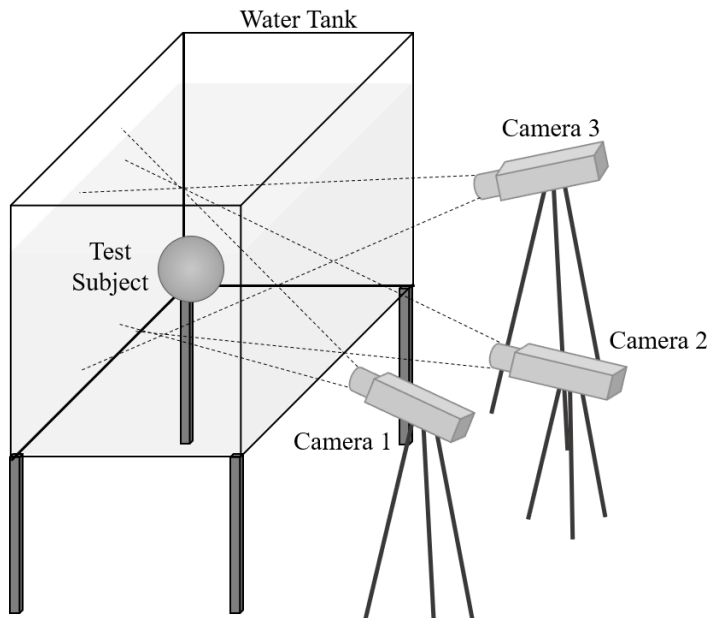


Figure 3-9 Experimental setup for kinematic analysis

Prior to the actual experiment, calibration of the cameras was done by capturing a  $150 \times 150 \times 150$  mm<sup>3</sup> calibration cube which was made of 2 mm straight copper wire soldered into a grid pattern with a total of 64 calibration points evenly spread as shown in Figure 3-10.

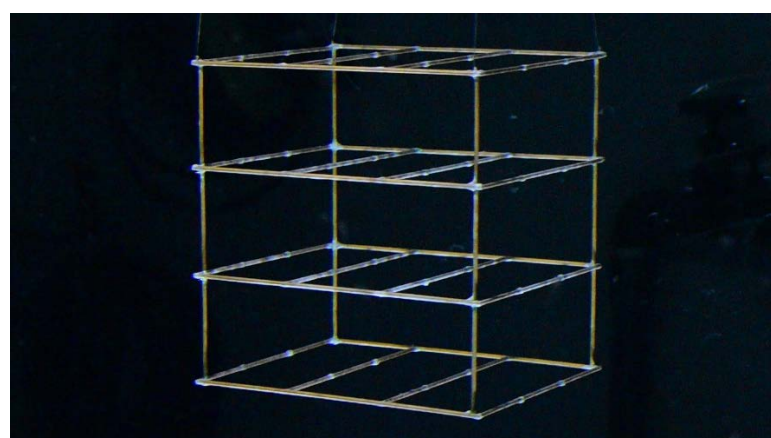


Figure 3-10 Calibration Cube

The objective of the calibration process is to find the transformation vector  $\mathbf{L}$  and  $\mathbf{R}$ .

For example, the vector  $\mathbf{L}$  could be found with the following matrix of equations:

$$\begin{bmatrix} x_1 & y_1 & z_1 & 1 & 0 & 0 & 0 & 0 & -u_{L1}x_1 & -u_{L1}y_1 & -u_{L1}z_1 \\ 0 & 0 & 0 & 0 & x_1 & y_1 & z_1 & 1 & -v_{L1}x_1 & -v_{L1}y_1 & -v_{L1}z_1 \\ x_2 & y_2 & z_2 & 1 & 0 & 0 & 0 & 0 & -u_{L2}x_2 & -u_{L2}y_2 & -u_{L2}z_2 \\ 0 & 0 & 0 & 0 & x_2 & y_2 & z_2 & 1 & -v_{L2}x_2 & -v_{L2}y_2 & -v_{L2}z_2 \\ & & & & & & & \vdots & & & \\ x_n & y_n & z_n & 1 & 0 & 0 & 0 & 0 & -u_{Ln}x_n & -u_{Ln}y_n & -u_{Ln}z_n \\ 0 & 0 & 0 & 0 & x_n & y_n & z_n & 1 & -v_{Ln}x_n & -v_{Ln}y_n & -v_{Ln}z_n \end{bmatrix} \begin{bmatrix} L_1 \\ L_2 \\ L_3 \\ L_4 \\ L_5 \\ L_6 \\ L_7 \\ L_8 \\ L_9 \\ L_{10} \\ L_{11} \end{bmatrix} = \begin{bmatrix} u_{L1} \\ v_{L1} \\ u_{L2} \\ v_{L2} \\ \vdots \\ u_{Ln} \\ v_{Ln} \end{bmatrix} \quad (3-5)$$

where  $x_i$ ,  $y_i$  and  $z_i$  ( $i = 1$  to  $n$ ) are the known three-dimensional coordinates of the calibration points and  $n$  is the number of visible calibration points.  $u_{Li}$  and  $v_{Li}$  are the horizontal and vertical pixel location of each calibration point in the left image.  $L_1$  through  $L_{11}$  are the transformation coefficients which consists  $\mathbf{L}$ . In the case of finding  $\mathbf{R}$ , simply substitute  $u_{Li}$ ,  $v_{Li}$  and  $L_1$  through  $L_{11}$  with  $u_{Ri}$ ,  $v_{Ri}$  and  $R_1$  through  $R_{11}$ . If the left-hand side matrix of the equation is named  $\mathbf{F}_L$  and  $\mathbf{F}_R$  and the right-hand side being named as  $\mathbf{G}_L$  and  $\mathbf{G}_R$ , then process of solving  $\mathbf{L}$  and  $\mathbf{R}$  is to simply perform the Moore–Penrose inverse method as shown below.

$$\mathbf{L} = (\mathbf{F}_L^T \mathbf{F}_L)^{-1} \mathbf{F}_L^T \mathbf{G}_L \quad (3-6)$$

$$\mathbf{R} = (\mathbf{F}_R^T \mathbf{F}_R)^{-1} \mathbf{F}_R^T \mathbf{G}_R \quad (3-7)$$

For any given point that is visible in both images, the three-dimensional coordinates can be found using the following equation:

$$\begin{bmatrix} L_1 - L_9 u_L & L_2 - L_{10} u_L & L_3 - L_{11} u_L \\ L_5 - L_9 v_L & L_6 - L_{10} v_L & L_7 - L_{11} v_L \\ R_1 - R_9 u_R & R_2 - R_{10} u_R & R_3 - R_{11} u_R \\ R_5 - R_9 v_R & R_6 - R_{10} v_R & R_7 - R_{11} v_R \end{bmatrix} \begin{bmatrix} x \\ y \\ z \end{bmatrix} = \begin{bmatrix} u_L - L_4 \\ v_L - L_8 \\ u_R - R_4 \\ v_R - R_8 \end{bmatrix} \quad (3-8)$$

where  $u_L$ ,  $v_L$ ,  $u_R$  and  $v_R$  are the horizontal and vertical pixel location of the point in the left image and the right image. Similar to that of solving the transformation coefficients, by denoting the left-hand side matrix as  $\mathbf{Q}$  and the right-hand side as  $\mathbf{q}$ , the three-dimensional coordinate of the point can be solved with:

$$\begin{bmatrix} x \\ y \\ z \end{bmatrix} = (\mathbf{Q}^T \mathbf{Q})^{-1} \mathbf{Q}^T \mathbf{q} \quad (3-9)$$

A custom MATLAB code was written to perform camera calibration and output the three sets of transformation coefficients that corresponds to the possible pairs of the three cameras. The code also automatically identifies the selected feature points throughout the captured video files and gets the three-dimensional coordinates and trajectory of each feature point. The kinematic angles are then calculated according to their definitions.

### 3.2.3 Camera Positioning

While performing the camera calibration process, it was noted that the effect of refraction was an issue and should be investigated since the cameras are place outside of the water tank and any light that are not traveling perpendicular to the water-air interface will be affected by refraction. The investigation into the effect of refraction on the DLT accuracy was first conducted with the setup shown in Figure 3-11. Individual images were captured from a perpendicular position from the water tank (0 degree) to 50 degrees from the centerline.

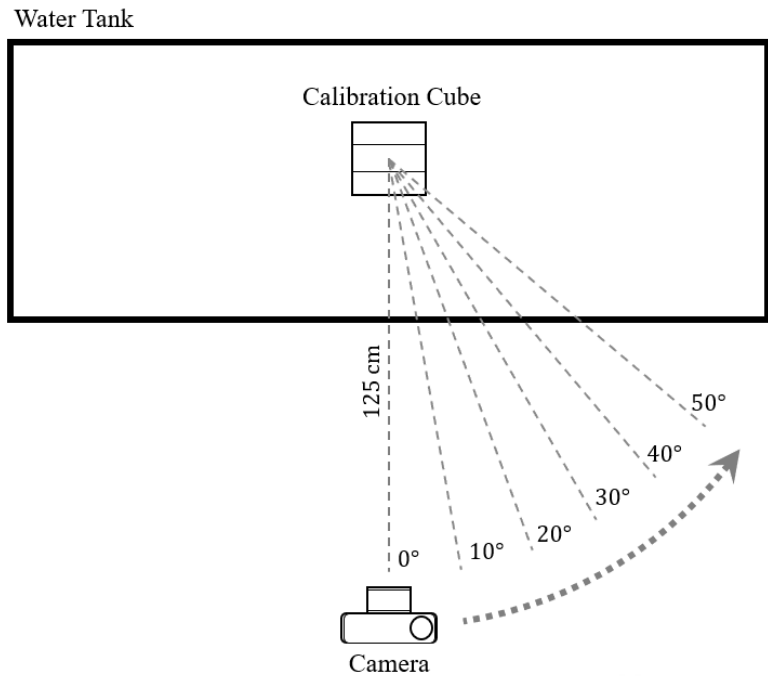


Figure 3-11 Top view illustration of the refraction experiment

Although the camera was rotated about the center of the calibration cube throughout the experiment, it was obvious that the calibration cube in the images did not stay in the center as it should when the camera angle was increased as shown in Figure 3-12. Moreover, the image of the cube moved to the left and was also slightly distorted due to the effect of refraction. Each image from 10 to 50 degrees was paired with the 0-degree image to perform DLT calibration and the mean error along with maximum error are shown in Figure 3-13.

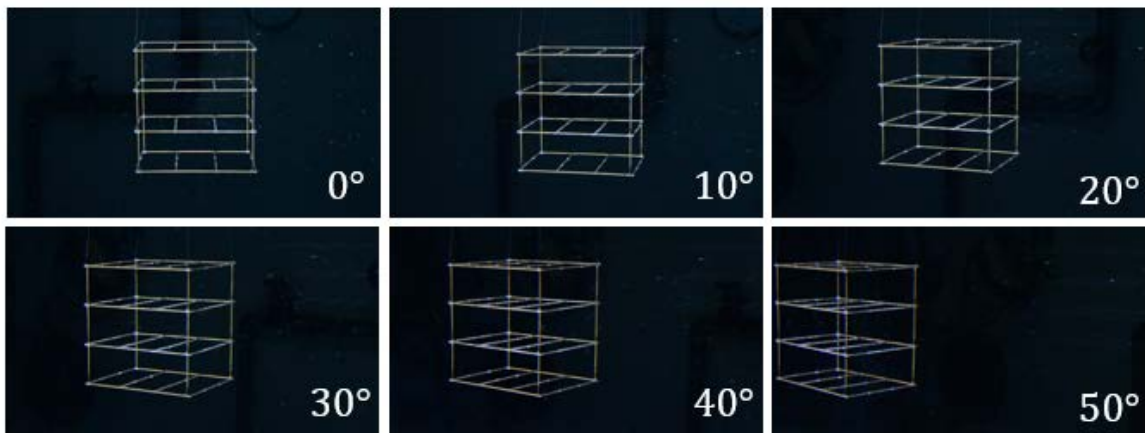


Figure 3-12 Image captured in the refraction experiment

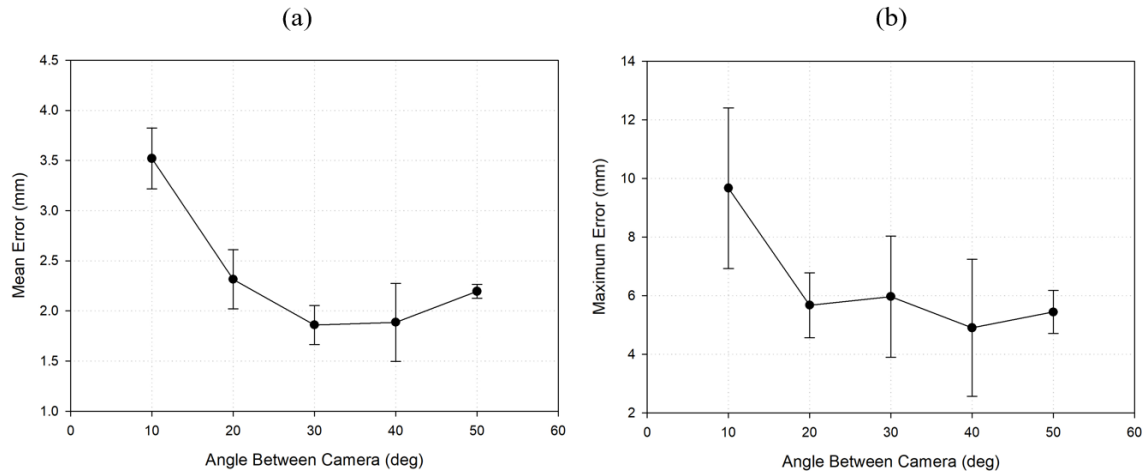


Figure 3-13 (a) Mean error (b) Maximum error of DLT method in refraction experiment ( $n = 64$  with 4 samples)

There are two major observations in this experiment. First, both the mean error and maximum error exist significantly greater values while the angles between two cameras are small and then reduce as the angles were increased. This is most possibly due to the fact that there are not sufficient differences between the two images when the angle is small, and the combined error from pixel resolution, manual point selection and image distortion could result in large reduction in the accuracy of the DLT method. Second, the mean error has minimum value when two cameras are separated about 30 to 40 degrees apart, then the image distortion from refraction started to have greater effect on accuracy at 50 degrees.

Base on the result from the first experiment, the next experiment was conducted with one camera set at 30 degrees to the left and another varying from 0 to 50 degrees to the right from the centerline as shown in Figure 3-14 expecting to find a best combination of camera orientation. The image captured in the second experiment are shown in Figure 3-15. By performing DLT between camera 1 and different positions of camera 2, one can calculate the mean error and maximum error as in the first experiment and the results are plotted in Figure 3-16.

Water Tank

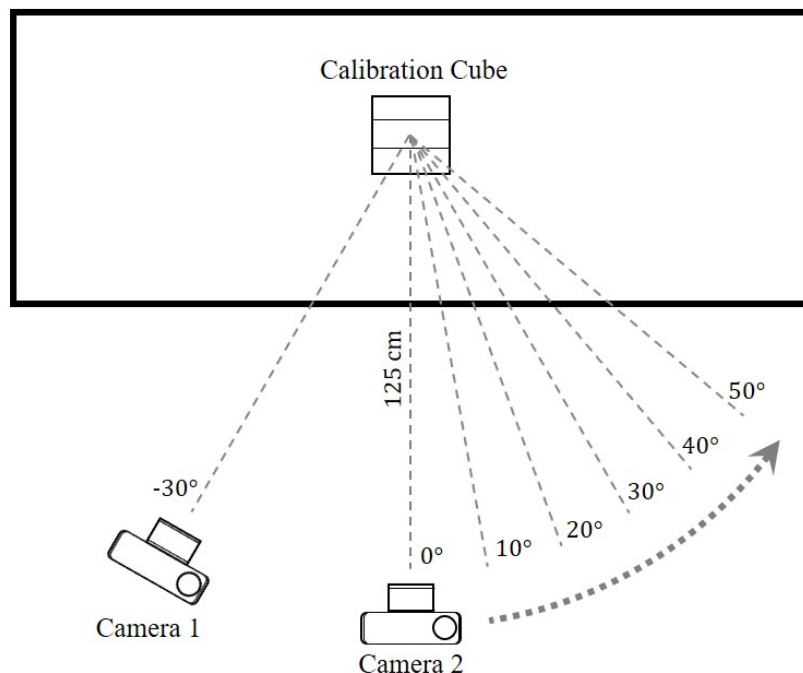


Figure 3-14 Top view illustration of the second refraction experiment

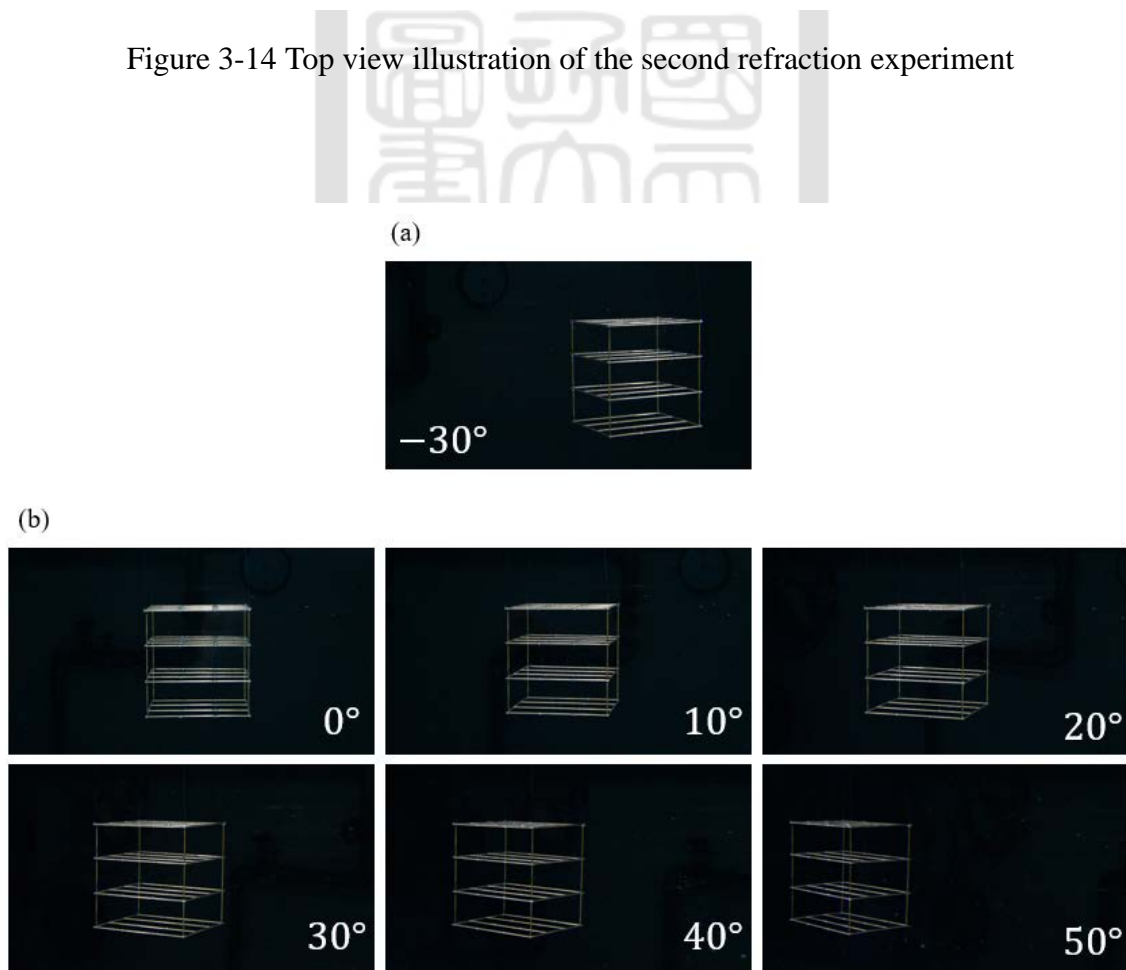


Figure 3-15 Image captured in second refraction experiment (a) camera 1 (b) camera 2

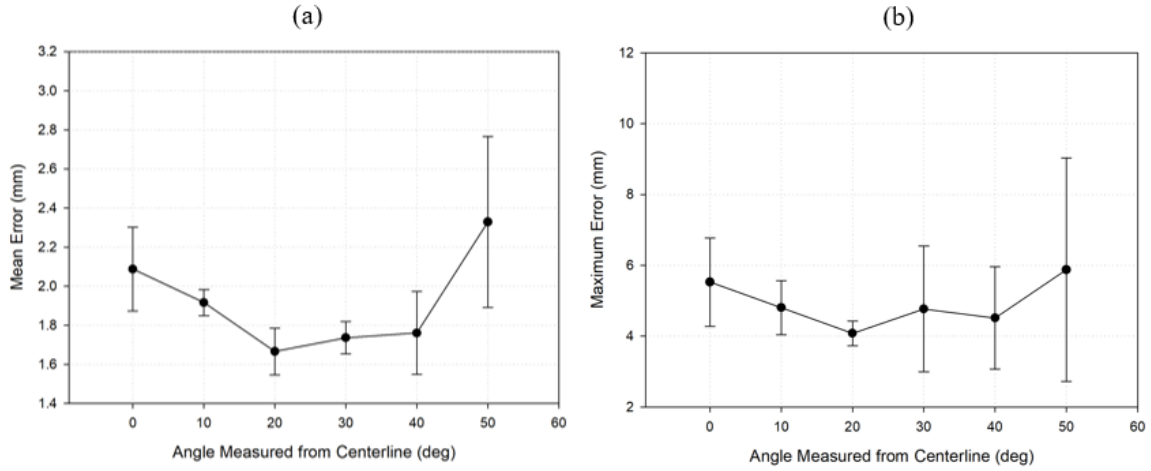


Figure 3-16 (a) Mean error (b) Maximum error of DLT method in second refraction experiment ( $n = 64$  with 4 samples)

According to Figure 3-16, although the maximum positional error of DLT method at different camera angles stayed roughly the same, the mean error still exists minimum value when the camera was set at an angle between 20 to 40 degrees from the centerline and rises again when placed at 50 degrees. From the above two experiments on water tank refraction, we conclude that the accuracy of the DLT method increases as the angle between camera increases, provided that each camera does not exceed 50 degrees measured from the perpendicular position where the distortion due to refraction starts to overwhelm the DLT algorithm. This gives a rough guideline on where the cameras should locate in order to ensure better accuracy for the following experiments on wing kinematics.

### **3.2.4 Feature Point Tracking**

The two proposed wing folding angles along with other kinematic angles were analyzed and compared with the desired results from computer kinematic simulation. A custom MATLAB was written to automatically track the marked feature points in each frame captured by the DSLR cameras. The main structure of the tracking algorithm is shown in Figure 3-17 and details of the algorithm will be introduced in the following paragraph.

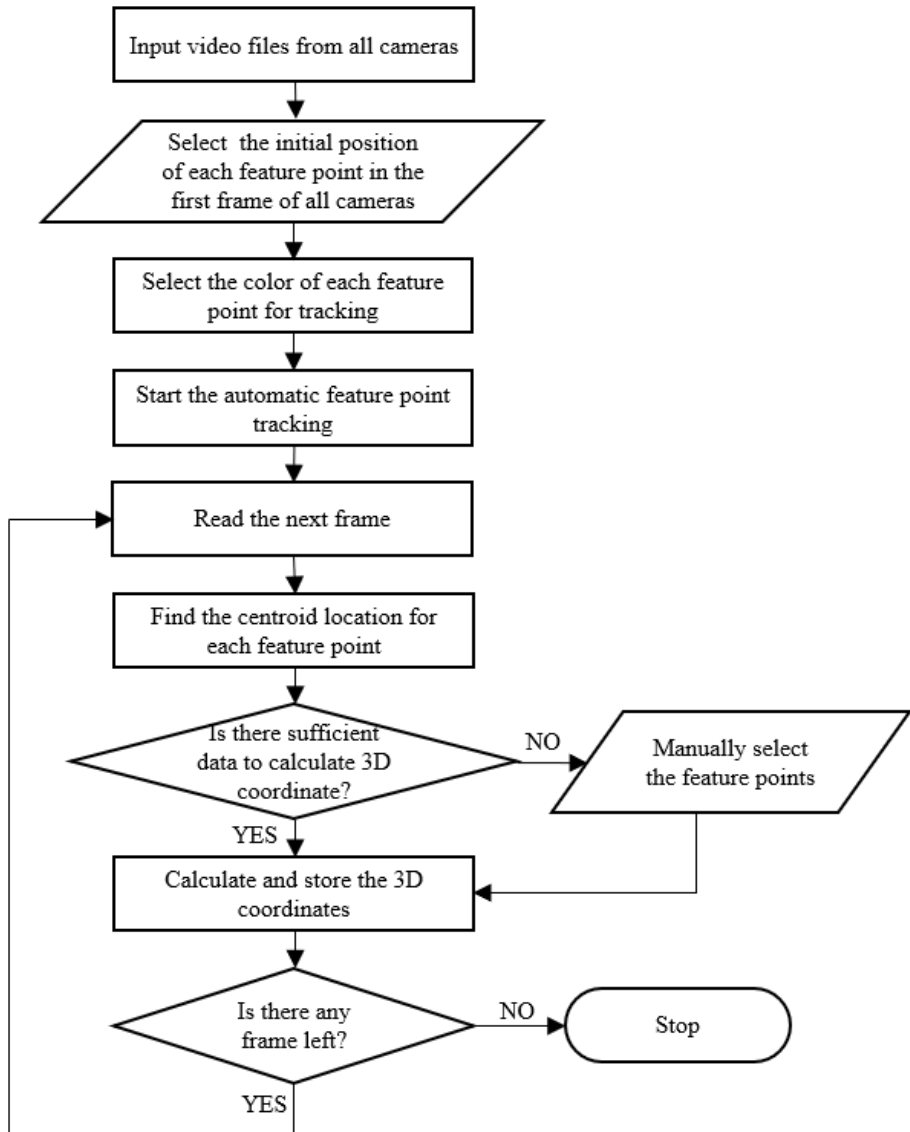


Figure 3-17 Flow chart of the feature point tracking algorithm

The tracking algorithm first transfers the image from the RGB (Red, Green, Blue) color model into the HSV (Hue, Saturation, Value) color model. The user then manually selects the initial positions and color of each feature point. Next, the algorithm identifies the regions where the 3 parameters are within a given range from the initially-selected color for each feature point. In addition, regions that are too small will be rejected in order to prevent false positives or noise. The centroid of the identified region will be calculated and stored for further processing.

After collecting all data of the centroids from each camera, the algorithm checks that there are no following invalid cases which cannot be processed:

1. More than one centroid was found in a single image.
2. No centroid was found in a single image.

By identifying these cases, the algorithm can then determine whether there are still sufficient data, i.e. at least data from 2 cameras were valid, to calculate the 3D coordinates of the feature points. If there is inadequate data, the program will prompt the user with the images asking the user to manually select the unidentified feature point. The videos are then processed frame by frame until the last frame. 3D coordinates of each feature point were calculated using the formula derived in the previous section.

### **3.2.5 Kinematic Verification Results**

For each proposed wing kinematics, 5 flapping cycles were recorded with an average frequency of 0.27 Hz, which matches the requirement for dynamic similarity, and only the 3 cycles excluding the first and last cycle were used for analysis. Camera images of the flapping sequence of experimental case 1, which presents a larger wing folding motion, are shown in Figure 3-18 with normalized time ( $T$ ) interval of 0.1 through a single wingbeat cycle. Figure 3-19 through Figure 3-23 shows the comparison between the desired trajectory from simulation and the actual experimental trajectory averaged between 3 wingbeat cycles. Shaded areas denote the downstroke portion of a wingbeat cycle.



Figure 3-18 Camera images from flapping sequence of experimental case 1

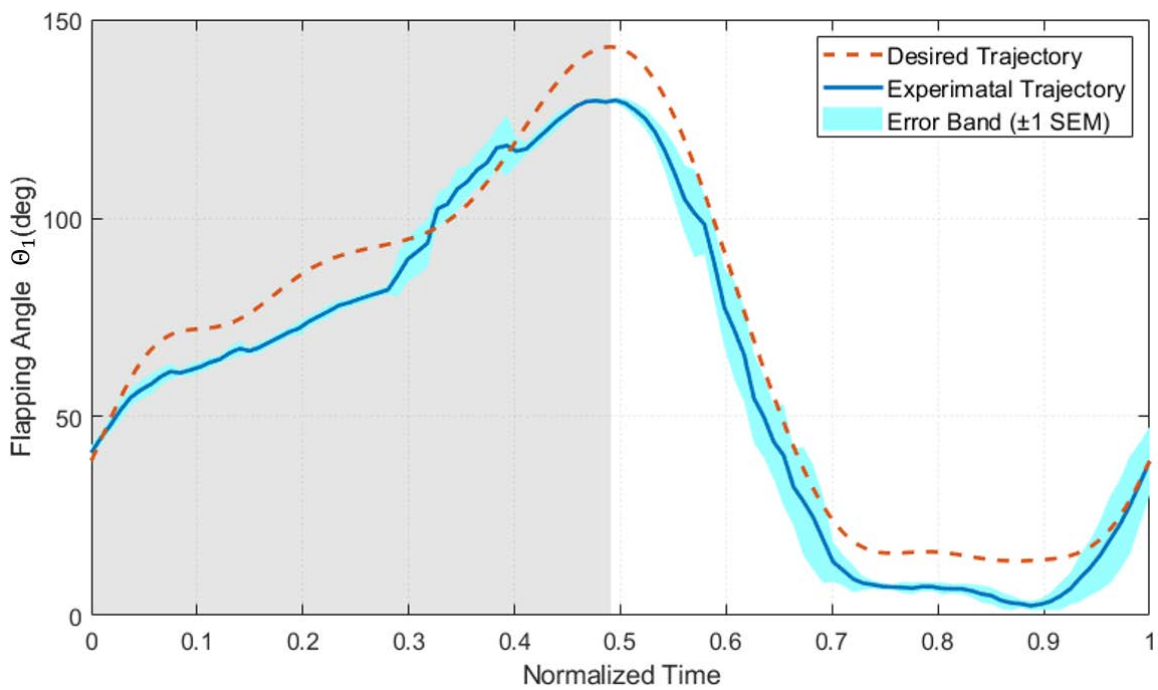


Figure 3-19 Flapping angle of experimental case 1

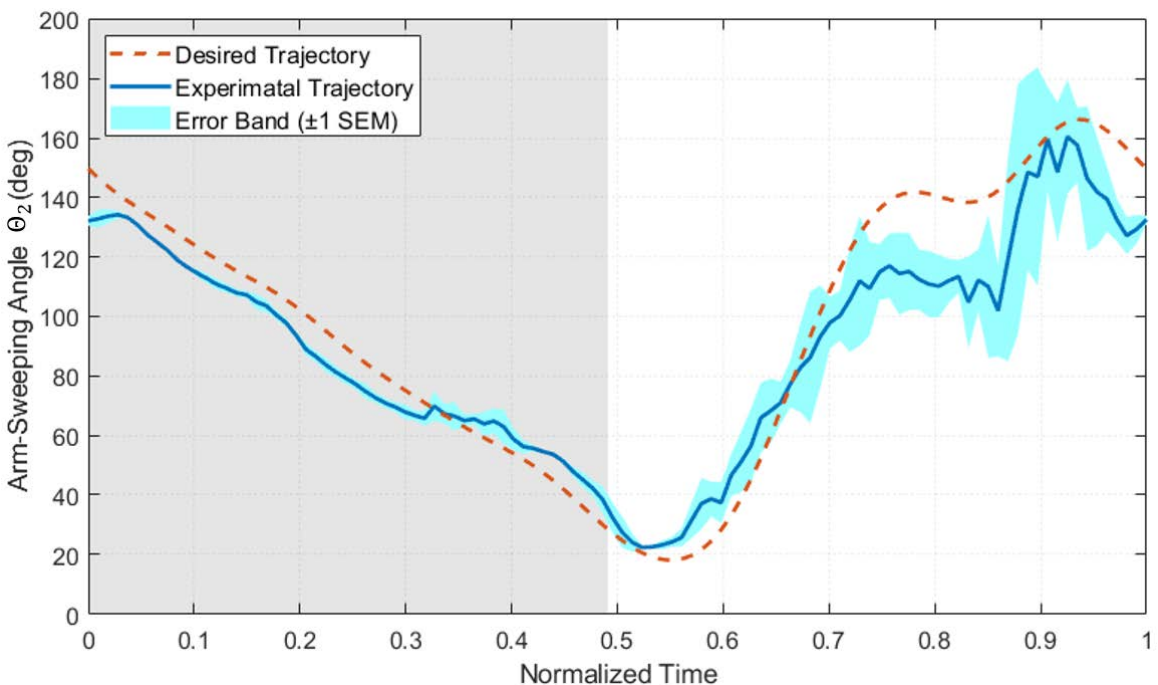


Figure 3-20 Arm-sweeping angle of experimental case 1

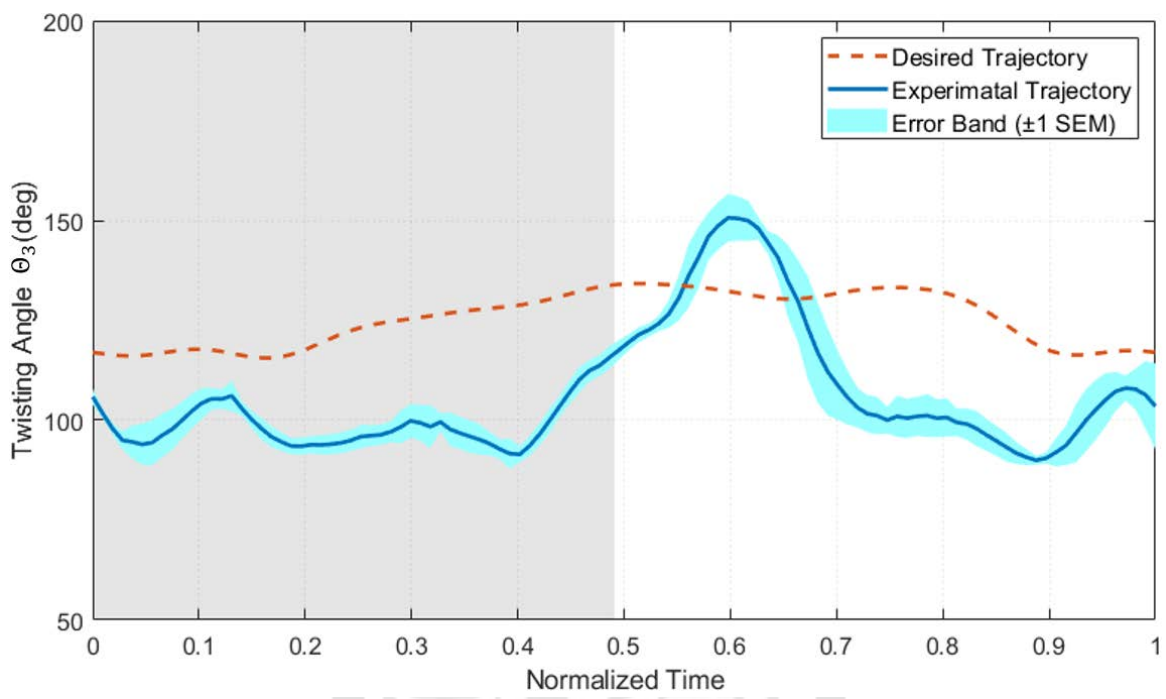


Figure 3-21 Twisting angle of experimental case 1

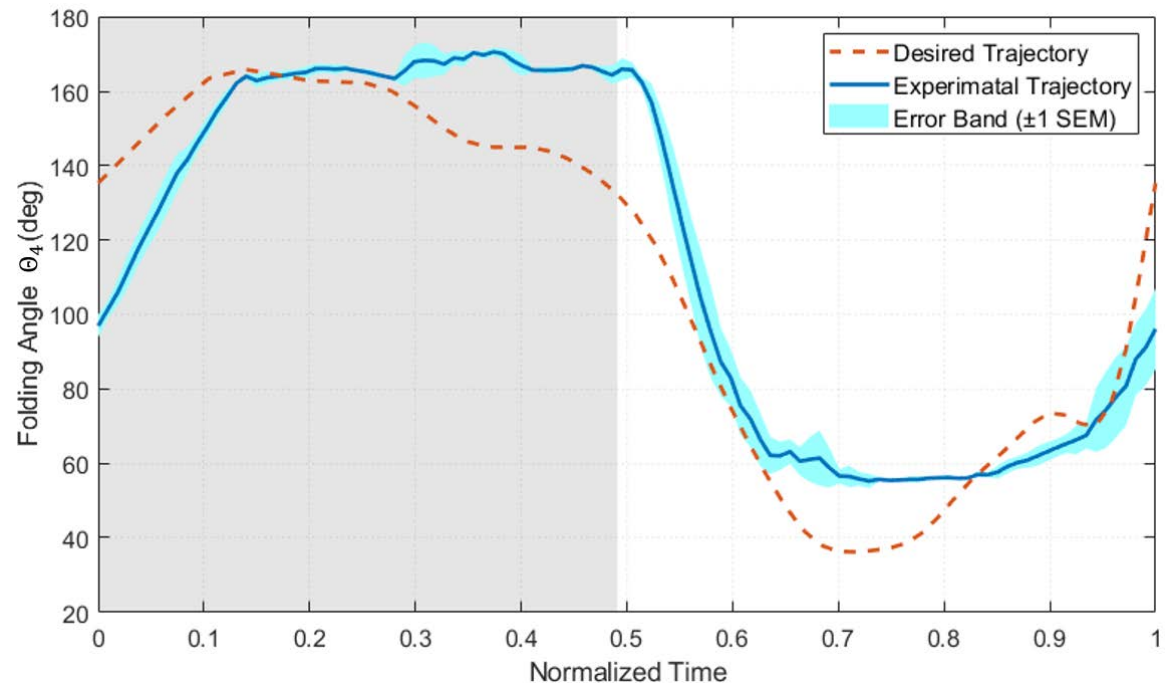


Figure 3-22 Folding angle experimental case 1

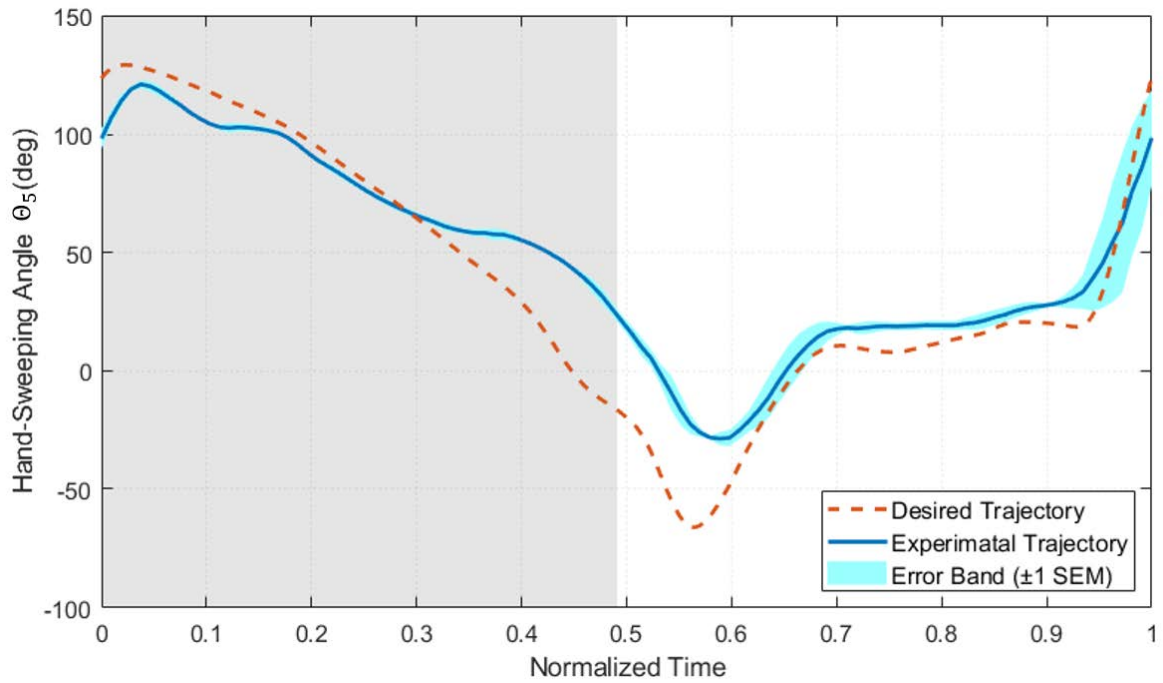


Figure 3-23 Hand-sweeping angle of experimental case 1

From the above data, we can derive the correlation coefficient, mean error and the maximum error between the desired trajectories and the experimental trajectories as shown in Table 3-1. Percentages of the error represents the ratio against the range of each desired trajectory, i.e. the differences between the maximum and minimum angle of each desired trajectory.

Table 3-1 Statistical comparison of experimental case 1

	<b>Flapping Angle</b>	<b>Arm-Sweeping Angle</b>	<b>Twisting Angle</b>	<b>Folding Angle</b>	<b>Hand-Sweeping Angle</b>
Correlation Coefficient	0.9929	0.9805	0.5151	0.9299	0.9701
Mean	$9.53^\circ$	$14.48^\circ$	$23.48^\circ$	$18.57^\circ$	$19.75^\circ$
Error	(7.35%)	(9.78%)	(126.15%)	(14.32%)	(10.12%)
Maximum	$14.80^\circ$	$40.53^\circ$	$37.45^\circ$	$39.24^\circ$	$25.47^\circ$
Error	(11.42%)	(27.37%)	(201.23%)	(30.25%)	(13.05%)

According to Table 3-1, all kinematic angles except the twisting angle, which will be addressed later, were able to achieve correlation coefficients of over 0.9 and only around 10% of mean errors. This not only shows that the designed mechanism is able to perform the desired kinematic motions but also confirms that the derived kinematic transformation between the reference kinematic angles ( $\Theta$ ) and the motor angles ( $\Psi$ ) is correct. After inspection, we determined that these errors are mostly due to causes such as the backlash in the gear system, extension of the stainless-steel cables under tension, gaps between the inner wall of the Teflon tubes and cables, and the deformation of Teflon tubes under load.

On the other hand, twisting angle seems to behave statistically quite differently compared with other angles with only a correlation coefficient of 0.5, over 100% of mean error and over 200% of maximum error. The low correlation coefficient is mainly due to the large peak at  $T = 0.6$  in Figure 3-21, right after stroke reversal. The strong added mass effect caused by the reversing of the wing combined with the rotation axis being at around the 1/4 chord position caused a high pitch-up moment on the wing resulted in a dramatic increase in the twisting angle. Furthermore, the percentage of error was also unusually high. However, when it comes to the actual value of the errors, there isn't much differences compared with others. Not only does the mean error maintained around 20 degrees as some other angles, also, the maximum error isn't as large as others. This is mainly due to the fact that the twisting angle was required to maintain a fairly constant value, with maximum variation of only 18.61 degrees, compared with other angles. As a result, similar amount of error caused by the imperfections in the system result in large percentages of error which may be irrelevant in the scope of determining the robot performance.

Next on, similar as case 1, the camera image sequence of experimental case 2, which has less wing folding motion, is shown in Figure 3-24 and the comparison between the

desired trajectory from simulation and the actual experimental trajectory is shown from Figure 3-25 through Figure 3-29 and Table 3-2.



Figure 3-24 Camera images from flapping sequence of experimental case 2

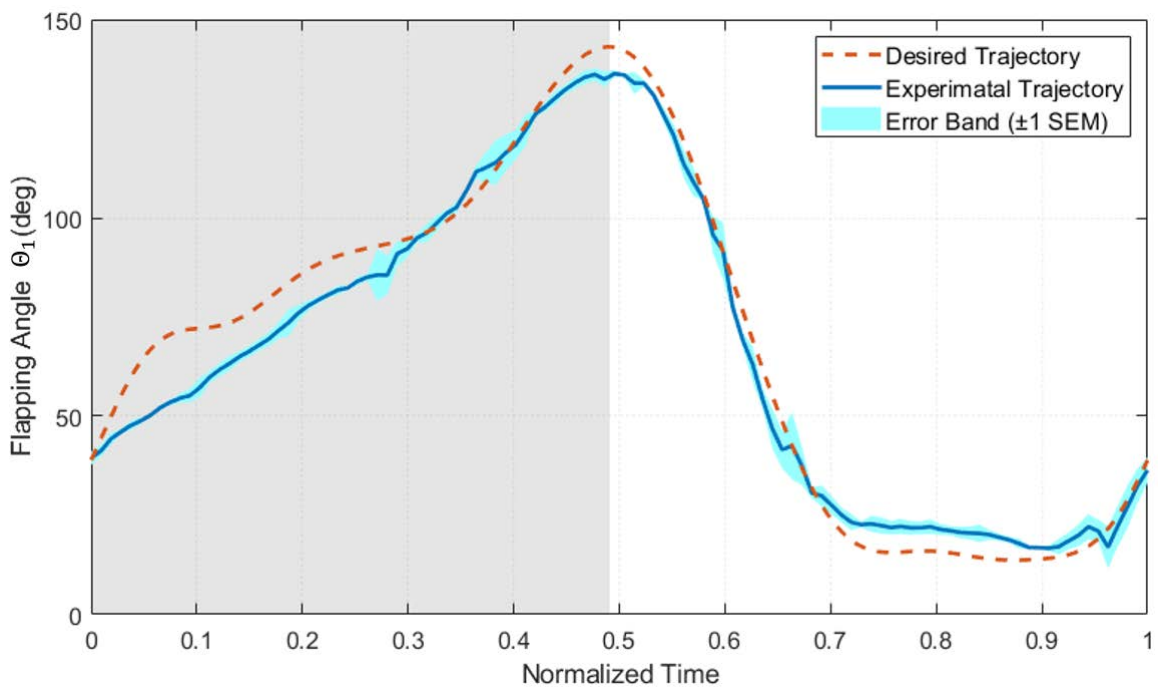


Figure 3-25 Flapping angle of experimental case 2

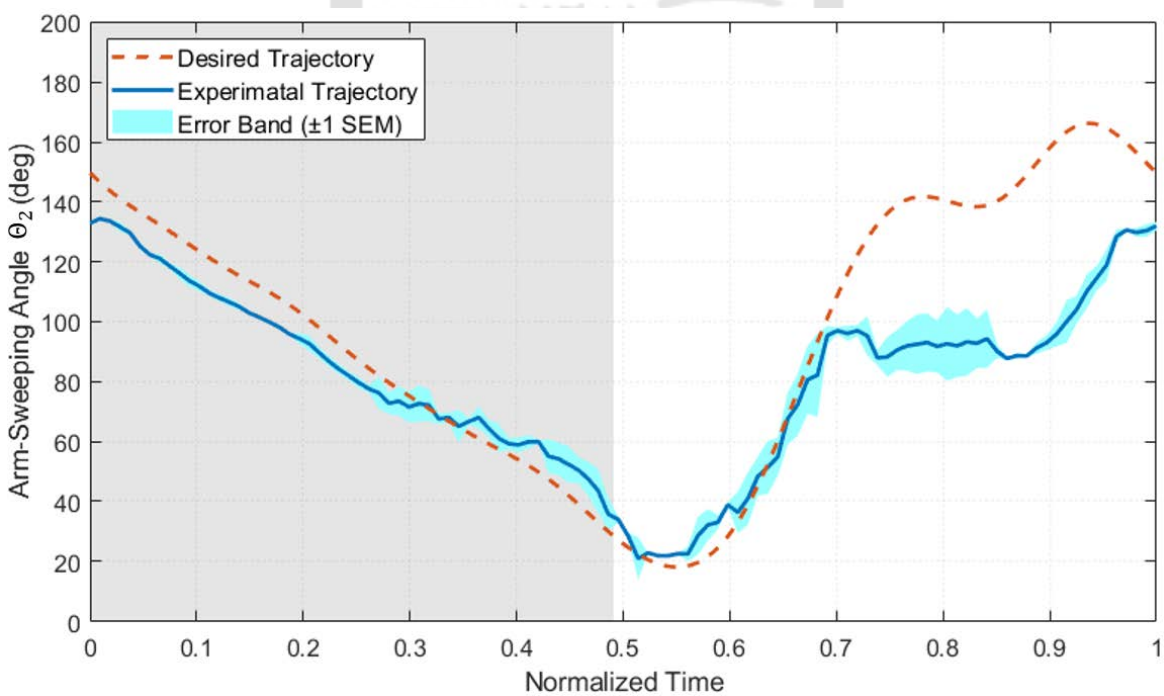


Figure 3-26 Arm-sweeping angle of experimental case 2

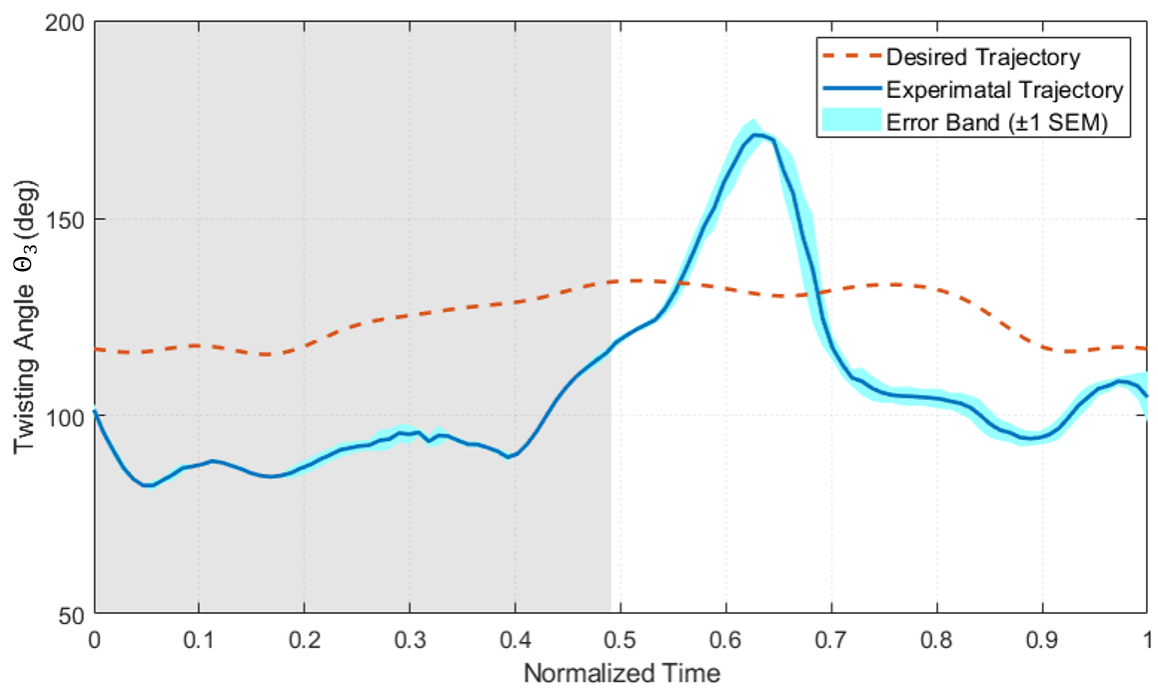


Figure 3-27 Twisting angle of experimental case 2

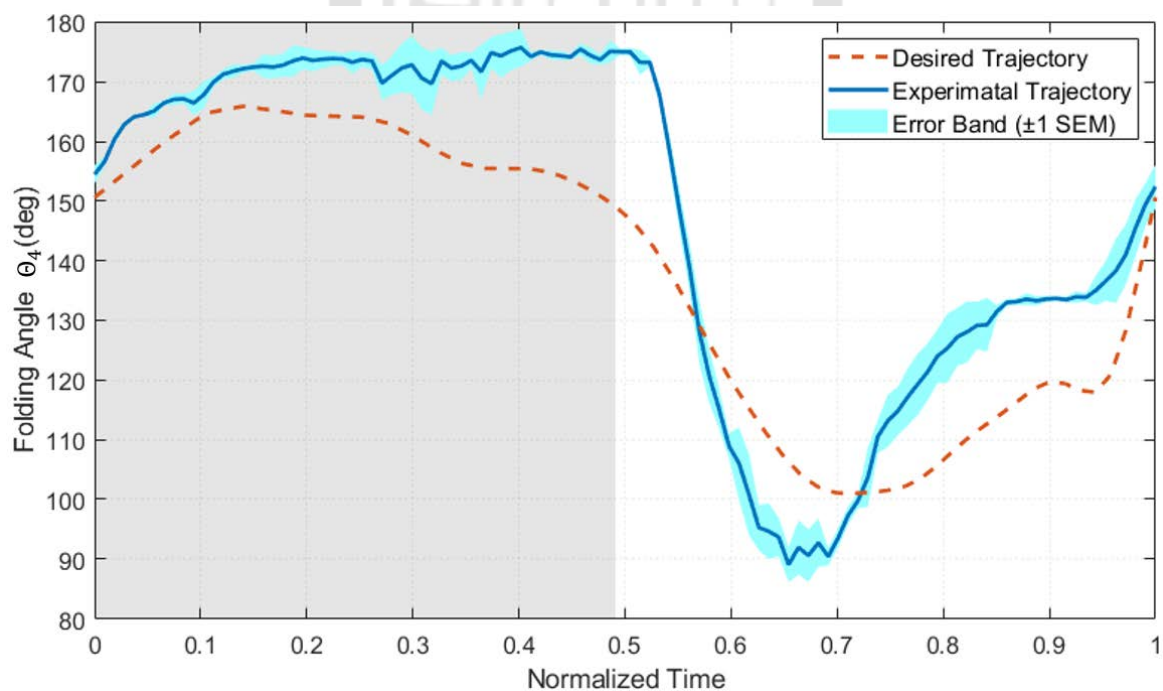


Figure 3-28 Folding angle of experimental case 2

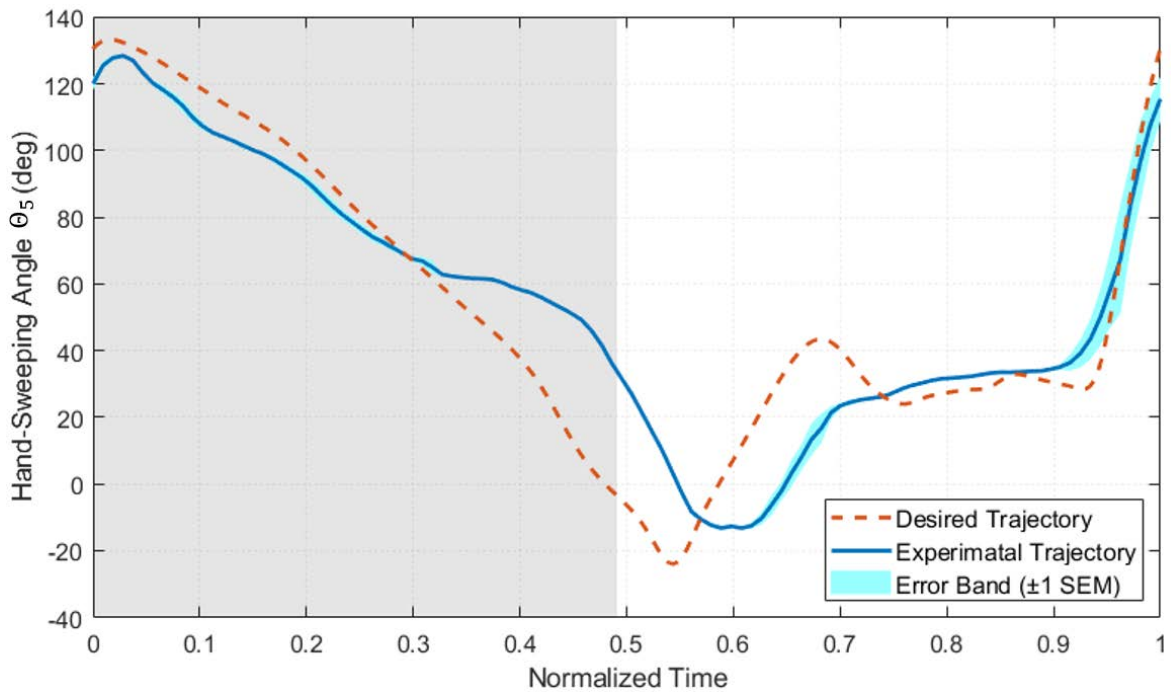


Figure 3-29 Hand-sweeping angle of experimental case 2

Table 3-2 Statistical comparison of experimental case 2

	Flapping Angle	Arm-Sweeping Angle	Twisting Angle	Folding Angle	Hand-Sweeping Angle
Correlation Coefficient	0.9897	0.9143	0.6042	0.9311	0.9174
Mean	7.12°	26.82°	26.78°	14.47°	17.52°
Error	(5.50%)	(18.11%)	(143.91%)	(22.32%)	(11.15%)
Maximum	17.14°	64.56°	39.00°	17.58°	34.23°
Error	(13.23%)	(43.59%)	(209.56%)	(27.11%)	(21.78%)

For experimental case 2, most kinematic angles show similar trends with that of case 1 when compared against the desired trajectories according to Table 3-2. However, one thing to be noticed is that the arm-sweeping angle existed a slightly lower correlation coefficient and larger errors. From Figure 3-26, the most significant issue was that the arm-sweeping angle was unable to reach the desired angle during upstroke. This was possibly due to the

smaller folding angle causing the wing to rapidly unfold during upstroke which results in higher aerodynamic loads on the wing that resists the aft-sweeping motion of the entire wing. On the other hand, the hand-sweeping angle did not suffer from large errors as much as the arm-sweeping angle despite the similar correlation coefficient. This was due to the combined effect of arm-sweeping and folding motion. Although the arm-sweeping was lagging behind the desired trajectory during upstroke, the wing unfolded so rapidly such that the folding angle was leading ahead of the desired position. This resulted in nearly perfect tracking of the desired trajectory from  $T = 0.7$  to  $T = 1.0$  in Figure 3-29.

To sum up, there are several key points that we can infer from the kinematic verification results of experimental case 1 and case 2. First of all, the derived kinematic transformation seems to be correct due to the fact that nearly all kinematic angles had high correlation coefficients with the desired simulation result. Second, errors between the desired and actual trajectories were mainly due to the imperfections in the robot system such as backlashes, deformations and gaps. Third, the reducing in folding amplitude caused unfavorable forces acting on the wing during upstrokes which could be further investigated through force measurements and flow visualization in the next chapter. Last but not least, reducing the imperfections in the robot system, especially the error in twisting, is necessary in the future design of this robot since it may lead to substantially different aerodynamic results.

# **CHAPTER IV**

## **Force Measurement and Flow Visualization**

This chapter focus on the force measurement and flow visualization experiments done with the flapping-wing robot, detailing the experimental setups and results from the experiments.

### **4.1 Force Measurement System**

#### **4.1.1 Construction of the Force Measurement System**

In the present research, lift generated by the robot is the only force component that we are interested in. Hence, a 1-component force balance assembled with load cells was implemented to measure the vertical force. However, several issues have to be considered while constructing the force balance. One is that the robot was submerged in water. Since a waterproof force balance was not available, the force measurement process had to be done above the water. Second is that the joints on the wing were actuated through pulleys by motors mounted in the control box. In order to correctly measure the aerodynamic forces, the force balance cannot be mounted directly between the fixed base and the supporting rod of the robot as shown in Figure 4-1A, which results in the actuating forces being an external force that will be measured with the force balance. Instead, a method of combining 4 load cells supporting each corner of the control box, illustrated in Figure 4-1B, was selected since it includes the entire control box into the measured system making the actuating forces internal that will not be measured. Despite the benefits, this configuration not only increased the number of load cells required but also the maximum allowable load of the combined load

cells needed since the total assembly of the control box involves 10 stepper motors, power supply and other electronics, which is significantly heavier than the robot wing alone.

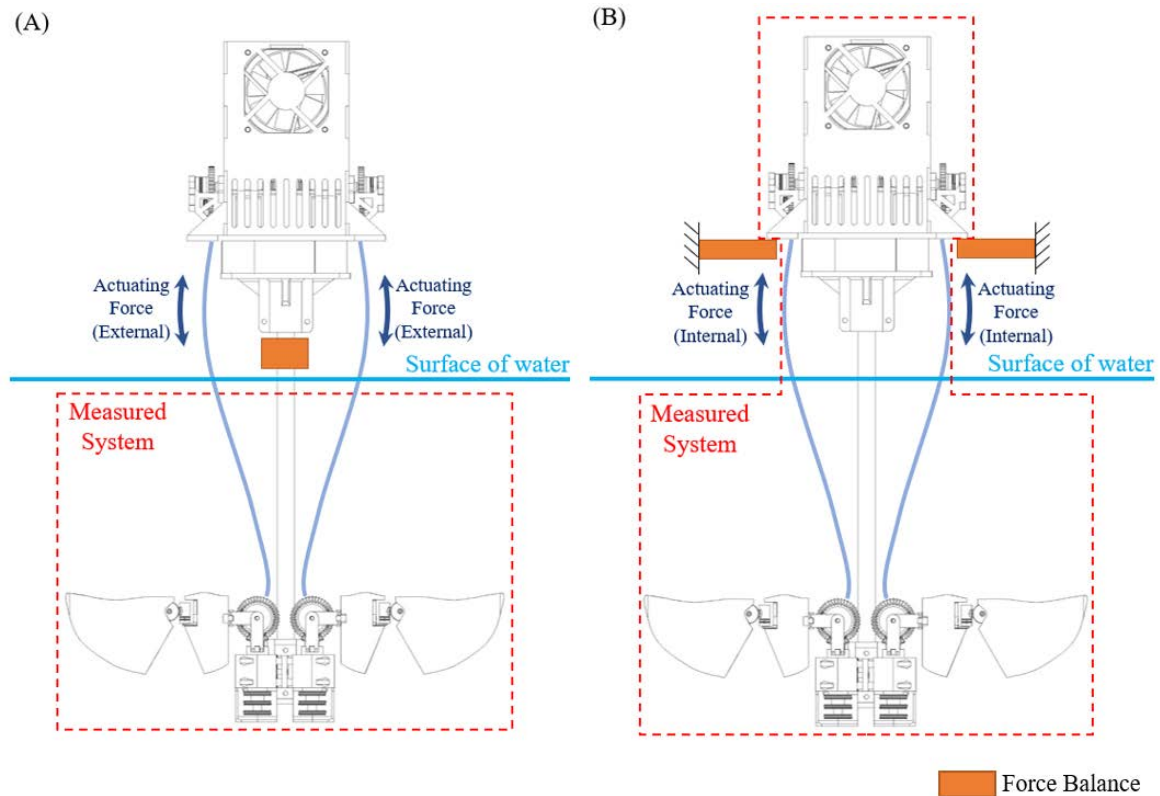


Figure 4-1 Configurations of force balance

The system layout of the force measurement system is shown in Figure 4-2 marking all components. The force balance was constructed using 4 2-kg cantilever type load cells forming bridges between the fixed frame and the robot assembly. The signal wire of each load cell then goes through a load combinator, merging all signals into a single output which is then processed by the HX711 load cell amplifier chip. The HX711 chip is a 24-bit analog-to-digital convertor with an on-chip amplifier which has a selectable gain of 32, 64 and 128. Furthermore, it provides a selectable sampling rate of 10 Hz and 80 Hz with simultaneous 50 Hz and 60 Hz power supply rejection ratio of 100 dB to reduce noise. For the purpose of this research, the amplifier gain and sampling rate are set to 128 and 80 Hz.

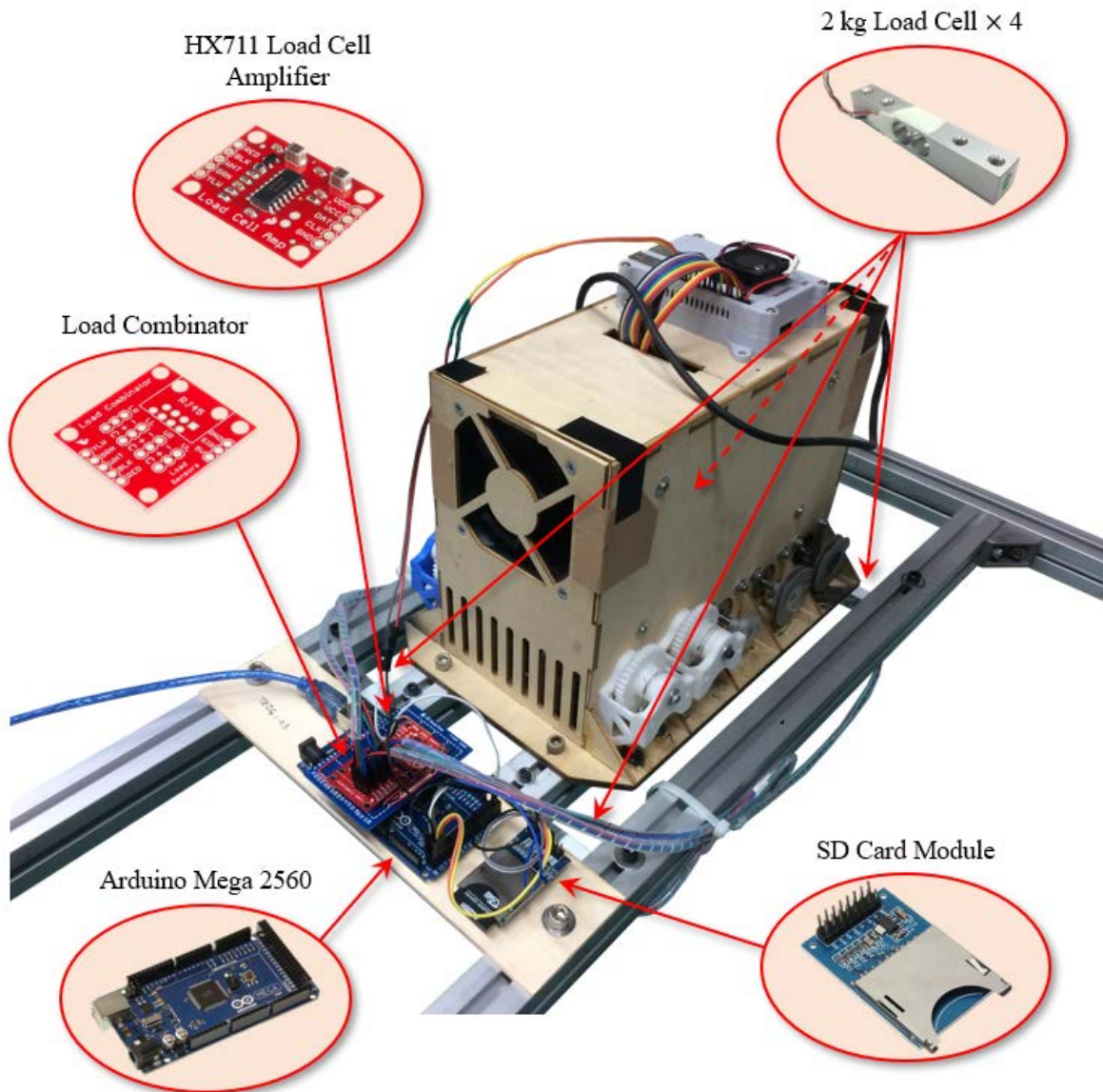


Figure 4-2 System layout of the force measurement system

A data collection system was written and programmed onto an Arduino Mega 2560 microcontroller board which the HX711 load cell amplifier communicates through a custom serial protocol. The data collection system provides a simple user interface through the Arduino serial monitor which allows the user to perform tasks such as taring, calibration and data recording. In addition, an SD card module was attached to the Arduino to record the collected dataset which includes the timestamp in milliseconds, force measurement in grams and also the triggering signal from the raspberry pi that controls the robot.

#### **4.1.2 Uncertainty and Calibration of the Force Measurement System**

Although the HX711 amplifier has a built-in function of noise rejection, calibration and noise filtering is still necessary in order to obtain reliable data. Furthermore, these general-purposed low-cost load cell amplifiers are also highly prone to sensor drift, meaning that the readings from could constantly drift away from the correct value as time goes on. Therefore, this should also be considered during the calibration process.

To understand the characteristics of the force measurement system, force measurements were recorded for 5 minutes without any external forces or disturbances. As plotted in Figure 4-3, the drifting phenomenon was clearly observed along with some noise in the data. The drifting appeared to be quite linear within the 5-minute observation window which highly matches the linear regression line. Thus, as long as the experiment is conducted within the 5-minute window, we should be able to compensate the drifting effect during data analysis using the linear regression results.

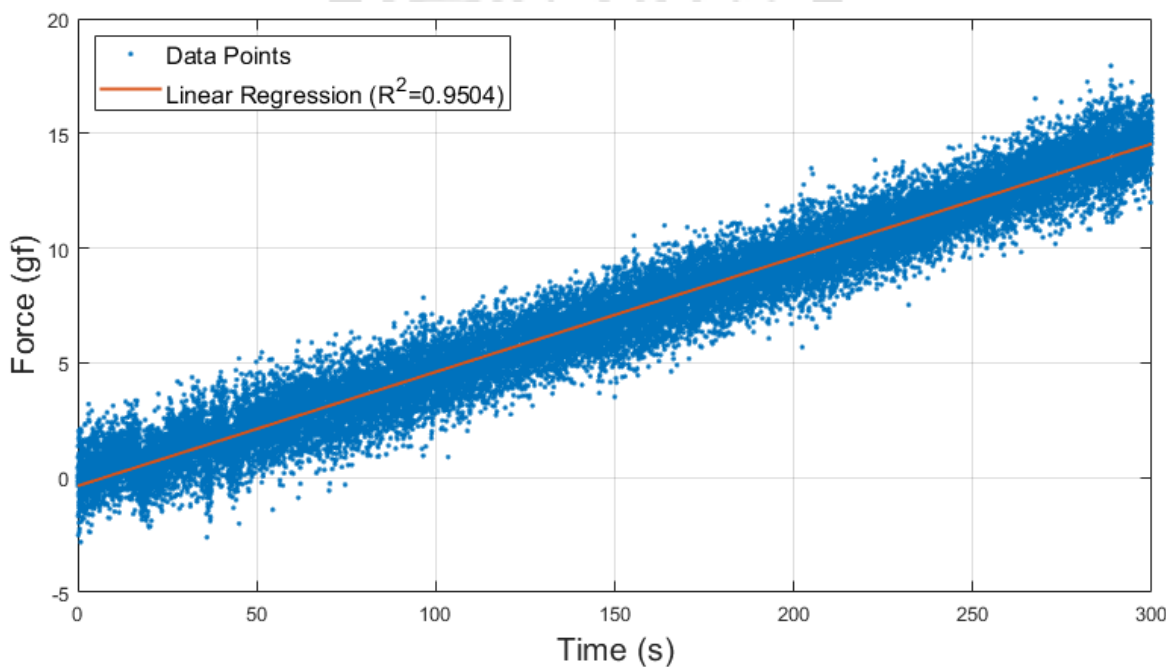


Figure 4-3 Drift assessment of the force measurement system

In addition, fast Fourier transform (FFT) was done to further analyze the noise component in the sensor readings. From the frequency spectrum shown in Figure 4-4, there were only a few noise components with insignificant amplitudes observed. These components could have resulted from sources such as the vibration of the cooling fan in the control box or other ambient electromagnetic interferences. However, this means that the fluctuation in Figure 4-3 had to be the inherent randomness of the HX711 chip. This can also

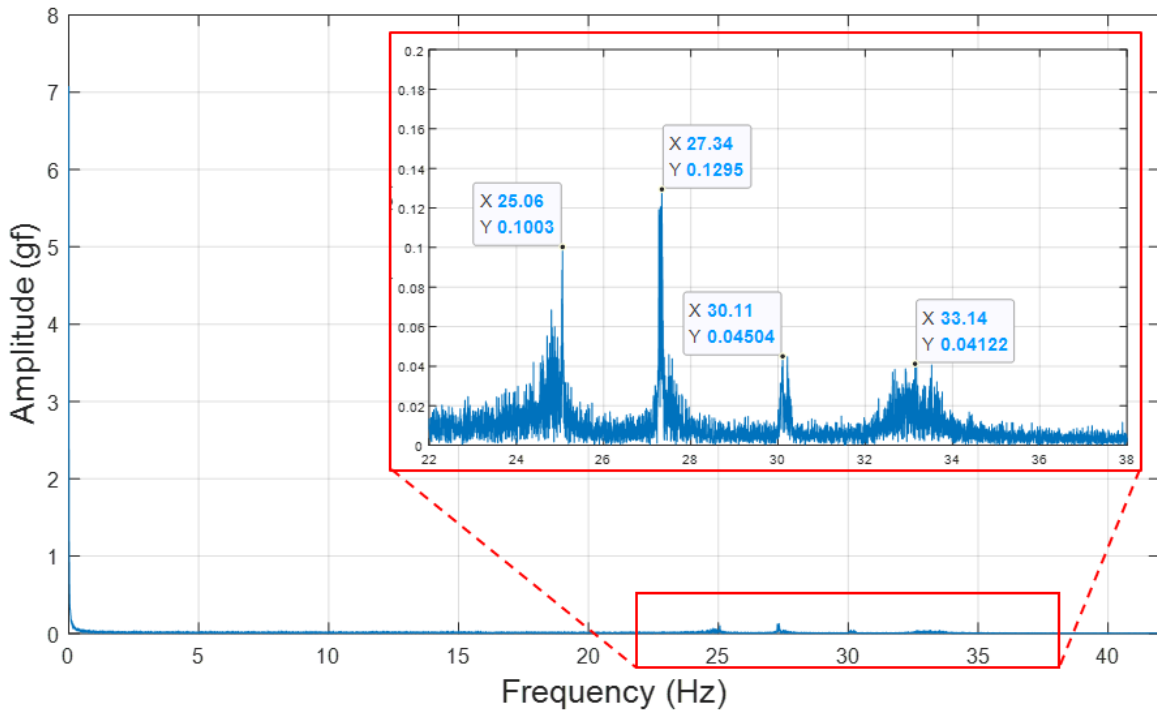


Figure 4-4 Frequency spectrum of measured force data

be verified by the histogram of the linearly compensated data shown in Figure 4-5 which forms a bell-shaped Gaussian distribution. The standard deviation of the corrected data was 0.9767 which means that it is expected to be errors within  $\pm 1.9143$  g in the measured data under a confidence level of 95% during all measurement by this system.

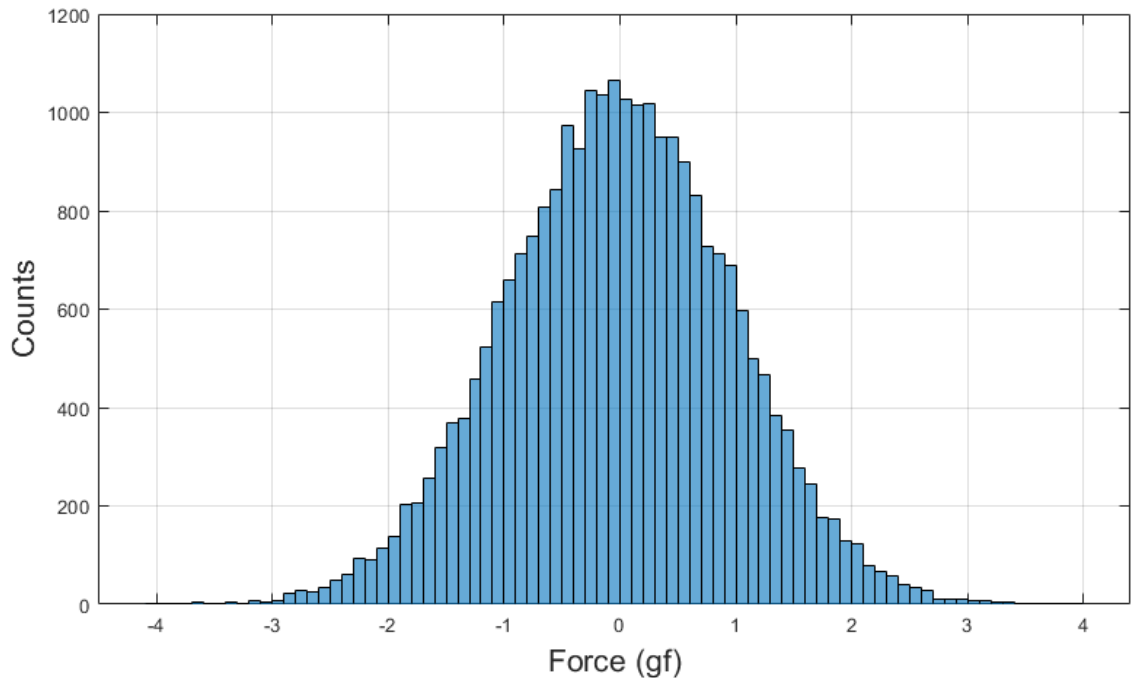


Figure 4-5 Distribution of linearly compensated force data

The linearity of the force balance was also checked using known weights. From Figure 4-6, it is clear that the system performed exactly linearly as expected within the range tested with only minor correction required.

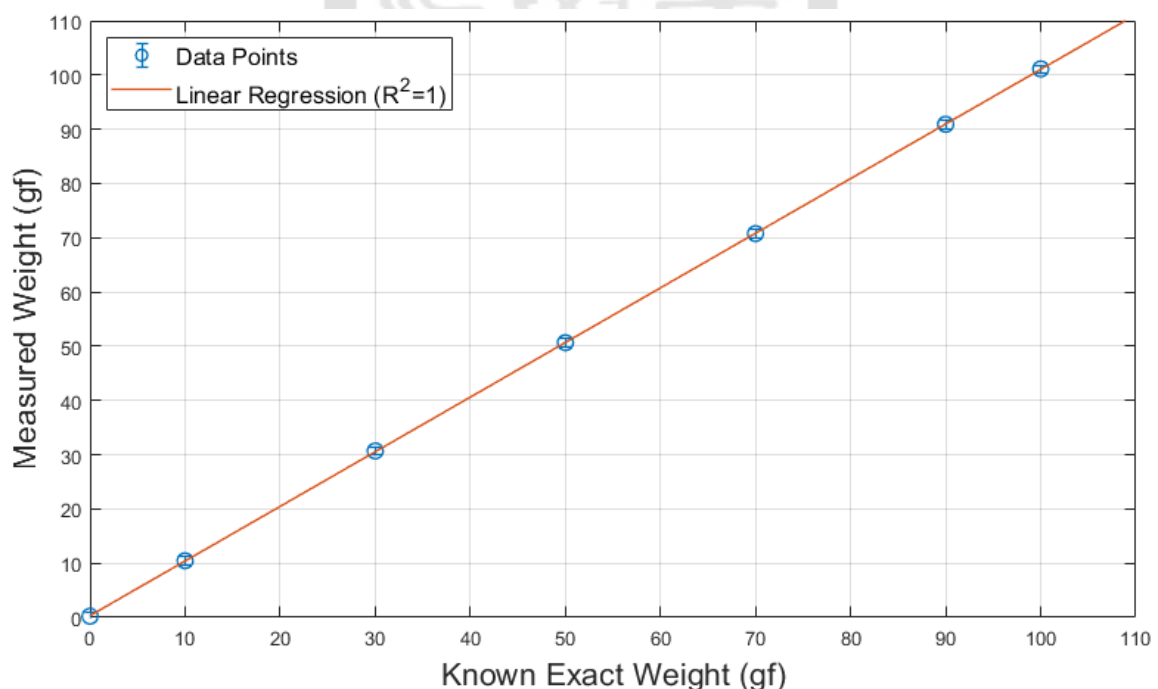


Figure 4-6 Linearity calibration results of the force measurement system

## **4.2 Flow Visualization System**

### **4.2.1 High-speed Camera**

The high-speed camera used in the present research a Photron Fastcam SA-X camera (Figure 4-7). The CMOS on the camera has a maximum resolution of  $1,024 \times 1,024$  pixels with 12-bit ADC. It is capable of capturing images at up to 12,500 frames per second under maximum resolution. The onboard memory is 16 GB which can store 10,916 frames at maximum resolution. The user can control the camera and also preview the images through computers with the Photron Fastcam Viewer software. The camera can also be triggered by an external triggering switch or TTL signals. During this research, the frame rate is set to 500 frames per second, which allows continuous recording up to 21.83 seconds.

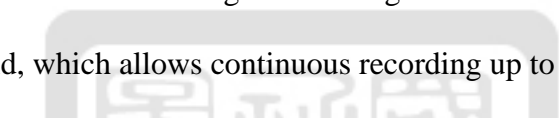


Figure 4-7 Photron Fastcam SA-X highspeed camera

### **4.2.2 Laser and Optics**

The laser source used in this research is the HPG-5000 solid state laser from Elforlight (Figure 4-8). It is a continuous wave (CW) laser with a maximum output power of 5 watts and the wave length of the laser beam is 532 nm. The output laser beam has a maximum diameter of 2 mm and is then passed directly through an adaptor with a cylindrical lens to form a uniform light sheet.



Figure 4-8 Elforlight HPG-5000 laser with power supply

#### **4.2.3 Experimental Setup**

In order to more thoroughly examine the flow field around the robot, PIV experiments on multiple parasagittal planes have to be conducted. This means that the position of the laser light sheet has to be easily adjusted. Therefore, the equipment is setup as illustrated in Figure 4-9. The laser head is mounted on to an optical flat which sits on a pair of guided rails which allows manual adjustments of the horizontal position. The highspeed camera, which will be triggered by the control board on the robot, is positioned on the other side, perpendicular to the light sheet.

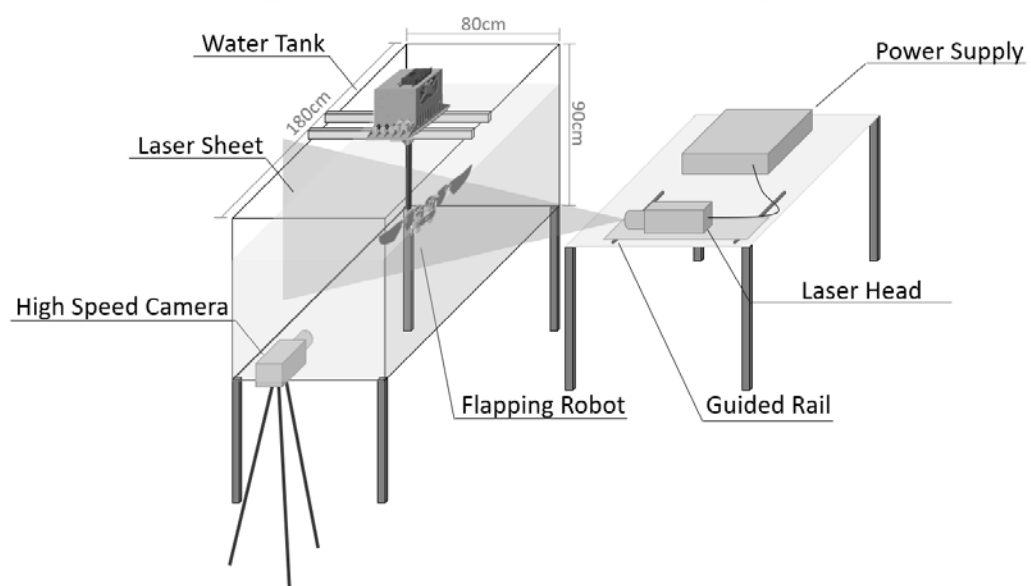


Figure 4-9 Experimental setup for PIV flow visualization experiment

#### **4.2.4 Image Processing Tool**

The PIV image processing was done using an open source software – PIVlab, which was written in MATLAB by Dr. Thielicke[42]. PIVlab provides a simple and user-friendly graphical user interface which implemented several different tools and algorithms for image pre-processing, PIV analysis and data post-processing. During analysis, each image was divided into multiple small interrogation windows and the velocity is determined by the cross correlation between two successive images pairs using fast Fourier transform. The program was set to perform 3 passes with the first pass using a  $128 \times 128$  pixel interrogation window for rough calculation, and then followed by two passes with  $64 \times 64$  pixel and  $32 \times 32$  pixel to provide finer resolution of the flow field.

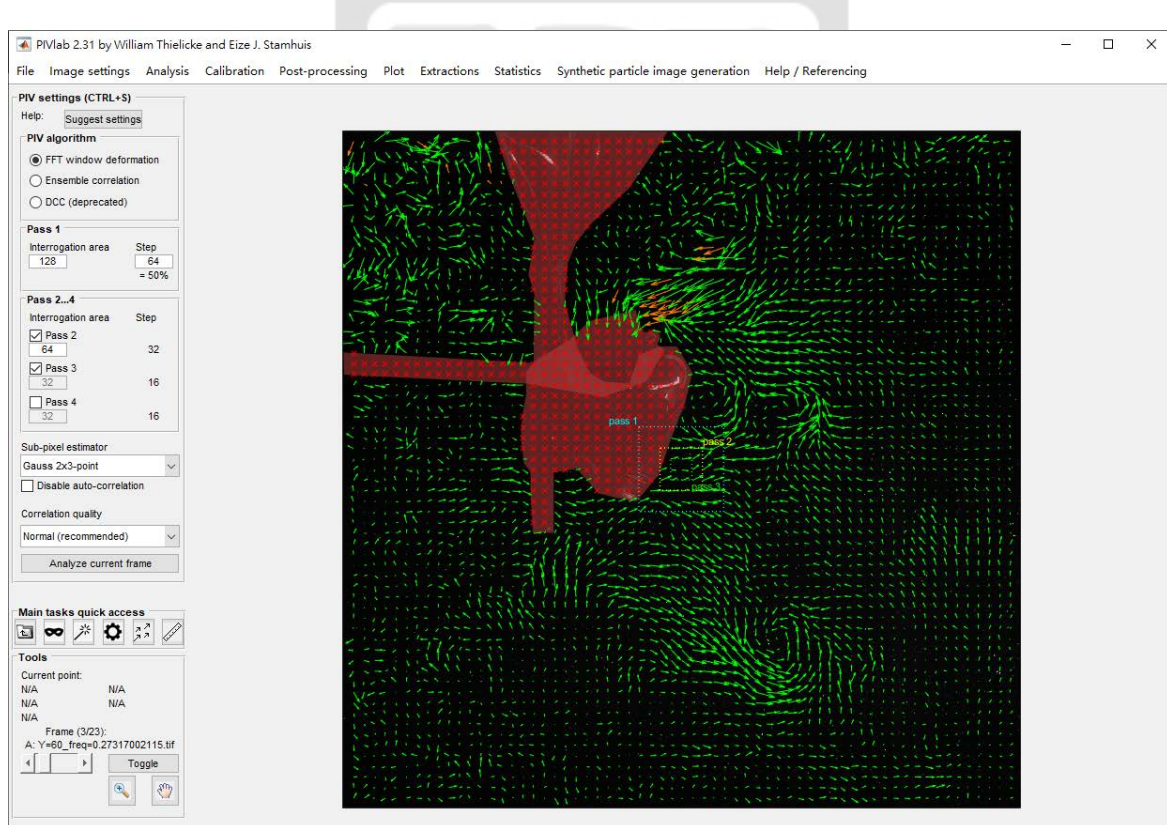


Figure 4-10 Graphical user interface of PIVlab

## **4.3 Results and Discussion**

### **4.3.1 Force Measurement and Wingbeat Phase Characterization**

To ensure valid force data, measurements for each experimental case are all conducted in 3 phases. The first phase is the drift estimation phase where we monitor the drift characteristics for 2 minutes in order to compensate the drift. The Second phase is the measurement verification and calibration phase where we place known weights on the force balance to verify that the compensation is correct and to also make sure that if any correction is needed to ensure valid data. Finally, the last phase is the flapping experiment phase where the robot performs 9 wingbeat cycles and the data from the mid 5 cycles will be averaged and analyzed.

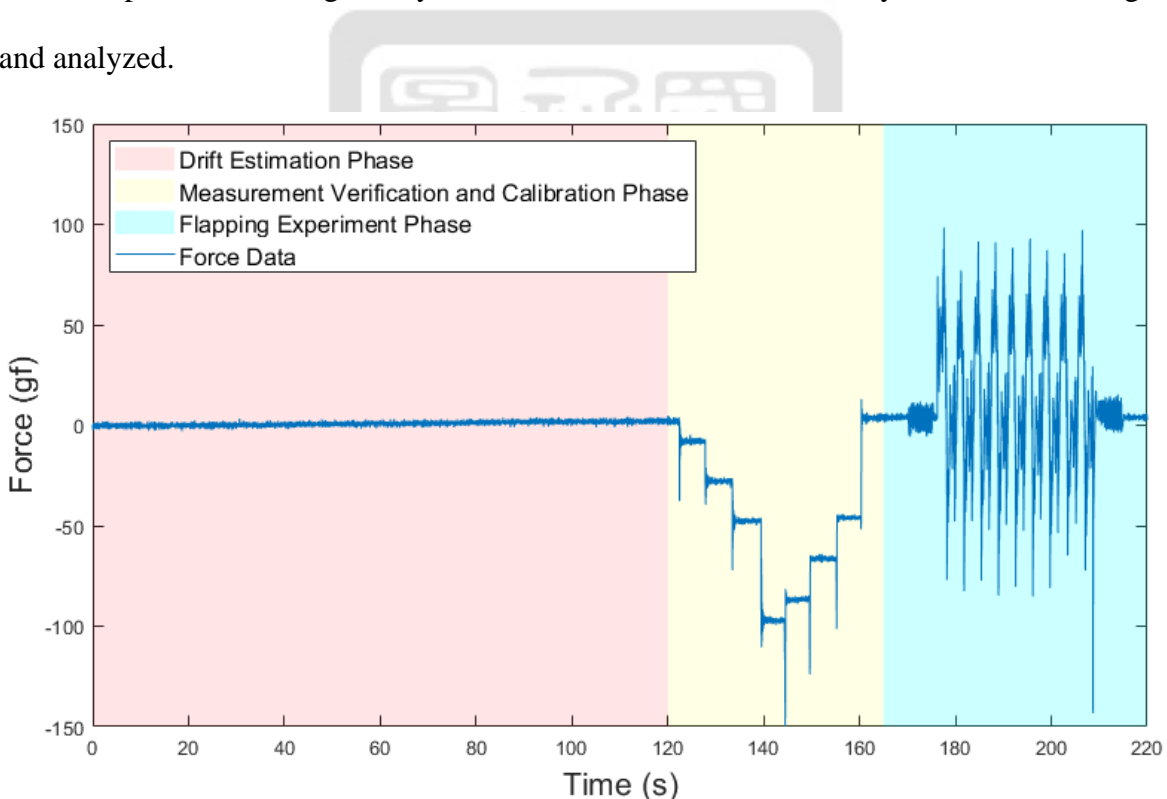


Figure 4-11 Experimental phases of force measurement

The raw lift measurements for each case were processed through a low-pass filter with a cutoff frequency of 10 Hz to eliminate undesirable high-frequency noise in the data. Comparison of the unfiltered and filtered data is shown in Figure 4-12.

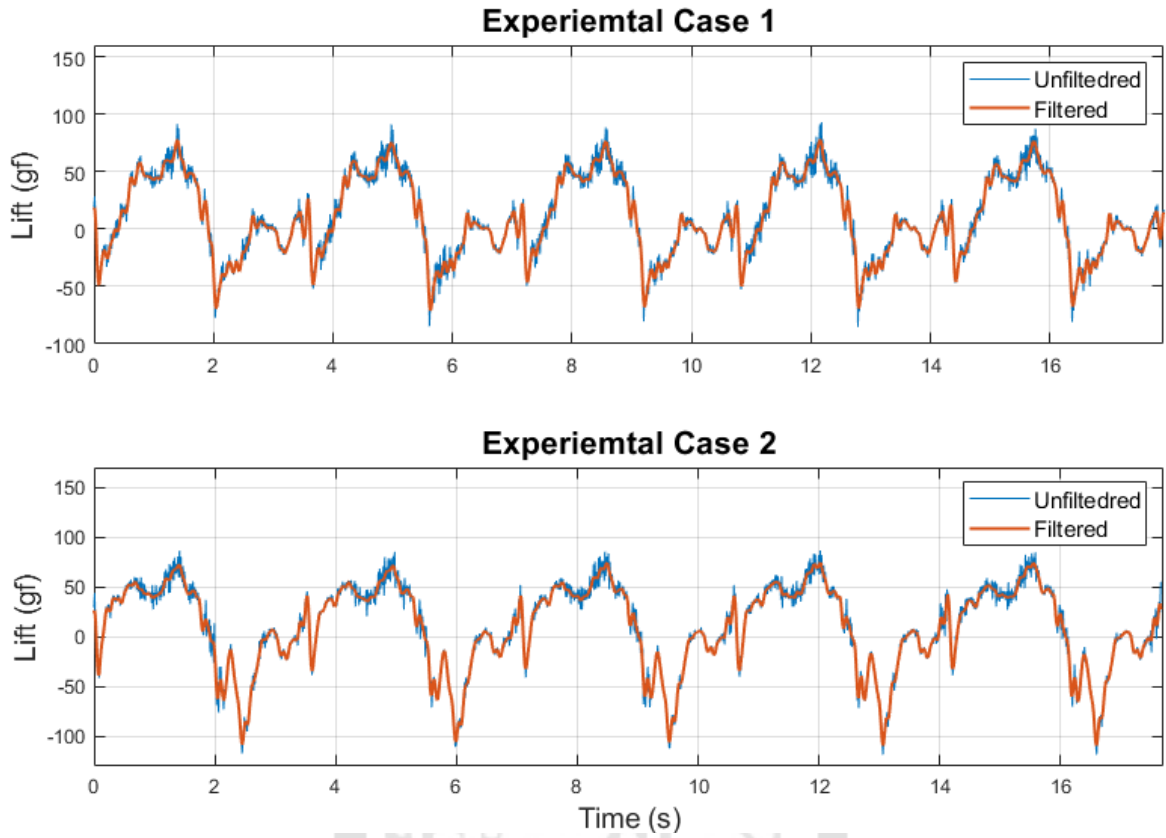


Figure 4-12 Comparison of unfiltered and filtered lift data

Figure 4-13 and Figure 4-14 show the lift production history throughout a wingbeat cycle which were averaged from the filtered data shown in Figure 4-12. Shaded areas in the figures depicts the downstroke portion of a wingbeat cycle. In addition, the time-averaged lift force of each case is calculated by

$$L_{avg} = \frac{\sum L_n \times \Delta t}{T_{cycle}} \quad (4-1)$$

where  $L_n$  is the lift force of each data point,  $\Delta t$  is the sampling time and  $T_{cycle}$  is the period of a wingbeat. Therefore, we can get

$$L_{avg,case1} = 6.1377 \text{ gf}$$

$$L_{avg,case2} = 7.3491 \text{ gf}$$

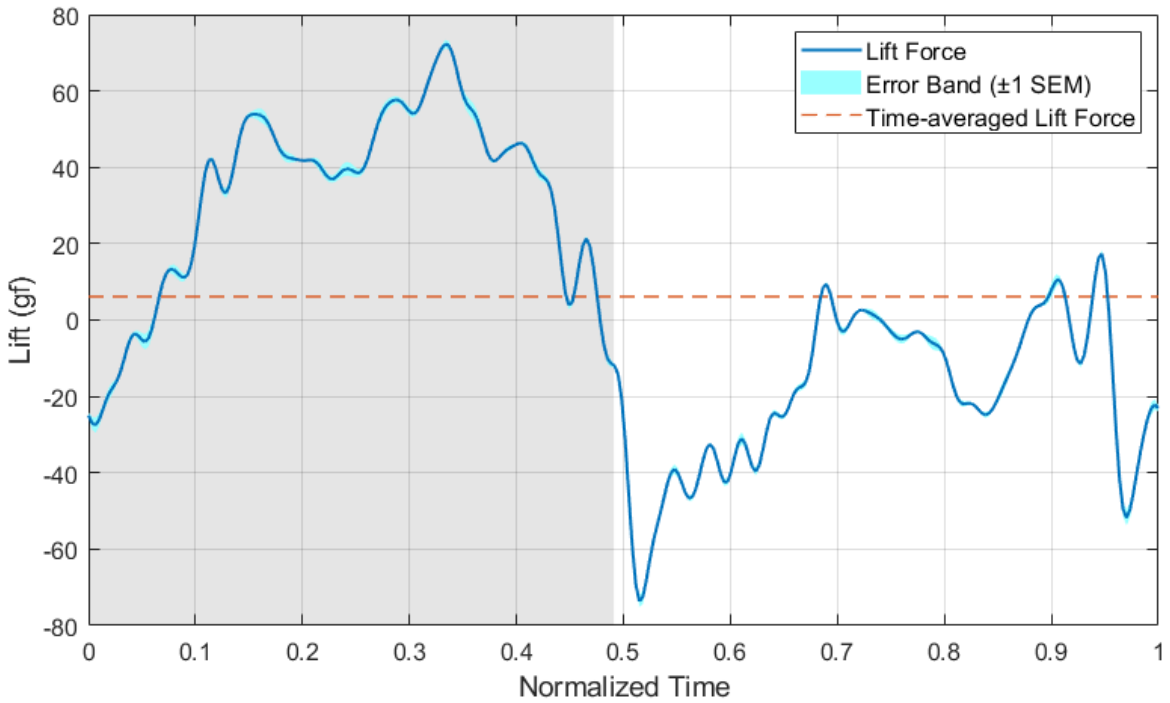


Figure 4-13 Lift production history of case 1

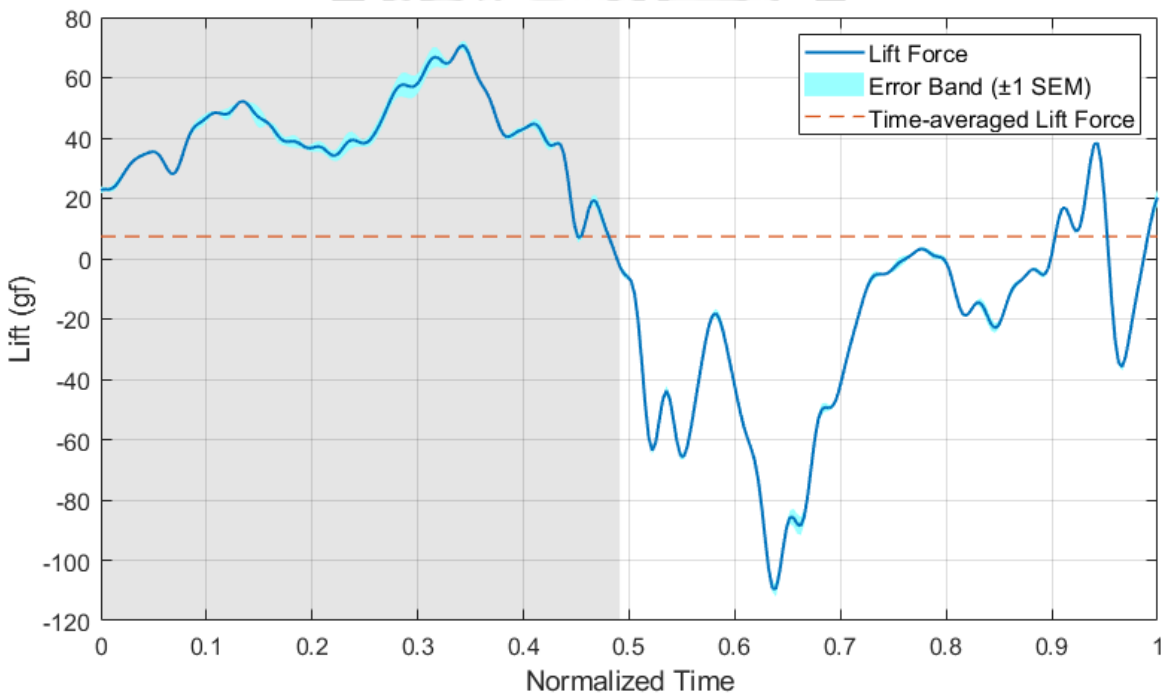


Figure 4-14 Lift production history of case 2

It was surprising that instead of the more passerine-like case 1 motion, the less-folding case 2 came out generating higher average lift. Since the results were out of expectation, the lift production histories of both cases are compared simultaneously in Figure 4-15.

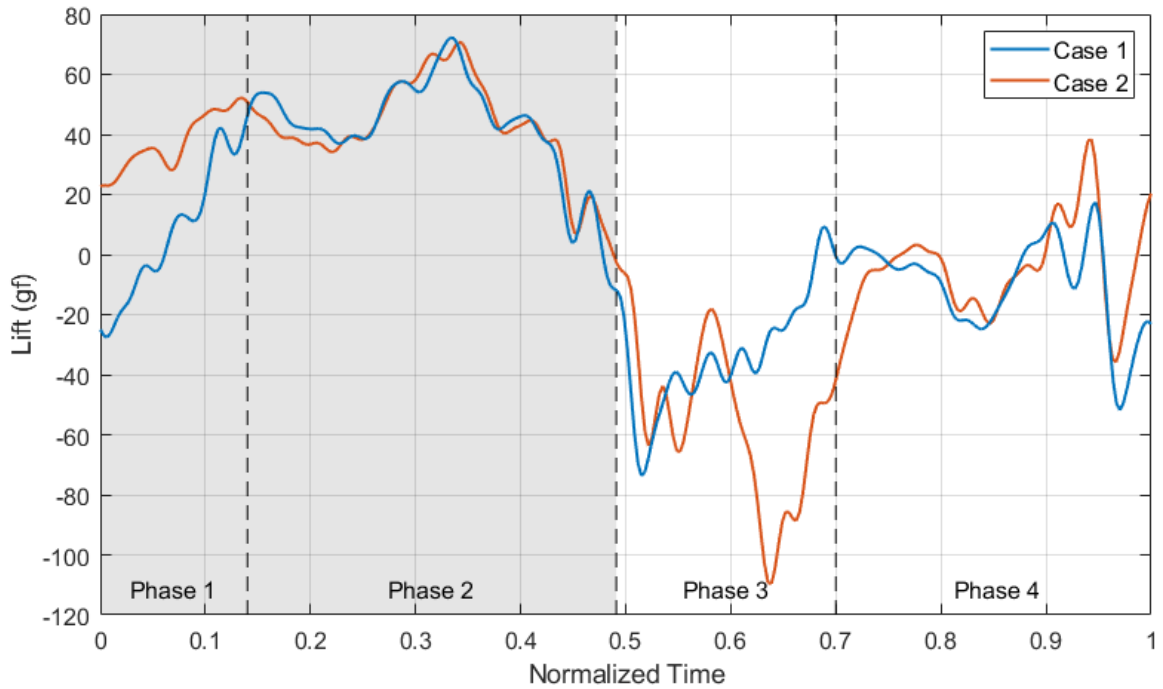


Figure 4-15 Lift production history comparison of both cases

By a side-by-side comparison, the time history can be divided into several phases according to their unique characteristics. Phase 1 starts from  $T = 0$  to  $T = 0.14$  where the lift generated by case 2 exceeds that by case 1. Phase 2 then goes from  $T = 0.14$  to  $T = 0.49$  where both cases generated comparable lift throughout the downstroke. Phase 3 is the folding phase ranging from  $T = 0.49$  to  $T = 0.7$  during the upstroke right after stroke reversal. Phase 4, which is characterized as the none-lifting portion of the upstroke, proceeds phase 3 to the end of the wingbeat cycle.

### **4.3.2 Phase 1 – Pre-downstroke**

The pre-downstroke phase is the initial section of the downstroke where the flow field could be highly unsteady due to mechanisms such as added mass or wing-wake interactions. According to Figure 4-15, during this phase, the lift generated by case 2 reached a stable value nearly instantly while the lift generated by case 1 started with a negative value and increased in a significantly slower rate. By observing the camera images in Figure 4-16, it

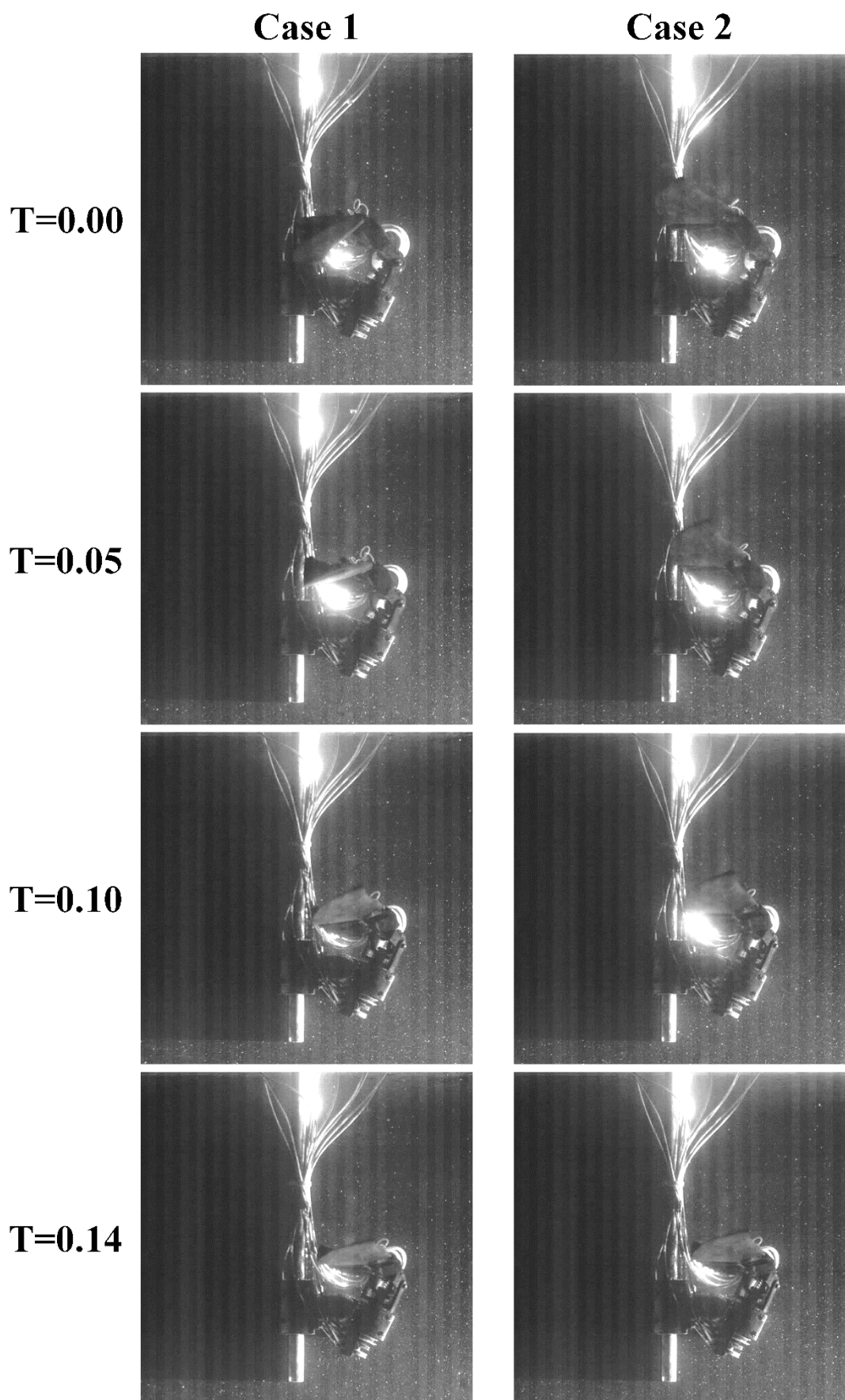


Figure 4-16 Kinematic comparison of Phase 1

was obvious that case 2 maintained the folding angle at an extended position throughout the pre-downstroke phase, mainly due to its less-folded upstroke, while case 1 initially struggled to extend its folded wing which means that there was less wing area to generate lift. However, to understand how case 2 was able to rapidly generate lift during initial downstroke and why case 1 generated negative lift initially, we have to take a look at the flow field.

Figure 4-17 and Figure 4-18 show the flow field comparisons around the arm section ( $y = 60$  mm) and the hand section ( $y = 150$  mm) of case 1 and 2 during the pre-downstroke phase. Both figure show that the wake and jet flow created by the previous upstroke were significantly greater in case 2. As the downstroke starts, both the upper wing and the lower wing flap through the rearward jet flow performing the so called ‘wake capture’ motion, which creates a high shear gradient at the leading edge of the wing that assists and accelerates the formation leading-edge vortices. This effect can be clearly seen in Figure 4-18 where the upper surface of the lower wing in case 2 already exists visible leading-edge vortex even at  $T = 0$ . Therefore, case 2 was able to rapidly generate lift at the beginning of each downstroke.

On the other hand, Figure 4-17 shows only minor wake in case 1, meaning that the upper wing will start generate lift slower than that of case 2. In addition, although there is some visible rearward jet flow in Figure 4-18 for case 1, the extending of folding angle caused the lower wing to move in the opposite direction of the downstroke. Instead of benefiting from the jet flow that generates positive lift, the ‘added mass’ effect in the opposite direction can be clearly seen at  $T = 0$  and  $T = 0.05$  where the fluid above the wing was pushed upwards as the wing extended, creating negative lift. Furthermore, a counterclockwise trailing-edge vortex also provide strong evidence that the hand section was producing negative lift in the initial downstroke. It was not until the unfolding motion slowed down that the wing started to generate positive lift. This can also be confirmed by the late-

forming leading-edge vortex and the breakdown of the original trailing-edge vortex at  $T = 0.14$ . The average lift produced in this phase for case 1 and 2 were 7.342 gf and 37.269 gf which had a huge difference.



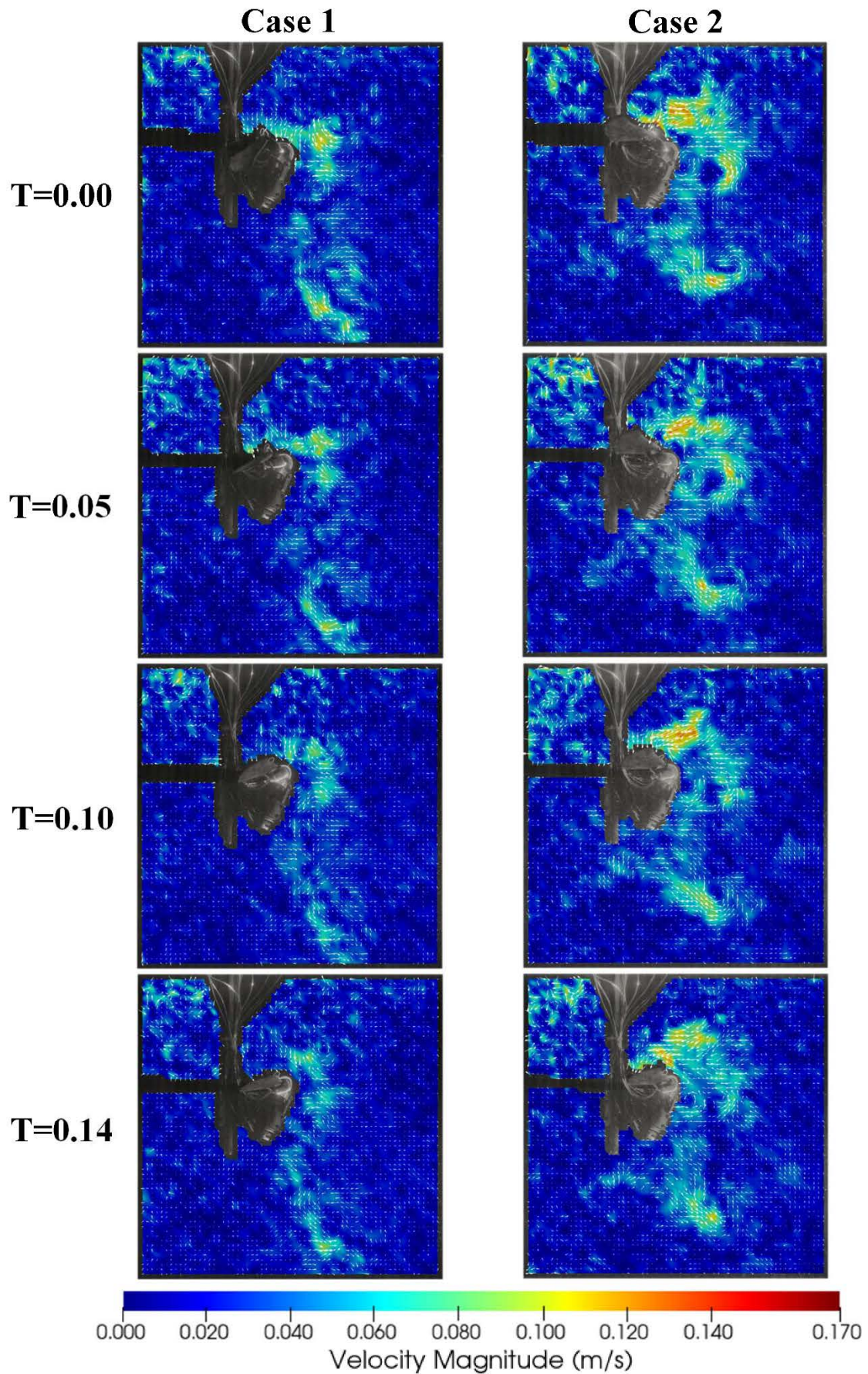


Figure 4-17 Velocity field comparison of phase 1 at  $y = 60$  mm

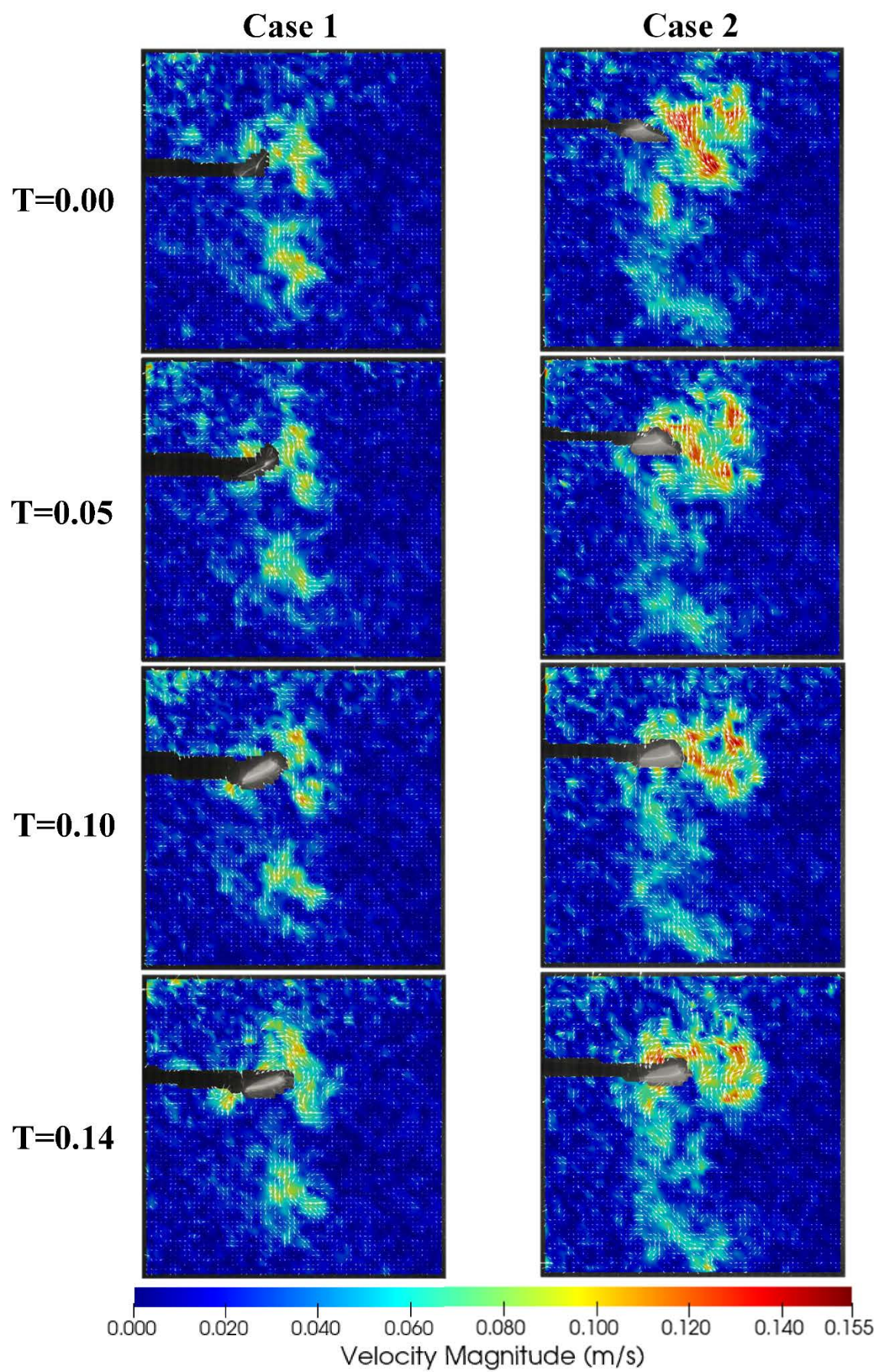


Figure 4-18 Velocity field comparison of phase 1 at  $y = 150$  mm

### **4.3.3 Phase 2 – Downstroke**

During the downstroke phase, two cases performed nearly identical wing kinematics which are compared in Figure 4-19, therefore, the lift production history was also highly similar. Most of the lift required for hovering flight was produced in this phase. The average lift produced in this phase for case 1 and 2 were 42.518 gf and 42.554 gf. In addition, maximum lift happened after mid-downstroke at  $T = 0.33$  where large amount of momentum was transferred into the fluid as shown in Figure 4-20.

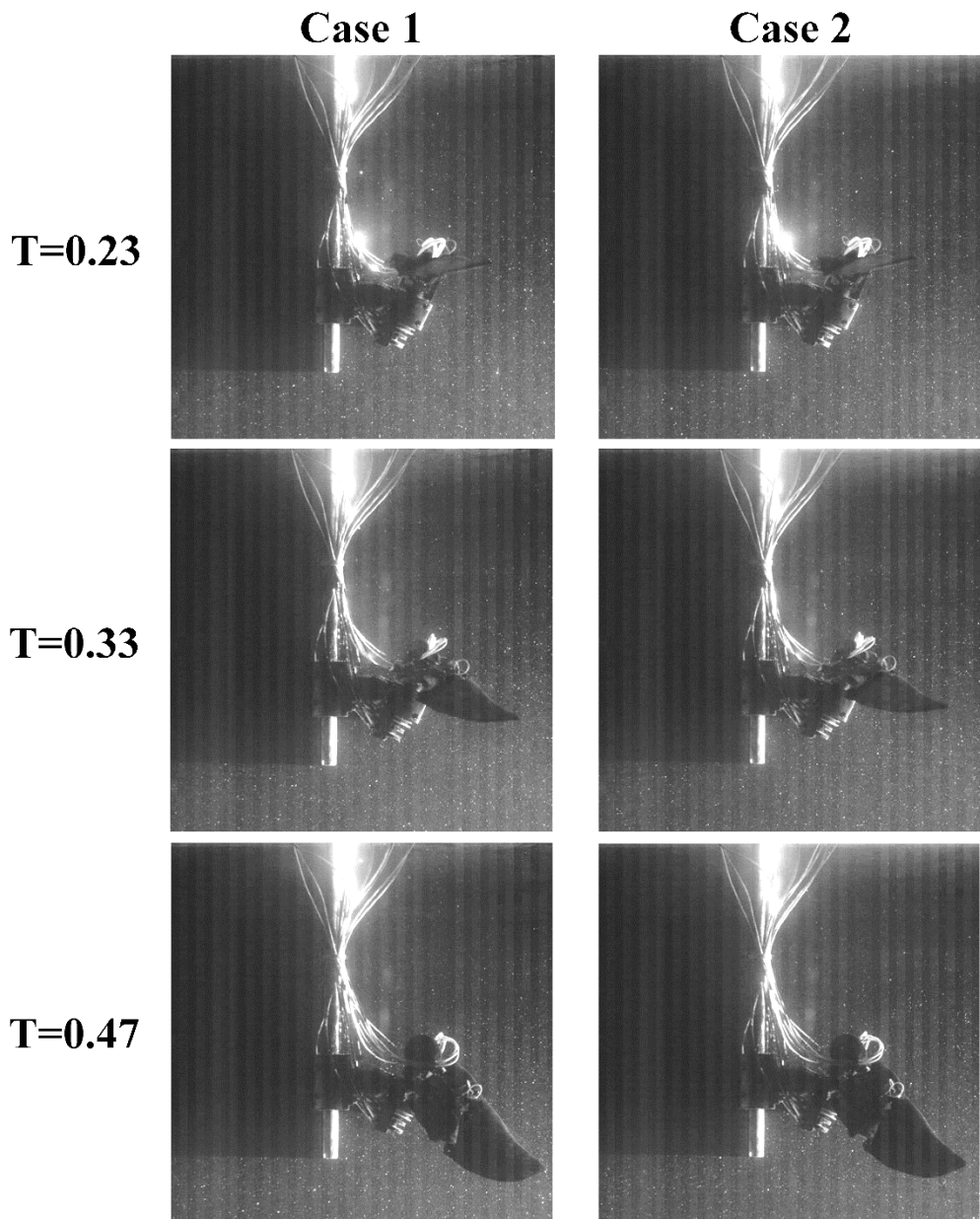


Figure 4-19 Kinematic comparison of phase 2

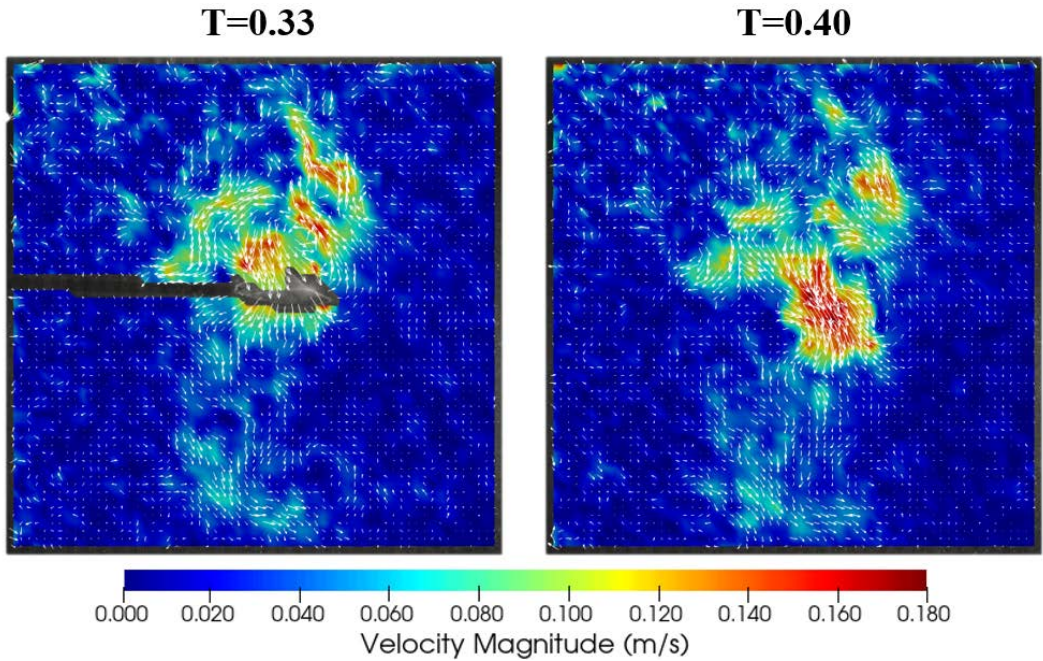


Figure 4-20 Velocity field during and after maximum lift at  $y = 150$  mm (case 2)

Interestingly, there appeared to be a small spike in lift production at  $T = 0.47$  right before stroke reversal in both cases which indicates a possible ‘clap’ effect between wings. By examining the velocity field at that moment, which is shown in Figure 4-21, we found that both cases exhibit a downward jet flow which confirms the hypothesis of a slight clap effect which enhanced lift just before stroke reversal.

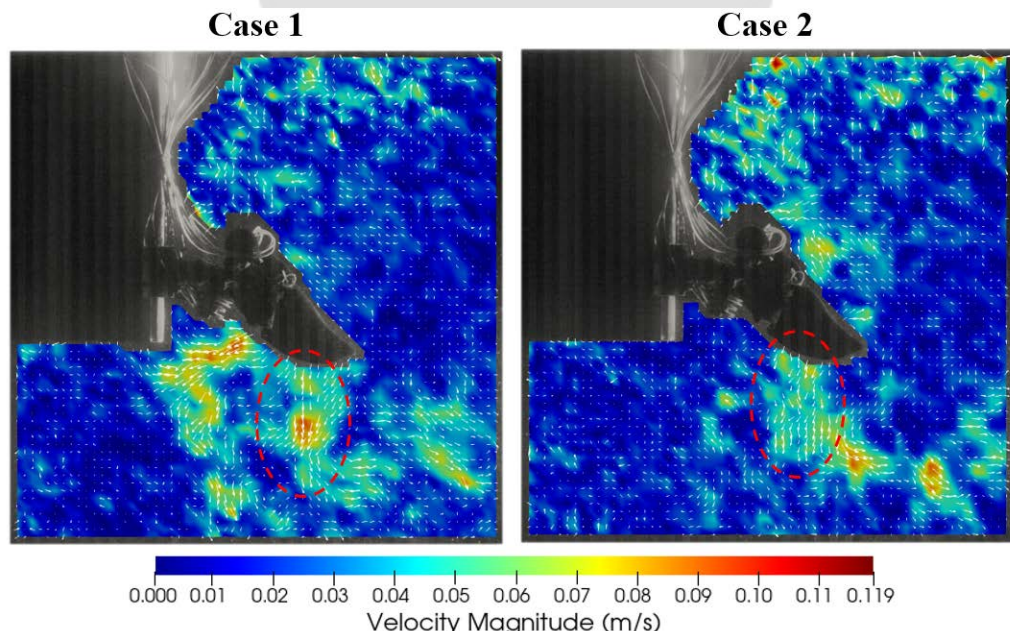


Figure 4-21 Velocity field of clap effect before stroke reversal ( $y = 0$  mm)

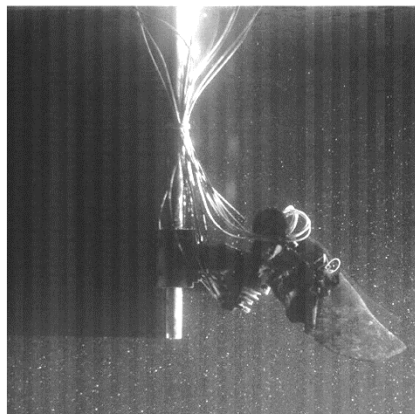
#### **4.3.4 Phase 3 – Folding Upstroke**

The main difference between the two cases comes in the folding upstroke phase where case 1 performed a more passerine-like folding motion and case 2 performed a version of reduced folding amplitude. As expected, the average lift produced in this phase for case 1 and 2 were  $-32.535 \text{ gf}$  and  $-54.260 \text{ gf}$  where a larger folding amplitude during upstroke resulted in less negative lift generated. To further investigate the relations between wing folding, flow condition and lift production, moments of the start of upstroke at  $T = 0.49$  initial negative peak in lift at  $T = 0.51$ , the minimum negative lift generated at  $T = 0.58$  and the largest negative peak  $T = 0.639$  in the lift production history of case 2 were examined.

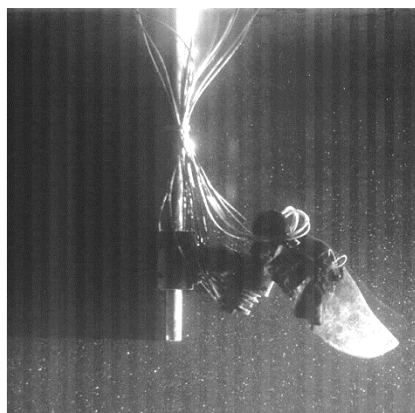
According to the camera images shown in Figure 4-22, two cases performed similar motion during the initial portion of the upstroke from  $T = 0.49$  to  $T = 0.51$  which can be confirmed by the lift production history. At  $T = 0.58$ , wing kinematics started to depart from each other where case 1 folded its outer wing inwards and case 2 maintained a more extended configuration. From Figure 4-23, we can see that the inward-folding of case 1 at this moment created a much higher velocity upward jet flow compared with that created by case 2, hence the greater negative lift produced by case 1. Following on is the most interesting part where case 2 produced significantly larger negative lift at  $T = 0.639$ . At this stage, the upper wing in both cases initiated a rapid sweep-back and pitch-down motion. However, case 1 had already completed the folding process meaning that it had significantly less effective wing area for force production. On the other hand, the extended wing of case 2 created a large low pressure region under the wings which sucked a great amount of fluid inwards and upwards as shown in Figure 4-23. This effect is similar to a ‘fling’, however, in the opposite direction where the trailing edge departs first creating negative lift.

**Case 1**

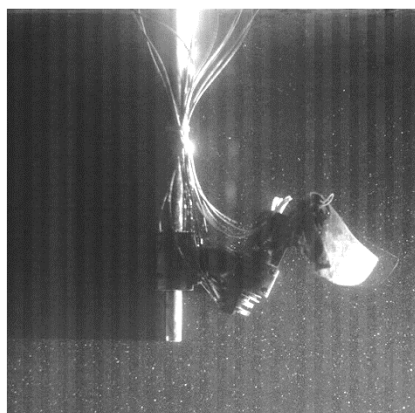
**T=0.49**



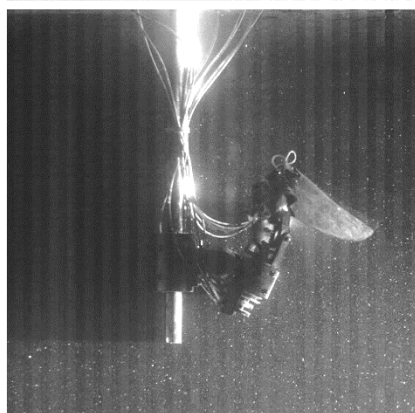
**T=0.51**



**T=0.58**



**T=0.639**



**Case 2**

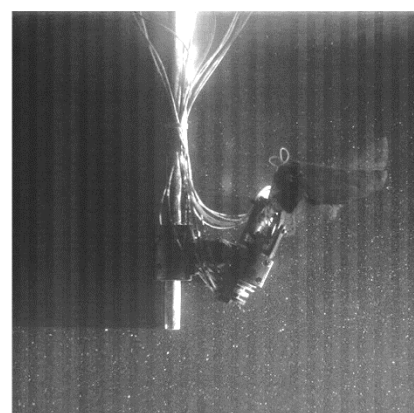
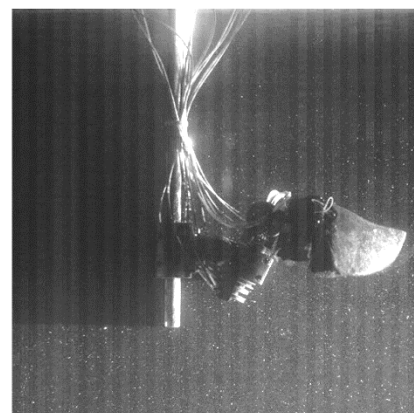
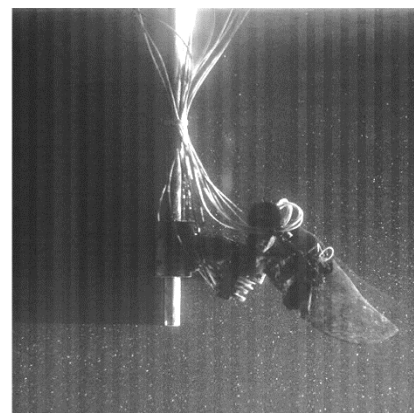
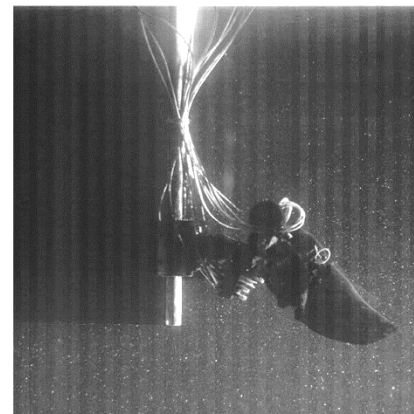


Figure 4-22 Kinematic comparison of phase 3

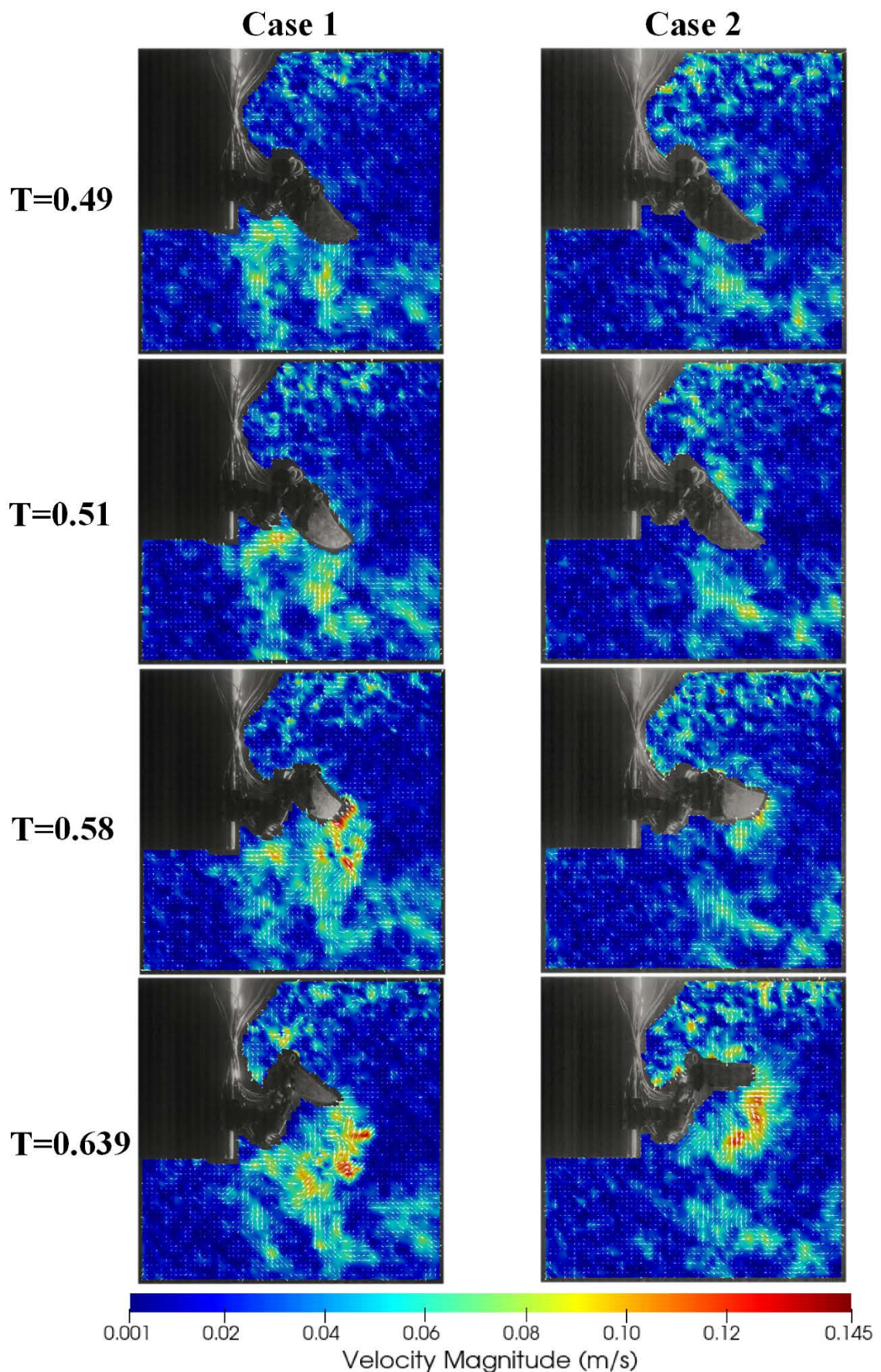
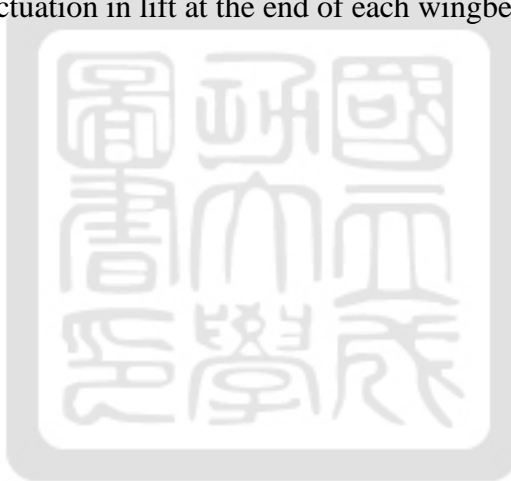


Figure 4-23 Velocity field comparison of phase 3 at  $y = 0$  mm

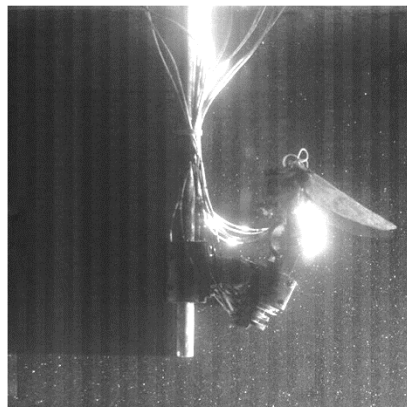
#### **4.3.5 Phase 4 – None-lifting Upstroke**

During this phase, the average lift production for case 1 and 2 were  $-9.609\text{ gf}$  and  $-4.560\text{ gf}$  which are both significantly lower than most other phases in terms of their amplitudes. Figure 4-24 shows the kinematic comparison of both cases within this phase. From  $T = 0.7$  to  $T = 0.8$ , case 2 started the unfolding process which produced some negative lift while other angles maintained nearly the same. Nearly no lift was generated by case 1 in this stage since it also remained quite stationary. As the time approaches the end of the wingbeat cycle, wings in both cases rapidly moved rearwards between  $T = 0.9$  and  $T = 1.0$  which placed the wing in a suitable position for the following downstroke. This also caused the larger fluctuation in lift at the end of each wingbeat cycle.

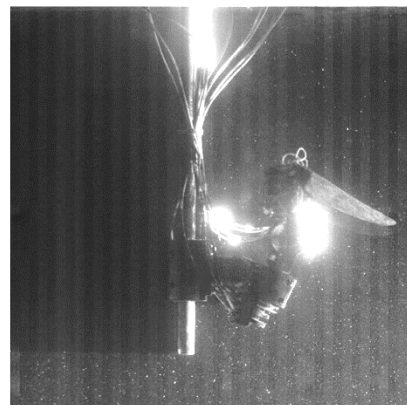


**Case 1**

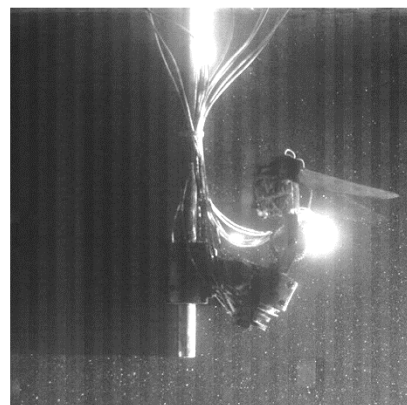
**T=0.70**



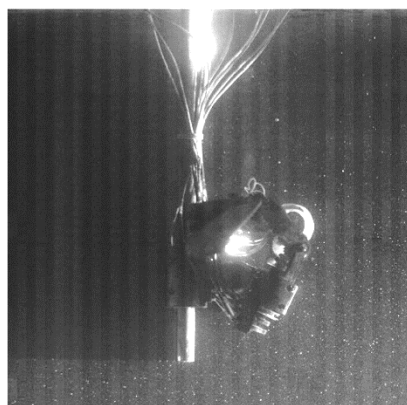
**T=0.80**



**T=0.90**



**T=1.0**



**Case 2**

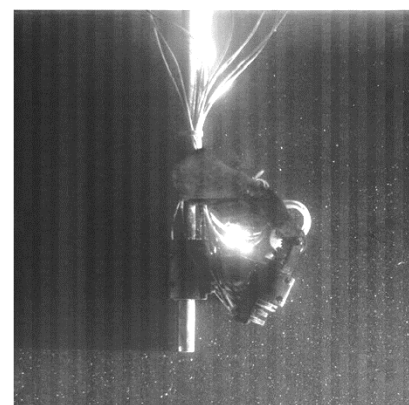
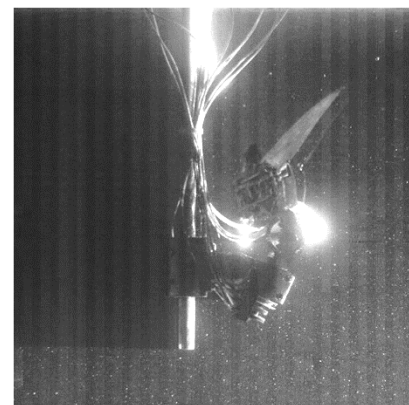
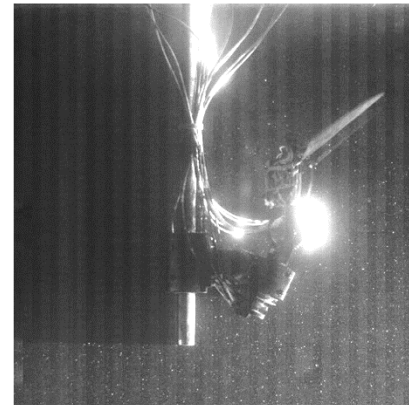
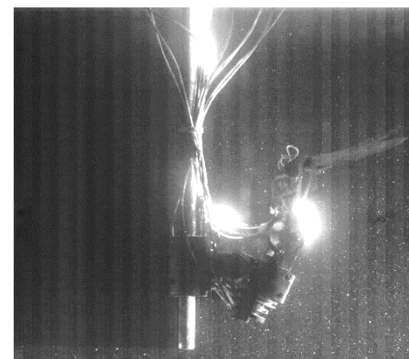


Figure 4-24 Kinematic comparison of phase 4

#### **4.3.6 Comparisons**

According to the dynamic scaling law, the equivalent averaged lift force during hovering flight in air can be calculated by

$$L_{avg,eq} = L_{avg,robot} \times \frac{\rho_{air} V_{w,bird}^2 S_{bird}}{\rho_{water} V_{w,robot}^2 S_{robot}} \quad (4-2)$$

From the data of kinematic analysis in chapter 3, the average wingtip velocity of case 1 and case 2 are 0.2537 m/s and 0.2675 m/s. The wing area of the robot is 96.19 cm<sup>2</sup>. According to Chang et al.[20], the wing area, average wingtip velocity and average body mass of Japanese white-eye (*Zosterops japonicus*) are 15.3 cm<sup>2</sup>, 9.4 m/s and 6.9 g, which gives

$$\begin{aligned} L_{avg,eq,case1} &= 1.643 \text{ gf (23.8\% body mass)} \\ L_{avg,eq,case2} &= 1.770 \text{ gf (25.7\% body mass)} \end{aligned} \quad (4-3)$$

The robot in the present research only produced a cycle-averaged lift of around one fourth the body mass of a passerine. This could result from the fact that instead of completely replicating the hovering motion of passersines, the robot was programed with a modified wing trajectory in this experiment due to its physical constraints. Despite the low cycle-averaged lift force, the lift-to-weight ratio history of case 1 showed some similar trends as that of real passersines which is shown in Figure 4-25. The more passerine-like case 1 kinematics exhibits similar value and timing of peak lift-to-weight ratio during downstroke. In addition, similar sudden peak in lift during the ‘clap’ event at stroke reversal was also replicated. However, during upstroke, data of real passersines seems to show a more positive trend compared with the negative-lifting upstroke of the robot. The validity of the highly scattered and positive-lifting data points during upstroke should also be questioned since a continuous near-zero or

negative lift production, similar to that measured in this research, is more reasonable in most hovering birds[43].

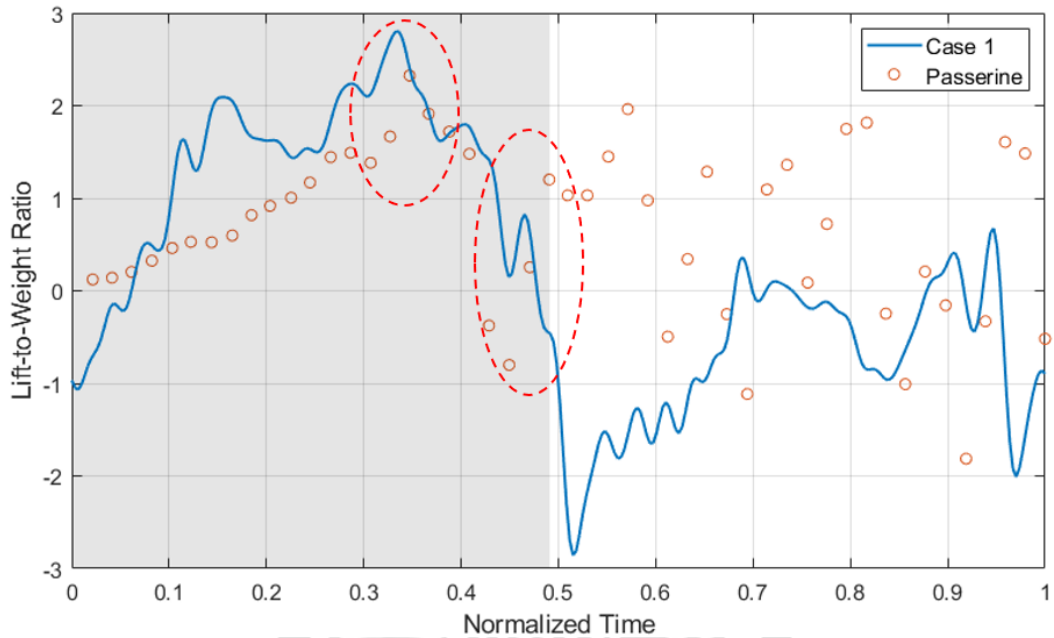


Figure 4-25 Lift-to-weight ratio comparison of case 1 and real passerines (data source:[38])

The lift-to-weight ratio of both cases are also compared in Figure 4-26 with the phase-averaged lift, stroke-averaged lift and the cycle-averaged lift listed in Table 4-1 and Table 4-2. The percentages in brackets represent the body weight ratio of each components.

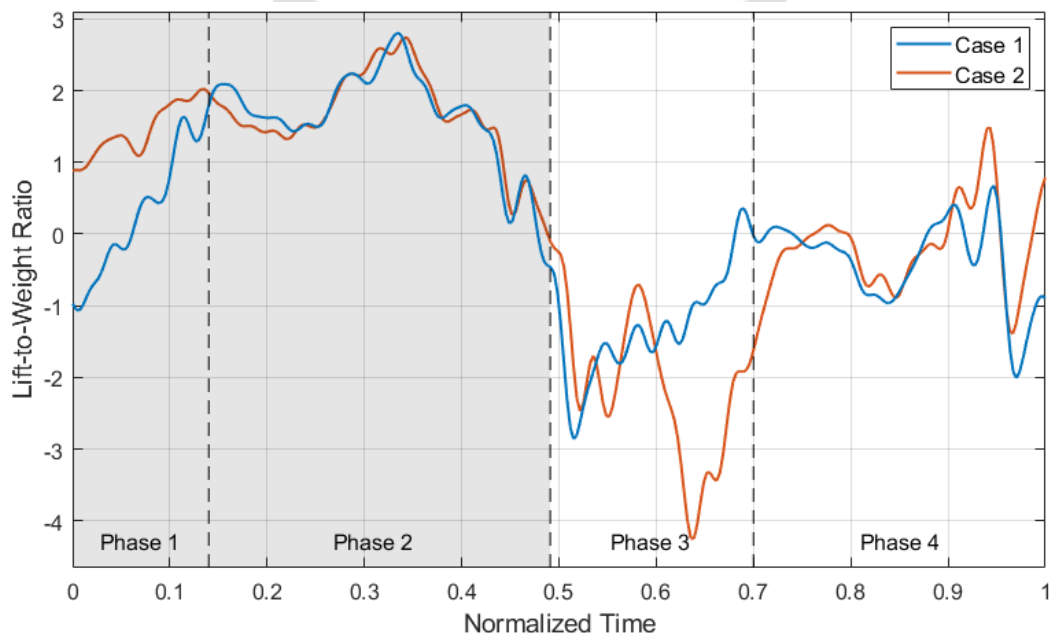


Figure 4-26 Lift-to-weight ratio comparison of both cases

Table 4-1 Equivalent averaged lift of case 1

	Downstroke		Upstroke	
	Phase 1	Phase 2	Phase 3	Phase 4
Phase-averaged Lift	1.966 gf (28.9%)	11.384 gf (165.0%)	-8.711 gf (-126.2%)	-2.573 gf (-37.3%)
Stroke-averaged Lift		8.666 gf (125.6%)		-5.108 gf (-74.0%)
Cycle-averaged Lift			1.643 gf (23.8%)	

Table 4-2 Equivalent averaged lift of case 2

	Downstroke		Upstroke	
	Phase 1	Phase 2	Phase 3	Phase 4
Phase-averaged Lift	9.979 gf (144.6%)	11.394 gf (165.1%)	-14.528 gf (-210.6%)	-1.221 gf (-17.7%)
Stroke-averaged Lift		10.990 gf (159.3%)		-6.657 gf (-96.5%)
Cycle-averaged Lift			1.770 gf (25.7%)	

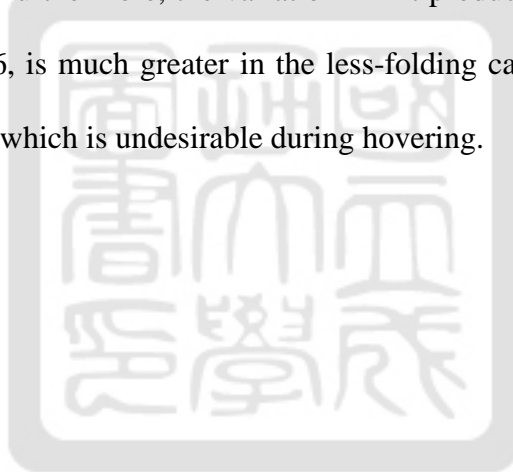
During downstroke, case 2 greatly benefited from the pre-extended wing and also the ‘wake capture’ effect resulting in nearly identical lift production in phase 1 and phase 2 while case 1 could not even support its own weight in phase 1. Through the reduced folding amplitude in case 2, negative lift was successfully increased as expected with a value over 2 times the body weight in phase 3. However, since the folding happened in a relatively short period of time, the negative effect on cycle-averaged lift was easily mitigated with the high lift in phase 1 resulting in an even higher cycle-averaged lift.

One more thing that should be noticed is that greater lift generated does not necessarily corresponds to better flight performance. Any lift-generating always comes with a cost, i.e.

drag, which dominates the power requirement with positive correlation during flight. Assuming that the wing efficiency of both cases are the same and neglecting the horizontal force components, we can roughly estimate and compare the power requirements with the average of the absolute value of lift force as

$$P_{\text{required}} \propto |L|_{\text{avg}} \quad (4-4)$$

which are 28.666 gf for case 1 and 35.374 gf for case 2. Therefore, we can roughly estimate that the power requirement for the greater-lifting case 2 could be over 23% higher than that of case 1 which compared with the 8% increase in lift is a great downside of the case 2 wing kinematics. Furthermore, the variation in lift production, i.e. the peak-to-peak difference in Figure 4-26, is much greater in the less-folding case 2, which could lead to larger vertical vibrations which is undesirable during hovering.



# **CHAPTER V**

## **Conclusion**

This chapter concludes the results from the kinematic analysis, force measurement and flow visualization experiment. Suggestions regarding further improvements on different aspects are also made for future studies.

### **5.1 Concluding Remarks**

This research focused on the construction, verification and experimenting of a novel multiple-DOF flapping-wing robot for submerged aerodynamic experiments on the impact of different folding angles. During preparation of the experiments, previously observed wing kinematics of passerines were transferred into controllable angles through mathematical representation of the robot kinematics and GA optimization.

According to results from the kinematic analysis, the robot was able to perform the proposed wing kinematics with correlation coefficients over 0.9 and less than 20% mean error for most kinematic angles. This implies that the mathematical representation and transformation derived during preparation were correct. Errors are mainly due to the imperfections and rigidities of the robot which allows each degree of freedom to passively rotate slightly under load. However, twisting angles of both cases exhibited low correlation coefficient and much higher percentage of errors due to the relatively unchanged angle.

By examining the lift production history of both cases, each cycle could be segmented into 4 phases with unique characteristics. Phase 1 is the pre-downstroke phase where case 1 initially unfolded its wing creating negative lift and case 2 rapidly started generating lift due

to the ‘wake capture’ effect. During this phase, case 2 generated 5-times more averaged lift than case 1.

Phase 2 is the downstroke phase where two cases performed nearly identical wing kinematics and generated comparable lift through the phase. Maximum lift was produced right after mid-downstroke in both cases and also highly correlates to the lift data of real passerines deduced in previous research. Furthermore, a slight ‘clap’ effect, which also exists in the data of real passerines, just before stroke reversal was observed in the lift production history for both cases and was also confirmed by the downward jet flow in the flow fields.

Phase 3 is the folding phase where case 2 produced negative averaged-lift greater than 2-times its body weight. The less-folded wing in case 2 created a large low-pressure bubble under the wings during a rapid sweep-back and pitch-up motion which caused the surrounding fluid to move inwards and upwards generating significant negative lift as expected. However, this negative effect on lift was mitigated by the high lift generated in phase 1 resulting in an unexpected higher overall lift compared with case 1.

Phase 4 is the non-lifting upstroke phase where both cases generated significantly less force compared with other phases. During this phase, case 2 started unfolding its wing much earlier than case 1 which is also favorable for the lift production in the following downstroke.

By looking at the complete wingbeat cycle, the average lift force generated by the robot was significantly lower than the body weight of a passerine which could result from the modification of wing kinematics due to robot constraints. Finally, although the initially-assumed unfavorable case 2 turned out to generate higher lift by 8%, the power consumption was estimated to be over 23% higher than case 1. Therefore, despite the slightly higher averaged lift, a less-folded upstroke during hovering flight might not be the right choice regarding flight performance and efficiency. Combined with the possible larger

vertical vibration, this could be the underlying reason why small birds such as passerines tends to maximize folding during hovering upstrokes.



## **5.2 Perspectives**

The flapping-wing robot constructed in this research provides a platform for further kinematic or aerodynamic experiments on flapping wings due to the high DOF and programmable wing trajectories. This research only experimented with the effect of different folding angles on lift force while other angles and possible perspectives such as horizontal forces and power requirements remained untested.

Furthermore, there are still several inherent flaws in the present design of the robot which can lead to inaccurate tracking of desired trajectories and possibly result in incorrect force readings and flow conditions. The most significant deficiency is the free play caused by the pulley system. The insufficient rigidity of the cable-shrouding Teflon tube and gaps between the cables and the inner wall of the tubes allows the robot to move under load. A Bowden drive system with higher rigidity or a waterproof direct drive system could be a more desirable design. Furthermore, direct angular feedback at each joint is recommended since it not only reduces the workload of kinematic verification, which is still time consuming even with the automated MATLAB program, but also act as a feedback signal for the control system, which could possibly improve tracking accuracy even under external loads.

## REFERENCES

- [1] D. A. Reay, *The History of Man-Powered Flight*. Elsevier Science, 2014.
- [2] T. A. Ward, C. J. Fearday, E. Salami, and N. Binti Soin, "A bibliometric review of progress in micro air vehicle research," *International Journal of Micro Air Vehicles*, vol. 9, no. 2, pp. 146-165, 2017.
- [3] R. J. Wood *et al.*, "An autonomous palm-sized gliding micro air vehicle," *IEEE Robotics & Automation Magazine*, vol. 14, no. 2, pp. 82-91, 2007.
- [4] F. Bohorquez, P. Samuel, J. Sirohi, D. Pines, L. Rudd, and R. Perel, "Design, analysis and hover performance of a rotary wing micro air vehicle," *Journal of the American Helicopter Society*, vol. 48, no. 2, pp. 80-90, 2003.
- [5] S. Deng, M. Percin, and B. van Oudheusden, "Experimental investigation of aerodynamics of flapping-wing micro-air-vehicle by force and flow-field measurements," *AIAA Journal*, vol. 54, no. 2, pp. 588-602, 2015.
- [6] T. N. Pornsin-Sirirak, Y.-C. Tai, C.-M. Ho, and M. Keennon, "Microbat: A palm-sized electrically powered ornithopter," in *Proceedings of NASA/JPL Workshop on Biomimetic Robotics*, 2001, pp. 14-17.
- [7] *MicroBat*. Available: <http://touch.caltech.edu/research/bat/bat.htm>
- [8] M. Keennon, K. Klingebiel, and H. Won, "Development of the nano hummingbird: A tailless flapping wing micro air vehicle," in *50th AIAA aerospace sciences meeting including the new horizons forum and aerospace exposition*, 2012, p. 588.
- [9] M. Percin, Y. Hu, B. Van Oudheusden, B. Remes, and F. Scarano, "Wing flexibility effects in clap-and-fling," *International Journal of Micro Air Vehicles*, vol. 3, no. 4, pp. 217-227, 2011.
- [10] M. P. G.C.H.E. de Croon, B.D.W. Remes, R. Ruijsink, Christophe De Wagter, *The DelFly - Design, Aerodynamics, and Artificial Intelligence of a Flapping Wing Robot*. Springer Netherlands, 2016.
- [11] D. D. Chin and D. Lentink, "Flapping wing aerodynamics: from insects to vertebrates," *Journal of Experimental Biology*, vol. 219, no. 7, pp. 920-932, 2016.
- [12] C. P. Ellington, C. Van Den Berg, A. P. Willmott, and A. L. Thomas, "Leading-edge vortices in insect flight," *Nature*, vol. 384, no. 6610, p. 626, 1996.
- [13] D. Lentink and M. H. Dickinson, "Rotational accelerations stabilize leading edge vortices on revolving fly wings," *Journal of Experimental Biology*, vol. 212, no. 16, pp. 2705-2719, 2009.
- [14] S. P. Sane, "The aerodynamics of insect flight," *Journal of Experimental Biology* vol. 206, no. 23, pp. 4191-4208, 2003.

- [15] S. P. Sane and M. H. Dickinson, "The control of flight force by a flapping wing: lift and drag production," *Journal of Experimental Biology*, vol. 204, no. 15, pp. 2607-2626, 2001.
- [16] V. M. Kramer, "Die zunahme des maximalauftriebes von tragflugeln bei plötzlicher anstellwinkelvergrosserung (boeneffekt)," *Z. Flugtech. Motorluftschiff*, vol. 23, pp. 185-189, 1932.
- [17] M. M. Munk, "Note on the air forces on a wing caused by pitching," *NACA Report*, 1925.
- [18] T. Theodorsen, "General theory of aerodynamic instability and the mechanism of flutter," *NACA Report*, 1949.
- [19] S. P. Sane and M. H. Dickinson, "The aerodynamic effects of wing rotation and a revised quasi-steady model of flapping flight," *Journal of Experimental Biology*, vol. 205, no. 8, pp. 1087-1096, 2002.
- [20] Y.-H. Chang, S.-C. Ting, J.-Y. Su, C.-Y. Soong, and J.-T. Yang, "Ventral-clap modes of hovering passerines," *Physical Review E*, vol. 87, no. 2, p. 022707, 2013.
- [21] R. Srygley and A. Thomas, "Unconventional lift-generating mechanisms in free-flying butterflies," *Nature*, vol. 420, no. 6916, p. 660, 2002.
- [22] B. K. van Oorschot, E. A. Mistick, and B. W. Tobalske, "Aerodynamic consequences of wing morphing during emulated take-off and gliding in birds," *Journal of Experimental Biology*, vol. 219, no. 19, pp. 3146-3154, 2016.
- [23] I. G. Ros, M. A. Badger, A. N. Pierson, L. C. Bassman, and A. A. Biewener, "Pigeons produce aerodynamic torques through changes in wing trajectory during low speed aerial turns," *The Journal of Experimental Biology*, vol. 218, no. 3, pp. 480-490, 2015.
- [24] B. F. Feshalami, M. Djavareshkian, M. Yousefi, A. Zaree, and A. Mehraban, "Experimental investigation of flapping mechanism of the black-headed gull in forward flight," *Proceedings of the Institution of Mechanical Engineers, Part G: Journal of Aerospace Engineering*, p. 0954410018819292, 2018.
- [25] Y.-H. Chang, S.-C. Ting, C.-C. Liu, J.-T. Yang, and C.-Y. J. E. i. F. Soong, "An unconventional mechanism of lift production during the downstroke in a hovering bird (*Zosterops japonicus*)," *Experiments in Fluids*, journal article vol. 51, no. 5, pp. 1231-1243, November 01 2011.
- [26] W. Shyy, Y. Lian, J. Tang, D. Viieru, and H. Liu, *Aerodynamics of low Reynolds number flyers*. Cambridge University Press, 2007.
- [27] J. G. Leishman, *Principles of Helicopter Aerodynamics*. Cambridge University Press, 2002.
- [28] W. Shyy, H. Aono, C.-k. Kang, and H. Liu, *An introduction to flapping wing aerodynamics*. Cambridge University Press, 2013.
- [29] T. Van Truong, D. Byun, M. J. Kim, K. J. Yoon, and H. C. Park, "Aerodynamic forces

- and flow structures of the leading edge vortex on a flapping wing considering ground effect," *Bioinspiration & biomimetics*, vol. 8, no. 3, p. 036007, 2013.
- [30] L. Y. Jen, "Aerodynamics of Three-Dimensional Flapping Wing," Doctor of Philosophy, National University of Singapore, 2017.
- [31] Y. Lu and G. X. Shen, "Three-dimensional flow structures and evolution of the leading-edge vortices on a flapping wing," *Journal of Experimental Biology*, vol. 211, no. 8, pp. 1221-1230, 2008.
- [32] J.-s. Han, J. W. Chang, J.-k. Kim, and J.-h. Han, "Role of trailing-edge vortices on the hawkmothlike flapping wing," *Journal of Aircraft*, vol. 52, no. 4, pp. 1256-1266, 2015.
- [33] S. Dhawan, "Bird flight, Sadhara," in *Academy Proceedings in Engineering Sciences*, 1991, vol. 16, pp. 275-352.
- [34] T. MUTLU, "Development and Testing of a 3 DOF Tandem Flapping wing Mechanism," The Graduate School of Natural and Applied Sciences, MIDDLE EAST TECHNICAL UNIVERSITY, 2014.
- [35] J. W. Bahlman, S. M. Swartz, and K. S. Breuer, "Design and characterization of a multi-articulated robotic bat wing," *Bioinspiration & Biomimetics*, vol. 8, no. 1, p. 016009, 2013.
- [36] R. S. Hartenberg and J. Denavit, "A kinematic notation for lower pair mechanisms based on matrices," *Journal of Applied Mechanics*, vol. 77, no. 2, pp. 215-221, 1955.
- [37] M. Uyguroğlu and H. Demirel, "Kinematic analysis of bevel-gear trains using graphs," *Acta Mechanica*, vol. 177, no. 1-4, pp. 19-27, 2005.
- [38] 章聿珩, "運動學參數對鳥類拍撲翼之升力影響," 機械工程學研究所, 臺灣大學, 2010 年, 2010.
- [39] Y. Abdel-Aziz, H. Karara, and M. Hauck, "Direct linear transformation from comparator coordinates into object space coordinates in close-range photogrammetry," *Photogrammetric Engineering & Remote Sensing*, vol. 81, no. 2, pp. 103-107, 2015.
- [40] N. M. Alem, J. W. Melvin, and G. L. Holstein, "Biomechanics applications of direct linear transformation in close-range photogrammetry," in *Proceedings of the Sixth New England Bioengineering Conference*, 1978, pp. 202-206: Elsevier.
- [41] R. B. George, "Design and Analysis of a Flapping Wing mechanism for Optimization," Department of Mechanical Engineering, Brigham Young University, 2011.
- [42] W. Thielicke and E. Stadhuis, "PIVlab—towards user-friendly, affordable and accurate digital particle image velocimetry in MATLAB," *Journal of Open Research Software*, vol. 2, no. 1, 2014.
- [43] U. M. Norberg, *Vertebrate flight: mechanics, physiology, morphology, ecology and evolution*

*evolution*. Springer Science & Business Media, 2012.

